BRNO UNIVERSITY OF TECHNOLOGY

VYSOKÉ UČENÍ TECHNICKÉ V BRNĚ

FACULTY OF MECHANICAL ENGINEERING

FAKULTA STROJNÍHO INŽENÝRSTVÍ

ENERGY INSTITUTE

ENERGETICKÝ ÚSTAV

DESIGN OF VERY LOW SPECIFIC SPEED PUMP

NÁVRH ČERPADLA S VELMI NÍZKÝMI SPECIDICKÝMI OTÁČKAMI

DOCTORAL THESIS

DIZERTAČNÍ PRÁCE

AUTHOR — Ing. LILIAN CHABANNES

AUTOR PRÁCE

SUPERVISOR — doc. Ing. PAVEL RUDOLF, Ph.D.

VEDOUCÍ PRÁCE

BRNO 2021

Abstrakt
Čerpadla s nízkými specifickými otáčkami nacházejí uplatnění v široké škále aplikací, ale trpí nízkou účinností a rizikem nestability křivky dopravní výšky. Tato disertační práce pojednává o vylepšení hydraulických parametrů čerpadla se specifickými otáčkami $n_s = 32$. Práce se zaměřuje na průtok v oběžném kole a ve spirále, které jsou řešeny pomocí CFD.

Průzkum literatury ukázal, že přidání mezilopatek do průtokového kanálu je účinný způsob, jak zlepšit neuspokojivé proudění obecně přítomné v oběžných kolech s nízkými specifickými otáčkami. Byla zkoumána poloha mezilopatky v kanálu a vliv počtu přítomných mezilopatek. Část výsledků je ověřena experimentálně v laboratoři fakulty.

Rovněž je zkoumán tvar spirály a pozornost je věnována numerickému řešení proudění u stěn a jeho vlivu na simulaci. Po numerických výpočtech na třech různých spirálách je navržen nový tvar, který zlepšuje vypočtové parametry čerpadla při nízkém i vysokém průtoku.

Summary
Low specific speed pumps find applications in a broad range of domains, but suffer from a low efficiency and a risk of head instability close to shut-off. This dissertation discusses hydraulic performance improvement of a pump with a specific speed $n_s = 32$. The work focuses on the flow in the impeller passage and the volute and is analyzed by means of CFD and experiments.

A literature survey showed that the addition of splitter blades in the flow passage is an efficient way to improve the unsatisfactory flow generally present in low specific speed impellers. Investigations have been made on the position of a splitter blade in the flow passage and on the influence of the number of present splitters. Part of the results are verified experimentally in the laboratory of the faculty.

The design of the volute is also investigated, and attention is paid to the numerical wall-treatment and its impact on the simulation. After numerical computations on three different volutes, a new volute design is proposed to improve the performance of the pump at both low and high flow rates.

Klíčová slova
Nízká měrná rychlost, Oběžné kolo, Volute, CFD, Stěnové funkce, mezilopatka.

Keywords
Low specific speed, Impeller, Volute, CFD, Wall-function, Splitter blade.

CHABANNES, LILIAN.*DESIGN OF VERY LOW SPECIFIC SPEED PUMP*. Brno: Vysoké učení technické v Brně, Faculty of Mechanical Engineering, 2021. 110 s. Vedoucí diplomové práce doc. Ing. Pavel Rudolf, Ph.D.

I declare that I have prepared my dissertation on the topic "Design of very low specific speed pump" independently under the guidance of the supervisor of the dissertation and using professional literature and other information sources, all cited in the work and listed in the literature at the end of the work.

Ing. Lilian Chabannes

I would like to thank the people that supported and helped me during my time in Czech Republic, while this thesis was in preparation and led to this final result. The past four years in Brno were a real adventure: new country, language, people and field of study.

Firstly, I want to thank my parents, Sylvie and Bernard, that supported me and never once doubted me, despite being 1500 km from them in the south of France. The same thing can be said about my brothers, Loïc and Lionel. Of course, a big thanks to Veronika, my girlfriend for her unwavering trust in my ability and her support to complete this work, which kept me motivated.

I would like to thank my supervisor, doc. Ing. Pavel Rudolf, Ph.D., for his guidance, accurate and thoughtful criticism of the work during the thesis and the final review of this thesis.

When I arrived in Brno, both CFD and turbomachinery were new worlds for me. For that reason, I would like to especially thank my former office colleagues, Pavel, Jakub and Prokop to whom I asked daily questions during my first months in the faculty and saved me from considerable struggle.

I am very grateful to David Štefan and Jiří Kozák. David for the constant help during the whole four years, whether it is in pump design, CFD, reviews of texts and articles, coffee pauses, etc... And Jiří for his very welcoming behaviour when I arrived in Czech Republic, two job opportunities that I gladly took, videos games and beers.

The most stressful part of the thesis was unquestionably the experimental part. It is also the part where I received the most help. An enormous thanks to Jiří Tůma for the countless hours spent manufacturing the pump components, always with a good mood. An enormous thanks to Martin, Bronislav and Karel from the laboratory who were always helping and joyful despite the constant working load in the laboratory and the language barrier.

Finally, I thank everyone part of the Viktor Kaplan department of fluid engineering, for the nice and kind atmostphere.

Ing. Lilian Chabannes

Contents

1. Introduction

1.1. Problem statement

1.1.1. Typical problems at low specific speed

Pumps are used in a wide range of applications. Cooling water pump, boiler feed pumps, rocket pumps or medical pumps cover a large area of applications, with power from a few watts to several megawatts. The centrifugal pump is the most widely used process pump and accounts for over 95% of all installations on ground and close to 75% of all developed pumped system for space applications. Centrifugal pumps are universally used because they are low cost and require low maintenance, they are simple to operate, provide a wide range of easily controlled, non-pulsating flow, and are suitable for clean, abrasive, corrosive or non-lubricating fluids. In addition, they are quiet, adaptable to motor, turbine or engine drive, can be obtained in a wide capacity-head range to handle fluids varying in temperature and have low space requirements. Designers and researchers are constantly challenged with specific needs, whether it is a high efficiency, broad operating range, challenging pressure requirements, need for decades of operations without maintenance for space applications and more. The design of low specific speed pumps is one of them.

Any pump application is characterized by the flow rate, the head and the rotor speed. To a large extent these parameters determine which impeller type and pump design to choose. These three performance parameters are interrelated by the specific speed n_s, which is of great importance for the selection and design of a pump.

$$n_s = 3.65\, N \frac{Q^{0.5}}{H^{0.75}} \tag{1.1}$$

With N $[RPM]$ the rotor speed, Q $[m^3.s^{-1}]$ the pump flow rate and H $[m]$ the pump head. Several definitions and notations are used for the specific speed. In Europe, and for pumps, n_q is the most popular. It is related to n_s by the relation $n_s = 3.65\, n_q$. In Czech Republic, the notation n_s is used for both pumps and turbines, and is adopted in this dissertation.

At high specific speed, i.e. $n_s = 600$ to $n_s = 1000$, axial pumps are the most common type of pumps. Their application often consists of displacing large volume of fluid at low pressure difference. Between $n_s = 250$ and $n_s = 600$, mixed flow pumps are used, where the outflow of the impeller is nor axial nor radial but inclined. Finally, between $n_s = 35$ and $n_s = 250$, radial pumps are the most common. As the specific speed decreases, a pump needs to provide a high pressure at a low flow rate. A pump with a specific speed below 75 is considered a low specific speed pump. Below $n_s = 35$, the pump is considered a very low specific speed pump. For convenience, all pumps with a specific speed below 75 will be called low specific speed pumps.

Below $n_s = 35$, the needs are extreme for centrifugal pumps, and a different type of technology can be used, the positive displacement pumps. A positive displacement pump makes a fluid move by trapping a fixed amount, i.e. geometric volume, and forcing (displacing) that trapped volume into the discharge pipe. In these pumps, energy is

periodically added by application of force to one or more movable boundaries of any desired number of enclosed, fluid-containing volumes, resulting in a direct increase in pressure up to the value required, moving the fluid through valves or ports into the discharge line. A large number of positive displacement pump exists. Some examples are cited below [1]:

- $n_s < 2$: Piston pumps
- $n_s < 7$: Gear pumps
- $n_s \in (7 - 36)$: Screw pumps

These pumps usually present a high efficiency ranging between 65 and 95%, and the attainable head is restricted by mechanical constraints or seal leakages. Other special types of pumps, with efficiencies usually in the range of 25 to 50% are also present, such as:

- $n_s \in (2 - 15)$: Peripheral pumps
- $n_s \in (3 - 36)$: Friction pumps
- $n_s \in (7 - 40)$: Side channel pumps

1.1.2. Need for low specific speed centrifugal pumps

Centrifugal pumps are of rare use at low specific speed, especially below $n_s = 35$. The primary reason is their low efficiency. Figure 1.1 presents the optimal efficiency that can be expected for a pump of a given specific speed at a given flow rate, based on statistical data of existing pumps. As the specific speed lowers, the efficiency drops sharply.

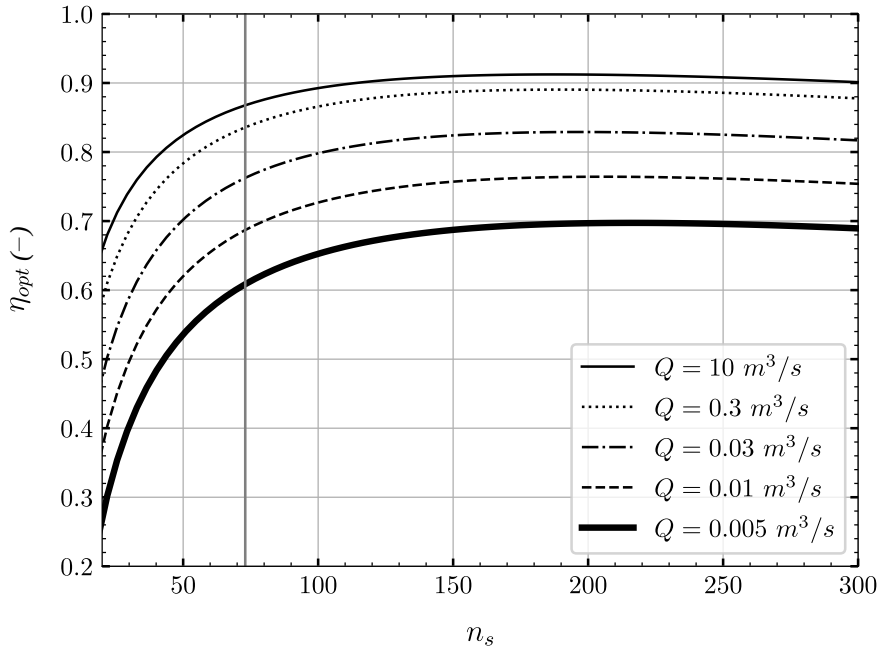

Figure 1.1: Optimal centrifugal pump efficiency as a function of specific speed. Adapted from [1].

In fact, multistage centrifugal pumps are used for services requiring heads higher than can be generated by a single impeller. All impellers are in series, the liquid passing from

one impeller to the next and finally to the pump discharge. The total head then is the summation of the heads of the individual impellers. This technology may be advantageous, as according to figure 1.1, several high efficient impellers in series may lead to a better total efficiency than a single low specific speed pumps.

When the use of multistage pumps is not possible, a low specific speed centrifugal pump needs to be considered. Indeed, the centrifugal pump design technology has crucial advantages in operation compared to positive displacement pumps. They can be operated at higher speed compared to positive displacement pumps, the pump design and the components are less complex, hence a lower failure probability and a lower number of wearing parts. Centrifugal pumps do not require pressure safety relief valves which are indispensable for the operation of positive displacement pumps. Last but not least, centrifugal pumps still have a consequent price advantage compared to positive displacement pumps and a simple sealing concept. Accordingly, research is interested in enhancing low specific speed centrifugal pumps performances.

Centrifugal radial pump design for specific speed between 80 and 350 is well documented and available for years, from Gülich [1] to Stepanoff [2], Japikse [3], or Karassik [4]. A complete design procedure based on theoretical and empirical formulas has been developed over the years in order to design single stage centrifugal pumps attaining high efficiency but it shows its limits at low specific speed.

1.2. Objectives

1.2.1. Improvement of hydraulic performances

The dissertation is focused on the hydraulic performance improvement of a low-specific speed pump of $n_s = 32$. The pump is a single-stage volute pump. Historically, the pump is part of the Viktor Kaplan department of fluid engineering for decades, and a great number of designs have been tested, see Klas [5, 6, 7]. Although the original pump design point and reference speed are used in the thesis, new impellers and volute casings have been tested both numerically and experimentally. It is believed that the results obtained are applicable for pump with specific speeds $n_s < 75$.

The work focuses on the flow in the impeller passage and the volute. The sidewall gaps are considered in calculations, but no special attention is given to their design, i.e. classic recommendations are used for their design.

The results of the thesis are presented into three separates studies.

- The first study, see section Study 1: Effect of a single splitter variation, deals with the influence of splitter blades on the performance of the pump. The impeller has 4 main blades and 4 splitter blades. Eight variations of splitter blades are tested numerically, three parameters control the position of the splitters. A design of experiment gives more hindsight about the influence of each parameter. Both steady and transient simulations are performed. The outcome of this first study is the suggestion of parameters for the placement of splitter blades into the impeller channel to aim for a specific goal, whether it favours pressure delivery or head stability.

- The second study, Study 2: Effect of the addition of 1 and 2 splitters per impeller passage, also deals with the influence of splitter blades on the performance. Firstly,

the volute has been redesigned compared to Study 1. Secondly, three impellers are tested. An impeller with 4 blades, a second with 8 blades (4 main blades and 4 long splitters) and a third impeller with 12 blades (4 main blades, 4 long splitters and 4 short splitters). The principal motivation for this study is to explore the influence of more splitters because of the lack of impellers with two splitter blades per impeller passage in the literature. For this reason, the study does not focus on an optimal placement of splitter blades, but rather aims to discuss the influence of the addition of splitters on the flow. The main performance curves (head, efficiency and torque) are validated experimentally for the three tested impellers. Then, a detailed flow analysis is performed based on the validated numerical results. The hydraulic power loss per domain is computed for each case to reveal in which regions of the pump the addition of splitters has a positive or negative impact. The flow at the outlet of the impeller allows to extract velocity components and evaluate the flow entering the volute. The development of the local eddy on the pressure side of the impeller is investigated as a function of the flow rate, and the role of splitters in its suppression is highlited. Finally, transient effects of splitters (pressure pulsations, hydraulic forces excitation...) on the pump are discussed. The outcome of this second study is a deeper understanding of the influence of splitters on the flow of low specific speed pumps.

- The third study, Volute throat area study has two different objectives. The first part is focused on CFD and more specifically on the influence of the wall-treatment on the prediction of the main pump characteristics. Recent studies based on the work of Juckelandt [8] exposed discrepancies between numerical and experimental results at low specific speed pumps. The conclusions of the author to properly capture the flow of low specific speed pumps are tested and validated in the first part. The second part evaluates the influence of the volute throat area on the pump characteristics. The performance of three volute designs with increasing volute throat area is computed numerically. After finding benefits from smaller and larger volute on the flow, a different volute design is proposed. The design is unconventional as it does not respect the rule of conservation of angular momentum for the spiral design of the casing, and improves the performance of the pumps at low and high flow. Based on these results, a new, unconventional volute design is proposed.

Only the results of the second study are validated experimentally. However, because the pump design of each study is very similar and the numerical methods used are identical, the results obtained in the first and third study are presented with confidence.

1.2.2. Tools used

Numerical simulations, or rather Computational Fluid Dynamics (CFD) is the main tool used in this thesis. The availability of computing power and software which are provided to the academics and the industry helps to analyze, predict and improve the flow behavior. Comparing to the experiments, CFD approach is usually cheaper and can provide more detailed information about the phenomena that scientists and engineers are interested in. However a great care has to be given to each computation to avoid inaccuracies and wrong conclusions. Coupled with experiments, a cost-efficient analysis can be performed on a given problem and this is the objective of this thesis. Computations are performed with

the commercial software `ANSYS-CFX 19.1` on the cluster `thor`, property of the faculty. The computations are used to assess the performance of the pumps and the flow physics. To validate the calculations, several experiments are performed in the hydraulic laboratory of the Viktor Kaplan department of fluid engineering.

2. State Of Art

This chapter is divided into two sections. In the first part, the flow mechanics of low specific speed pumps are presented. Indeed, due to the unique design of this type of pump, each fluid domain presents uncommon physics compared to classic centrifugal radial pumps. In the second part, the solutions that were found to tackle these problems are presented in a literature review.

2.1. Loss mechanisms and physical limitations

The inherent design of low specific speed pump is responsible for the low efficiency observed in figure 1.1. Pump impellers have a large diameter and a narrow meridional section and volutes have a small cross-sectional area relatively to their length.

As the specific speed decreases, the pump is required to provide a high pressure (or head) for a low flow rate. To achieve a high head, a large impeller diameter is necessary. More specifically, the ratio d_1/d_2 decreases with the specific speed, where d_1 is the impeller inlet diameter and d_2 the impeller outer diameter. The flow benefits from the effect of centrifugal forces providing a head rise. Additionally, the meridional section must be narrow to adapt to the low volume flow rate passing through the impeller. As a result, long and narrow bladed impellers are always found at low specific speed. Figure 2.1 illustrates this phenonemon as meridional sections of radial impeller get wider and thinner with n_s dropping. Typically, figure 2.2 presents the meridional section of fluid domains of a pump with a specific speed $n_s = 32$ that is used in this thesis.

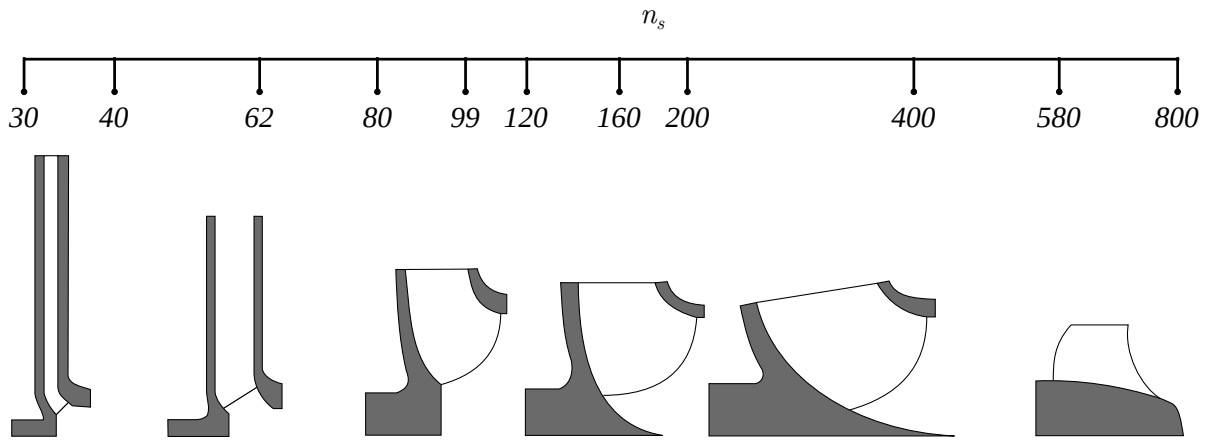

Figure 2.1: Schematic meridional section of impellers as a function of the specific speed. Adapted from [3].

The impeller is the core component of a centrifugal pump and the first designed element. The long and narrow shape of the impeller blades implies friction losses within the impeller. However, the impeller itself is a relatively efficient component in a low specific speed pump. Indeed, the work transfer in radial impellers of low specific speed is largely accomplished by centrifugal forces, as mentioned previously. This method of energy transfer implies very low losses in the impeller.

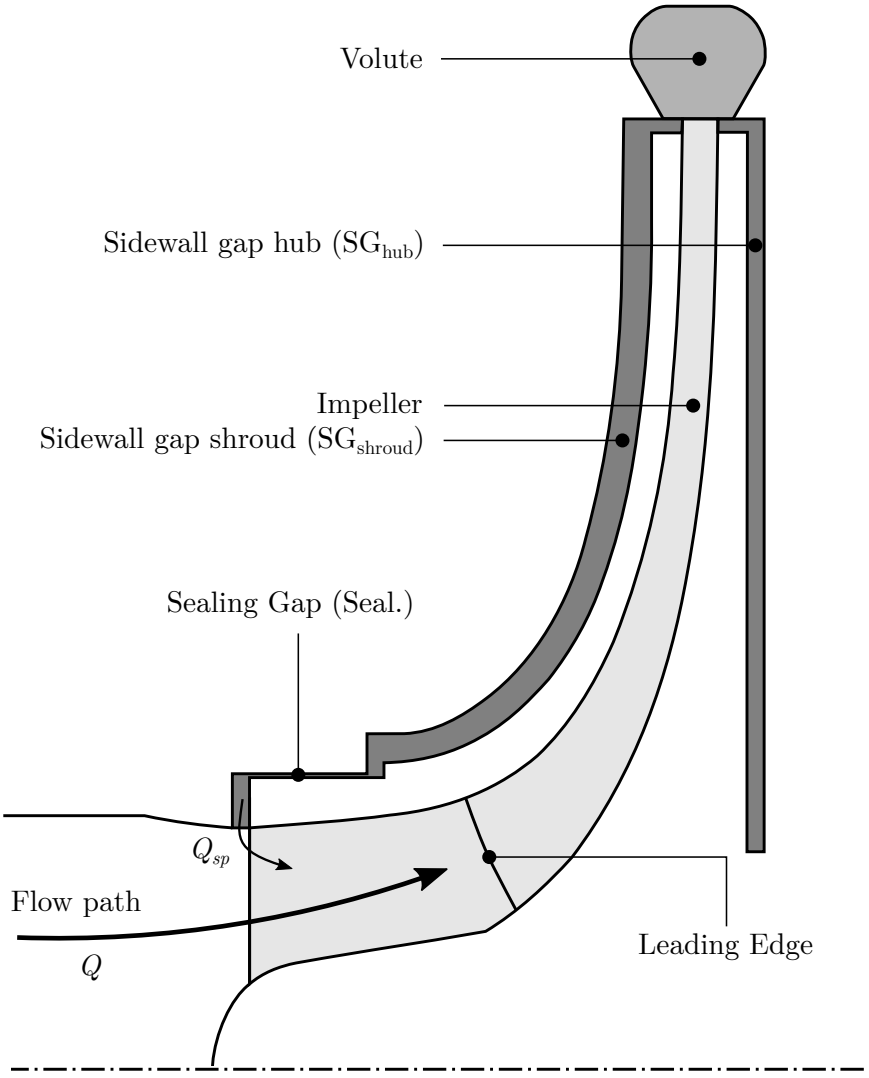

Figure 2.2: Schematic meridional section and main dimensions of a pump with a specific speed $n_s = 32$.

Figure 2.3, represents the head loss relative to the pump head due to the volute (black lines) and the impeller (blue lines) as a function of the specific speed. At low specific speed, the volute losses are higher and they diminish at higher specific speed. The opposite is observed for the impeller. At $n_s = 65$, the volute losses are, on average, 4 times higher than the impeller losses. At $n_s = 170$, the losses in the two components are similar, and the trend is reversed at higher specific speed, where the impeller contributes to most of the losses. The influence of the roughness on the losses is also represented, where ϵ (μm) represents the equivalent sand roughness as presented in [1]. An increase in roughness in each of the components naturally increases the losses. However the effect is different for both components. Rough walls in the volute have more impact than in the impeller at low specific speed, where the impact on the losses is moderately low.

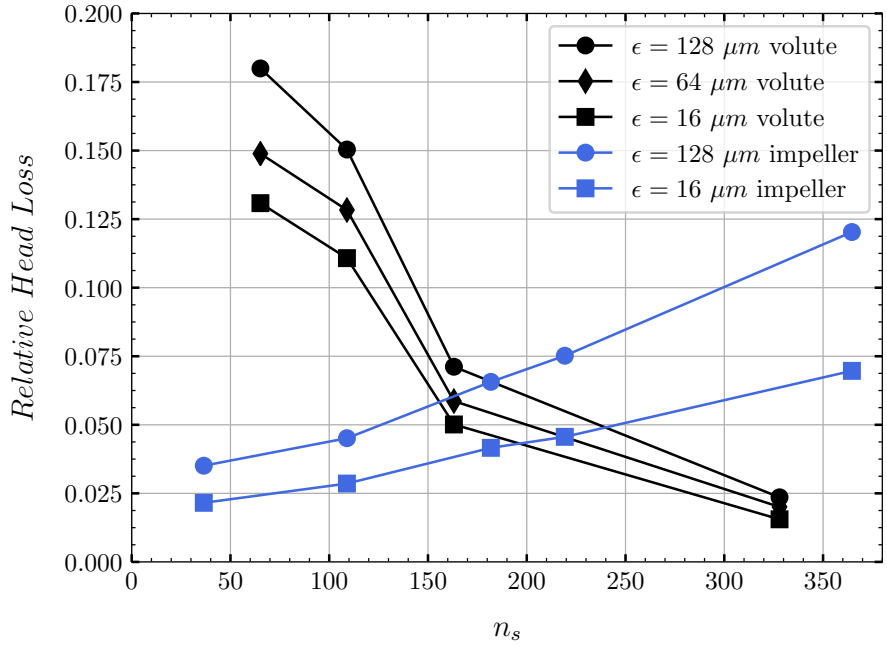

Figure 2.3: Head loss per stage vs. Specific speed with influence of roughness for the volute (black lines) and impeller (blue lines). Adapted from [1].

2.1.1. Volumetric efficiency

The volumetric efficiency represents the percentage of the flow at the outlet of the pump divided by the flow rate in the impeller, see equation 2.1.

$$\eta_{vol} = \frac{Q}{Q + Q_{sp}} \tag{2.1}$$

The additional flow in the impeller comes from the impeller outlet. The backflow (see Q_{sp} $[m^3 \cdot s^{-1}]$ in figure 2.2) travels back to the inlet of the impeller via the sidewall gap on the shroud side.

Estimation of the volumetric efficiency is poorly referenced in the literature at low n_s, but a simple formula, see equation 2.2, proposed by Gülich [1], helps understanding its behaviour with decreasing specific speed:

$$\eta_{vol} = 1 - \frac{4.1}{(n_s/3.65)^{1.8}} \tag{2.2}$$

Although inaccurate, this formula, plotted in figure 2.4, shows an asymptotic behaviour at low specific speed. The low volumetric efficiency η_{vol} is simply explained by two facts:

- The backflow Q_{sp} is a direct function of the impeller pressure rise.
- The mean flow Q in low specific speed pumps is small.

The large pressure at the outlet of the impeller drives a portion of the flow back to the inlet of the impeller (at low pressure) via the sidewall gap on the shroud side. As the main flow is, by definition of low specific speed pumps, small, the back flow Q_{sp} represents a consequent part of the main flow Q. Hence a low volumetric efficiency as per equation

2.1. Any decrease in low volumetric efficiency represents a net pump efficiency loss. The impeller transfers power to recirculated flow that is dissipated in the gaps.

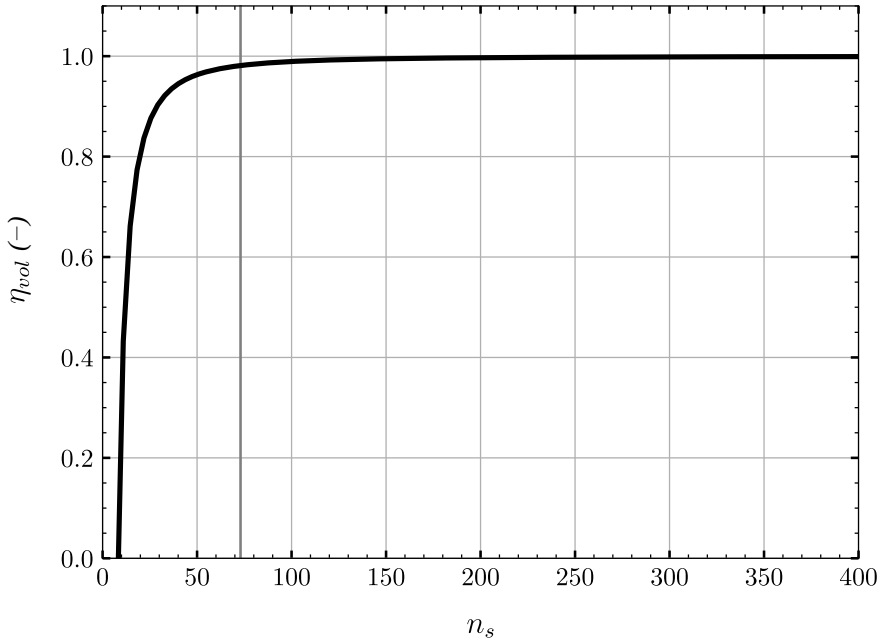

Figure 2.4: Volumetric efficiency vs. Specific speed.

2.1.2. Impeller secondary flow

The flow in low specific speed impellers is almost completely radial due to its large diameter and narrow meridional section. A common feature found at low n_s is a local eddy located on the pressure side of the blade, figure 2.5.

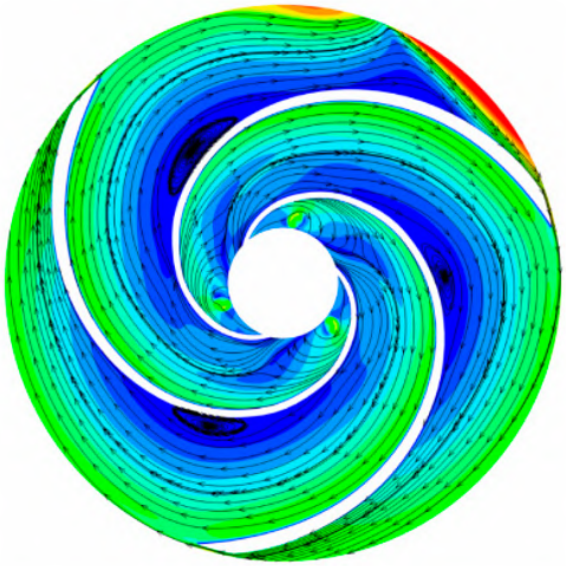

Figure 2.5: Local eddy in a low specific speed pump at design point [9].

The development of this local eddy can be understood by looking at a simple model of the accelerations acting on a fluid element in a radial impeller travelling on a streamline,

figure 2.6. The displacement of a streamline depends on the equilibrium of accelerations perpendicular to the streamline. The centrifugal acceleration ($\omega^2 R$ in figure 2.6) has a component acting in the streamline direction (b_{z1}) and a component acting perpendicularly to it (b_{z2}). The acceleration b_{z3} results from the streamline curvature and is perpendicular to the streamline. The Coriolis acceleration b_c is by definition perpendicular to the streamline, and acting opposite to b_{z2} and b_{z3}.

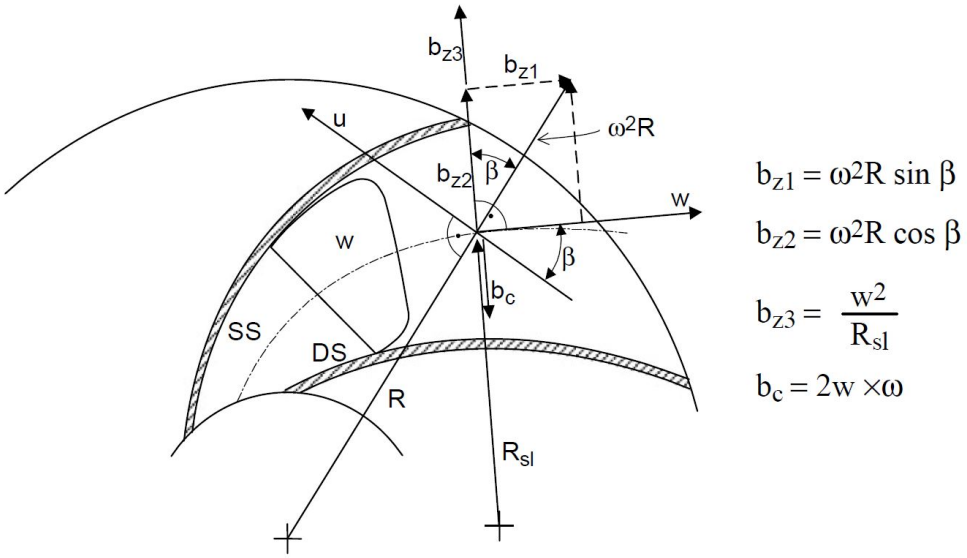

Figure 2.6: Accelerations acting on a fluid element in a radial impeller [1].

The ratio $(b_{z2} + b_{z3})/b_c$ determines whether a fluid element is deflected towards the suction or the pressure surface of the blade. This ratio is the Rossby number. If the Rossby number is near 1.0, no noticeable secondary flow would be expected. If it is smaller than 1.0, the Coriolis force predominates and the flow is deflected in the direction of the blade pressure surface. If it exceeds 1.0, the secondary flow transports fluid to the suction surface of the blades. Because centrifugal forces dominate at low specific speed and the relative velocity w is small, the streamlines are deflected towards the suction surfaces of the blade and the volume of the impeller being too large for the flow, an eddy develops by continuity on the suction side. This eddy acts as a solid and rotates with the impeller. Large momentum exchanges between the "healthy" streamlines and the eddy occur, although those losses are small compared to friction losses. A more problematic outcome of this eddy is the flow at the outlet of the impeller which has a jet-wake pattern, i.e. exits at high speed on the suction side and low speed on the pressure side. Such non-uniformity has an influence on the flow downstream the impeller, in the volute, and may also affect pressure pulsations.

2.1.3. Disk friction

Disk friction losses are generated on a hub and a shroud of the impeller, which represents the rotating wall of sidewall cavities. It is caused by shear stress arising on the surfaces. It can influence the overall efficiency significantly, especially in the case of low specific speed hydraulic machines [10]. The typical pump power losses due to disk friction typically reach about 50% of the useful power [11] in the case of specific speed $n_s = 35$. The losses

gain importance in off-design conditions, especially at part-load, for which the flow rate is low and hence the hydraulic power developed by the pump.

The estimation of power losses due to friction P_{RR} is difficult due to the complexity of the flow in the gaps. Gülich [11] investigated and derived equations able to give an estimation of the disk friction losses in a real impeller. Based on figure 2.7, for $\delta < 45°$ and $Re > 10$, the friction power is expressed as:

$$P_{RR} = \frac{k_{RR}}{cos\delta}\rho\omega^3 r_2^5 \left[1 - \left(\frac{r_1}{r_2}^5\right)\right] \tag{2.3}$$

where k_{RR} is a friction coefficient determined experimentally and depends on the Reynolds number, surface roughness, axial gap, boundary layer and leakage flow. The complete calculation procedure of each term is presented in [1]. Although the calculation considers many geometrical and flow parameters, Gulich estimates a tolerance of $\pm 25\%$ in loss predictions. For that reason, nowadays, numerous authors use CFD for the determination of disk friction rather than an empirical approach, see e.g. [12, 13, 14, 15].

Figure 2.8 presents the portion of power loss due to disk friction and shows an asymptotic behaviour at low n_s. Similar to low volumetric efficiency, the small flow rate of low specific speed pumps implies a relatively small fluid power which is a function of the flow rate. With the disk friction power losses P_{RR} being independent of the mean flow rate of the pump, their relative importance increases with lower flow rate.

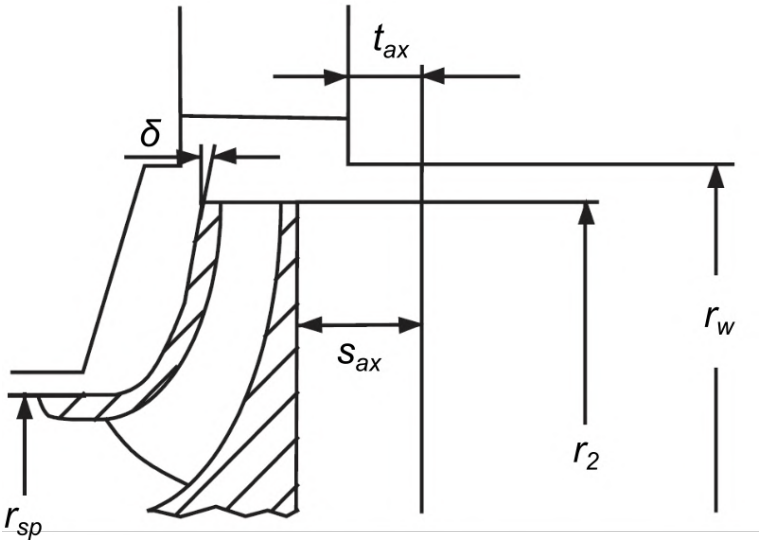

Figure 2.7: Variable for disk friction calculation [11].

2.1.4. Volute losses

The main flow in the volute presents no major difference with classic specific speed volutes. The main flow is circumferential, as the spiral guides the flow at the outlet of the impeller. Due to the superposition of the main flow with the radial component of the impeller outflow and the acting centrifugal forces, a vortex system forms as secondary flow, see figure 2.9. This secondary flow escapes to the sidewall gaps and tightly connects the flow from the impeller, volute and gaps.

The losses occurring in the spiral are frequently separated in the literature into losses of the main and secondary flow. The dominant friction losses of the main flow are estimated

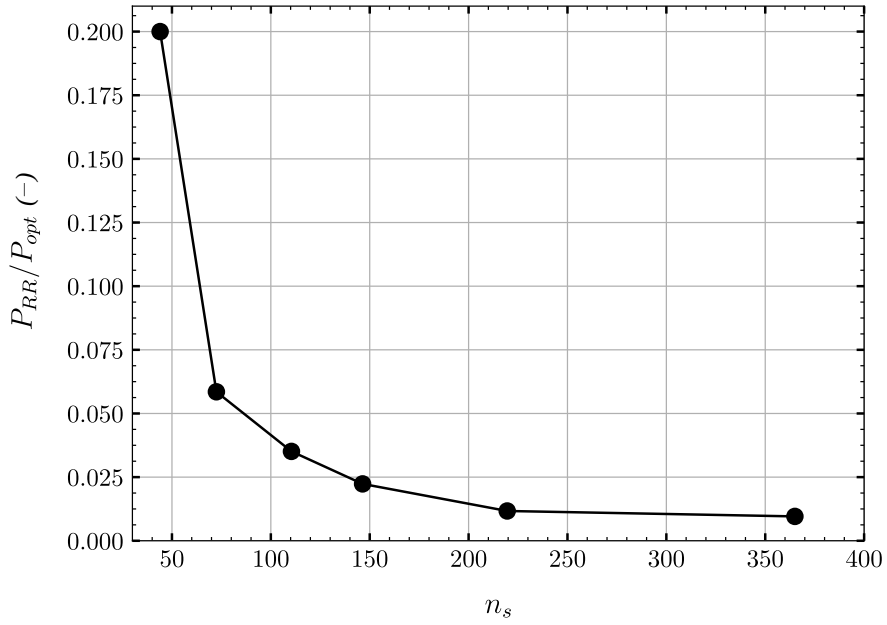

Figure 2.8: Relative power loss due to disk friction as a function of the specific speed. Adapted from [1].

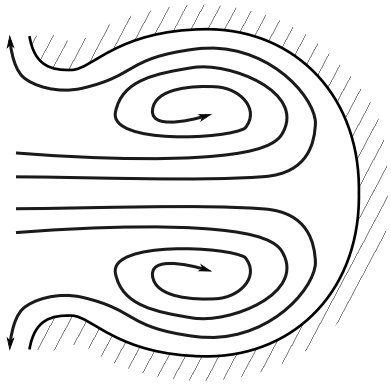

Figure 2.9: Secondary flow volute [16].

in analogy to the flat plate or pipe flow with one-dimensional models [1, 17, 18, 19]. The friction losses $\Delta h_{L,vol}$ of the main flow in the volute are calculated as:

$$\frac{\Delta h_{L,vol}}{H} = f \frac{L_{vol}}{D_{vol}} \frac{c_u^2}{2gH} \tag{2.4}$$

With f as the friction coefficient, L_{vol}/D_{vol} is ratio of the developed volute length by its average diameter and c_u is the circumferential velocity resulting from the flow at the impeller outlet.

However, in 1963 already, Worster [20] insisted that this formulation is not accurate and that using a slightly different definition for the losses leads to better loss predictions:

$$\frac{\Delta h_{L,vol}}{H} = f \frac{S_{vol}}{A_{vs}} \frac{c_u^2}{2gH} \tag{2.5}$$

The ratio L_{vol}/D_{vol} is replaced by S_{vol}/A_{vs}, where S_{vol} is the wet area of the volute and A_{vs} is the volute throat area. The idea of the two formulas is similar. A long and narrow

volute will give large values for L_{vol}/D_{vol} as well as S_{vol}/A_{vs}. This simple theoretical consideration also explains the increasing influence of roughness at lower specific speeds as shown in figure 2.3. A rise in the friction coefficient f has more impact on the volute major head loss at low specific speed because of the increase of the ratio S_{vol}/A_{vs} with lower specific speeds.

In determining the secondary flow losses in the volute $\Delta h_{L,vol,secondary}$, Van Braembussche [19] assumes that the total kinetic energy of the radial component c_{m2} at the outlet of the impeller is dissipated.

$$\frac{\Delta h_{L,vol,secondary}}{H} = \frac{c_{m2}^2}{2gH} \tag{2.6}$$

At the impeller outlet, the radial velocity component c_{m2} has a low value compared to the circumferential component c_{u2}, because the flow rate is small. The secondary flow losses are small compared to the mean flow losses. Figure 2.10 shows the fluid zone of a volute used in this thesis and shows its length relative to its small cross-sectional area. A direct analogy can be made with a pipe of a small diameter, where friction losses are dominant.

Figure 2.10: Volute at a specific speed $n_s = 32$.

2.1.5. Head curve instability

With a low efficiency, the stability of these pumps is the second major hydraulic problem. The stability is a criterion based on the head performance curve. The head should always be decreasing with increasing flow rate, i.e. $dH/dQ < 0$. The pump is called unstable if this criterion is not satisfied. This phenomenon can happen for mid to high specific speed pump at $Q/Q_d = 0.6$ to 0.9, where a saddle appears in the curve. For low specific speed pump, the instability always occurs close to the shut-off point, where the maximum head is located at $Q > 0$. Gülich [1] named this instability the type F instability. Depending on the situation, and especially on the static head, it is possible that the system curve crosses

twice the head curve if the latter one is unstable, as seen with the second system characteristics (red curve) in figure 2.11. Under specific conditions, the flow rate in the system may oscillate between the two solutions, creating large vibrations, pressure pulsations, and would eventually permanently damage the pump or other hydraulic components.

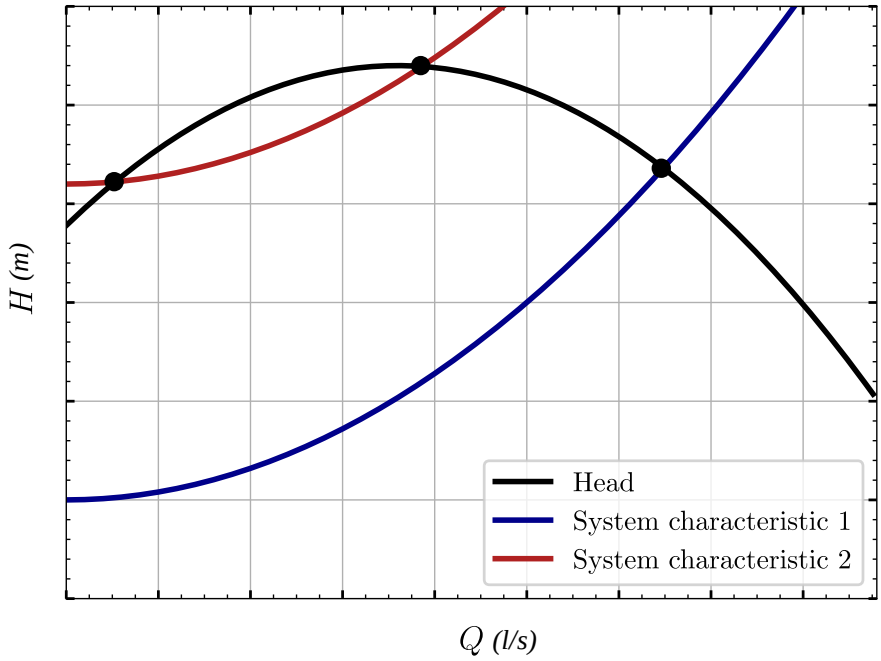

Figure 2.11: Schematic representation of a stable (blue) and unstable (red) system.

The origin of head curve instability is detailed in the next sections first by looking at theoretical considerations inherently flattening the head curve at low specific speed, and then looking at flow phenomena at the inlet and volute leading to the instability.

Theoretical head curve

Theoretical considerations from Worster [20] help understand the flat head observed in low specific speed pump. He wrote equations to find the BEP of a pump by intersecting the theoretical impeller head characteristic Ψ_{imp} with the theoretical volute characteristic Ψ_{vol}.

$$\Psi_{imp} = h_0 - \frac{Q/u_2}{\pi d_2 b_2 tan(\beta_{2B})} \tag{2.7}$$

$$\Psi_{vol} = \frac{2\sqrt{A_v}/d_2}{\ln\left(1 + \frac{2\sqrt{A_{vs}}}{d_2}\right)} \frac{Q/u_2}{A_{vs}} \tag{2.8}$$

Where h_0 is the Busemann head coefficient which is a function of the impeller blade angle and the number of blades, u_2 the blade tip velocity, β_{2B} the impeller outlet blade angle and A_{vs} the volute throat area. The impeller characteristic is mainly governed by the outlet blade angle and the volute characteristic by the ratio $\sqrt{A_{vs}}/d_2$.

For backward swept blades ($\beta_{2B} < 90°$), the impeller head decreases with the flow. The assumptions for the calculation of the impeller head characteristics are a frictionless impeller with parallel hub and shroud, logarithmic blades and zero whirl. The volute

has a rising head characteristic, (eq. 2.8). The point of intersection is the only one that satisfies the requirements of both the impeller and the volute, and gives the position of the BEP. Although these limitations may be far from a real impeller geometry, this model has been shown to predict accurately the best efficiency point for classic specific speeds, see Worster [20], and low specific speeds with Kurokawa [21] or Kagawa [22]. Figure 2.12 shows an estimation of the BEP based on the presented formulas with the experimental BEP. A single volute is tested with different impellers where the number of blades varies from 2 to 12.

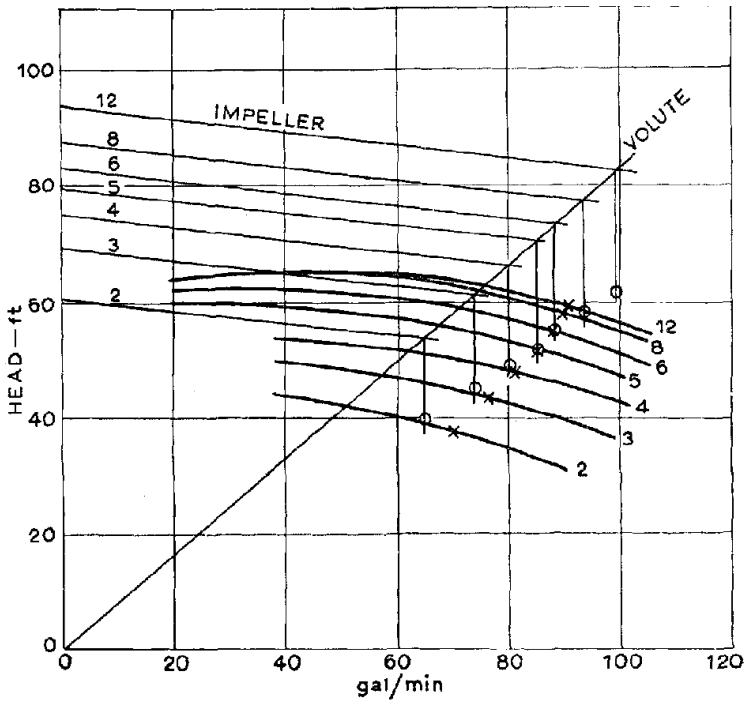

Figure 2.12: Estimation of BEP based on formulas 2.7 and 2.8 (hollow circles) with experimental BEP (cross) [20].

To illustrate the fact that the characteristics of low specific speed pumps is flat, an example is shown in figure 2.13 with 2 test case pumps of $n_s = 32$ (pump used in the thesis) and $n_s = 110$ (considered a high efficiency radial pump). By choosing a similar number of blades and outlet blade angles, the impeller characteristics are similar for both cases and even overlap. The volute head coefficients are different. At $n_s = 32$, the characteristic raises abruptly. The volute characteristic is governed by the ratio $\sqrt{A_{vs}}/d_2$, a much smaller ratio in the case of low specific speed pumps which presents a small volute throat area and a large impeller diameter. As a result, the predicted BEP for the case $n_s = 32$ is reached at a lower flow coefficient, where the head drop between shut-off and BEP is small. At the estimated BEP, the flow coefficient is 0.05 for the pump $n_s = 32$ and 0.12 for the pump $n_s = 110$. The drop in head coefficient between the shut-off head and the BEP is 0.11 at $n_s = 32$ and 0.25 at $n_s = 110$. At $n_s = 32$, the drop in head coefficient is about 2.4 times lower than at $n_s = 110$. This inevitably translates into a flatter head curve.

Although the predicted shut-off head by this model does not match real pumps shut-off head, it shows that theoretically, the head characteristic of pumps flatten with lowering specific speed.

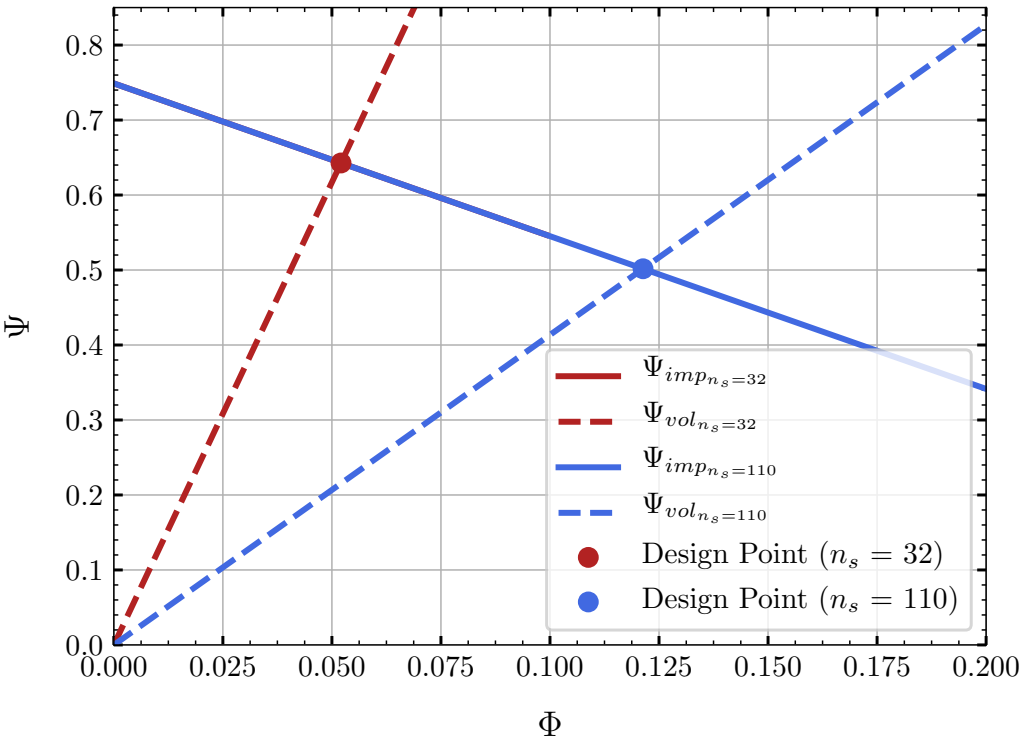

Figure 2.13: Theoretical BEP according to Worster [20].

Inlet phenomena

If low specific speed pumps inevitably have a rather flat head curve, it does not imply an unstable head characteristic. Loss phenomena at partload are responsible for head instability. At the impeller inlet, two flow features may lead to an unstable head curve.

Pre-rotation

A considerable fraction of the fluid flows back from the outlet of the impeller to the inlet, as seen in previous sections. The volumetric efficiency can drop below 50% at $Q/Q_d \leq 0.3$, meaning that more than half of the flow at the impeller inlet is recirculated flow. The backflow Q_{sp} has a rotating component thanks to the shroud rotating wall in the sidewall gaps. The fluid, rotating in the same direction as the impeller, induces pre-rotation at the inlet of the impeller, directly reducing the head as per the Euler's pump equation (eq. 2.9), by introducing a circumferential component c_{1u} upstream the impeller as seen in 2.14, case *a*.

$$gH = u_2 c_{2u} - u_1 c_{1u} \tag{2.9}$$

Head rise by recirculation

Pre-rotation impairs the head, but the backflow from the sidewall also has a positive effect of the head at low flow. Due to the backflow to the impeller inlet from the sidewall gap, recirculation always appears close to the shroud in the impeller eye. This recirculation region shifts the effective streamline at partload towards the hub by a distance Δd (see

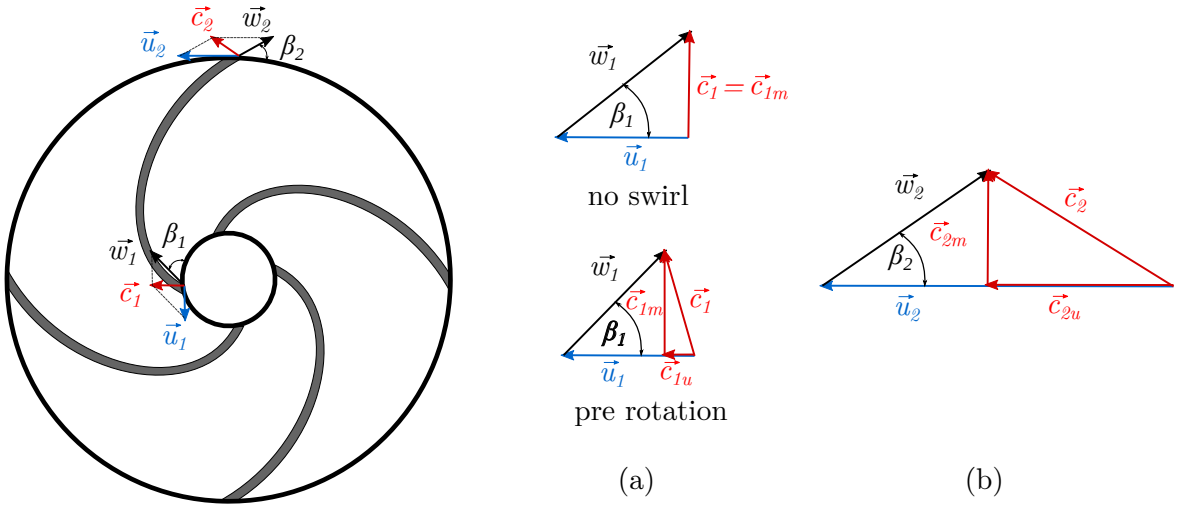

Figure 2.14: Velocity triangle at impeller inlet and outlet. Adapted from [1].

figure 2.15), and the pump benefits from a slight head gain due to additional centrifugal force. The partload head gain due to recirculation, noted H_{Rec}, is estimated as:

$$H_{Rec} = \frac{u_2^2}{2g}\left(\frac{\Delta d^2}{d_2^2}\right) \tag{2.10}$$

For low specific speed pumps, the narrow meridional section implies small values of Δd. Also, the impeller diameter d_2 is large and reduces this effect furthermore. As a consequence, the head gain H_{Rec} becomes negligible and low specific speed pumps do not effectively benefit from this flow feature.

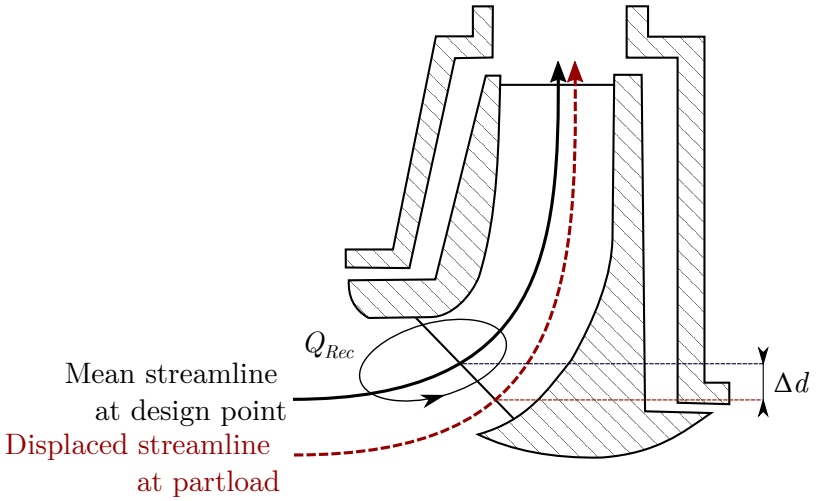

Figure 2.15: Inlet recirculation. Adapted from [1].

Flow approaching the tongue

Wo and Bons [23] investigated experimentally the flow in a pump of specific speed $n_s = 62$. The objective of the study was to identify the onset of instability rather than solving it. The experimental setup and main results are shown in figure 2.16.

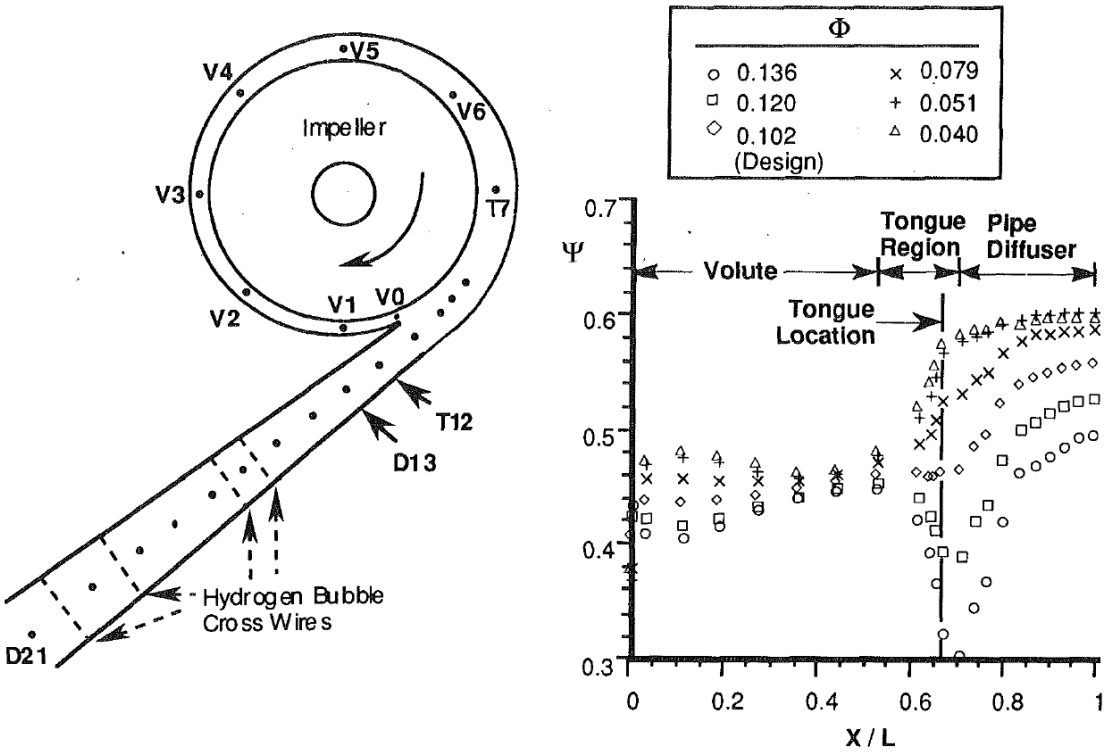

Figure 2.16: Pressure tap locations (left) and meridional variation of static pressure rise (right) [23].

The right part of figure 2.16 presents the evolution of the pressure from the tongue to the outlet pipe. The pressure evolution in the first portion of the volute is essentially flat at all flow rates. This is true from tap $V1$ to tap $T7$, which are located respectively at 15° and 285° from the tongue. From tap $T7$, the pressure decreases for high flow coefficient and increases for low flow coefficient. The volute at partload acts as a diffuser in its last portion. After tap $V7$, a fluid particle will prefer the recirculated path leading to the impeller-tongue gap rather than flowing into the diffuser thanks to a bigger positive pressure gradient. This recirculation is confirmed by Wo by injecting air bubble close to the tongue of the volute, and a reverse flow region is observed as seen in figure 2.17. The recirculated flow causes additional losses at partload.

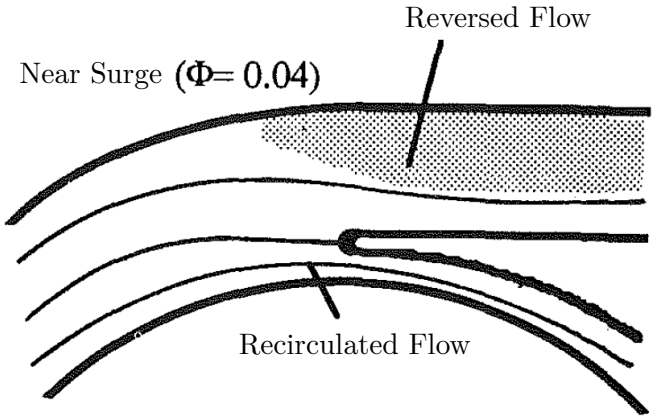

Figure 2.17: Flow pattern near the tongue region near instability [23].

Conclusion about instability

As a result, several flow phenomena may cause a head instability at partload for low specific speed pump:

- The head naturally flattens with diminishing specific speed.
- The important back flow Q_{sp} causes pre-rotation and reduces the head at partload.
- A positive flow feature displacing the effective streamline towards the hub allows for a head gain H_{Rec}. Due to the narrow meridional section, this phenomenon is small for low specific speed pumps.
- Additional losses are caused by the flow from the volute driven to the impeller/tongue gap due to a positive pressure gradient.

The stated points are qualitative only, as it is difficult to quantify the influence of each statement. It should be noted that the second and third point (inlet losses) are assumed to be responsible for small flow losses as they are proportional to the blade inlet velocity u_1, a value way smaller than u_2 due to the high ratio d_1/d_2 in low specific speed pumps. However, as the head is naturally flat, any losses close to shut-off point can cause instability.

2.2. Solutions Applied to Low Specific Speed Pumps

Kurokawa et al. [21] is one of the first that has done an extensive work on low specific speed pumps. He experimentally tested 12 combinations of 6 impellers with 2 volutes based on Stepanoff [2] design. The specific speeds ranged from $n_s = 40$ to 55. The tested impellers have various outlet blade angles β_{2B} (23°, 60° and 90°) and outlet width b_2 (6 and 8 mm). The two volutes have different inlet width b_3 (19 and 35 mm). The influence of the parameters is clear. Increasing the blade outlet angle β_{2B} and width b_2 increases the head and causes stronger instability. Increasing b_3 raises the efficiency, head and instability. These results are expected. A great effort in enhancing performances of low specific speed pumps is based on modification of the impeller. As seen in section Impeller secondary flow, the local eddy creating the jet-wake flow pattern is common and has been observed by, e.g. [24, 26, 27, 28]. The resulting poor outlet flow condition enhances the mixing losses in the volute. Improving the flow at the impeller outlet has been a focus of many researchers and the main solution used is the addition of splitter blades in the flow passage.

2.2.1. Splitter blades

Miyamoto et al. [29] stated that, in centrifugal impeller, it is expected that as the number of blades increases, outlet pressure and efficiency increase. However, a large number of blades (typically, $Z \geq 8$), increases the blockage and skin friction in the impeller passage counterbalancing the benefit of a great number of blades. Splitter blades are a solution, allowing an increase of blades without impairing the inlet blockage. The jet-wake flow pattern described above can be reduced or suppressed with additional blades in the passage. Many researchers have analysed their influence considering different parameters, for different pump specific speeds.

In fact, splitter blades have been the most common solution to help breaking the jet-wake flow in low specific speed impellers. Splitters are known to introduce a decrease in efficiency due to additional friction in the impeller while having a positive impact on the head as found by Golcu [30] for a pump with $n_s = 152$ and Kergoulay [31] for a pump with $n_s = 117$. But at low specific speed, the impeller plays only a small role in the efficiency of the whole pump (see fig 2.3) and the introduction of disruptive elements does not necessarily induce an efficiency loss. In some cases, the efficiency even increases thanks to the improved flow condition at the impeller outlet provided by splitter blades.

Cui et al. [24] investigated experimentally and numerically an impeller with a specific speed of $n_s = 18$. The initial impeller has 4 blades, and different splitter blades were added to have a total of 8, 16 and 24 blades, see figure 2.18. At such extreme specific speed, the backflow region in the four-bladed impeller is so large that the fluid flows near the outlet of the impeller only close to the suction side. As the number of blades raises, the recirculation regions are reduced, leading to a more uniform outlet flow. The efficiency improved with increased number of blades and the head becomes extremely flat, but stable, for the 24-bladed impeller.

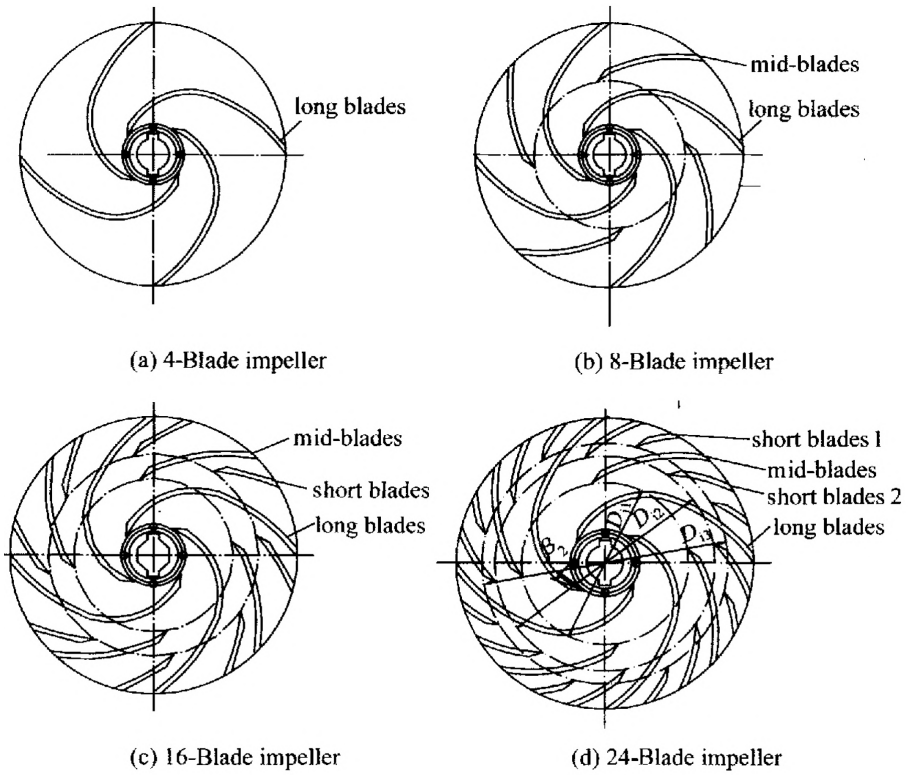

Figure 2.18: Multi-split blades at $n_s = 18$ [24].

Li [25] also used the multi-split blade technology to solve the reverse flow in the impeller in a pump with a specific speed $n_s = 13$ and showed that the addition of blades helps increase the pump head and control the reverse flow. However experimental results are missing.

Yuan et al. [32] worked extensively on splitter blades and summarized his work on the splitter blades design for low specific speed pump using CFD, PIV and orthogonal experiments. He tested pumps with specific speeds from $n_s = 47$ to $n_s = 78$. He concluded that the effect of splitter blades on low specific speed pump is as follows:

- The BEP is shifted at high flowrate, raising the specific speed of the pump.
- The head is increased at high flow rate.
- The power consumption is increased at high flow rates.

This results in a head flattening, and sometimes in the introduction of instability. Zhang [33], Ye [34] and Zhang [35] confirm the previous points by studying pump with specific speeds between $n_s = 44$ and $n_s = 58$.

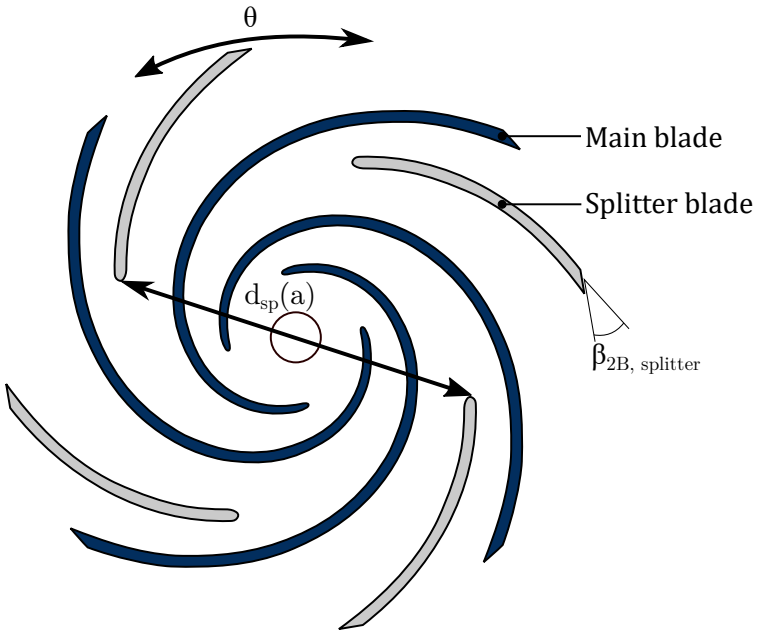

Figure 2.19: Splitter blades parameters.

Yuan et al. [32] also created a design procedure for placing splitters in low specific speed impellers, based on parameters seen in figure 2.19:

- The number of main blades should be 4 for maximum efficiency.
- The inlet diameter of splitter blades has limiting values. The maximum length of splitter is limited by inlet blockage. On the opposite side, a small splitter does not solve the jet-wake flow pattern.

$$d_{sp} = \left[a \left(1 - \frac{d_1}{d_2} \right) + \frac{d_1}{d_2} \right] d_2 \tag{2.11}$$

  With $d_1/d_2 \in [0.2 - 0.4]$; $a \in [0.5 - 0.6]$
- Splitter deviation θ: This parameter places the splitter circumferentially in the channel and takes values between 0 (suction side of the main blade) and 1 (pressure side of the main blade). The velocity in the impeller passage in the circumferential direction is not uniform, so the splitters cannot be set at the middle of flow passage. They need to deviate towards the main blades suction side to improve the flow structure of "jet-wake", the pump performance and have an evenly flow rate repartition in the blade channel. The recommended deviation is $\theta \in [0.30 - 0.35]$.

- Deflection of splitter α_{sp}: This parameter controls the splitter outlet blade angle.

$$\alpha_{sp} = \beta_{2B,splitter} - \beta_{2B,main} \tag{2.12}$$

  A splitter outlet deflection angle of 5°, so $\alpha_{sp} = +5°$ gives the best pump performance. However, this parameter has not been studied deeply.

2.2.2. Special designs

Based on the principle that the work transfer in radial impellers of low specific speed (i.e. with a small ratio d_1/d_2) is largely accomplished by centrifugal forces, a series of special, usually simpler impellers, has been designed. They take advantage of the fact that the inlet losses are insignificant.

Circular blades

At specific speeds below $n_s = 59$ to 66, untwisted blades can be designed. Cylindrical blades, or 2D blades, imply virtually no loss in efficiency. However, if good cavitation characteristics are required, twisted blades must be employed. Circular arc blades of this type result in an unfavorable development of the relative velocity which is decelerated to a value $w < w_2$ within the impeller channel and it might jeopardize the stability of the Q-H-curve [1].

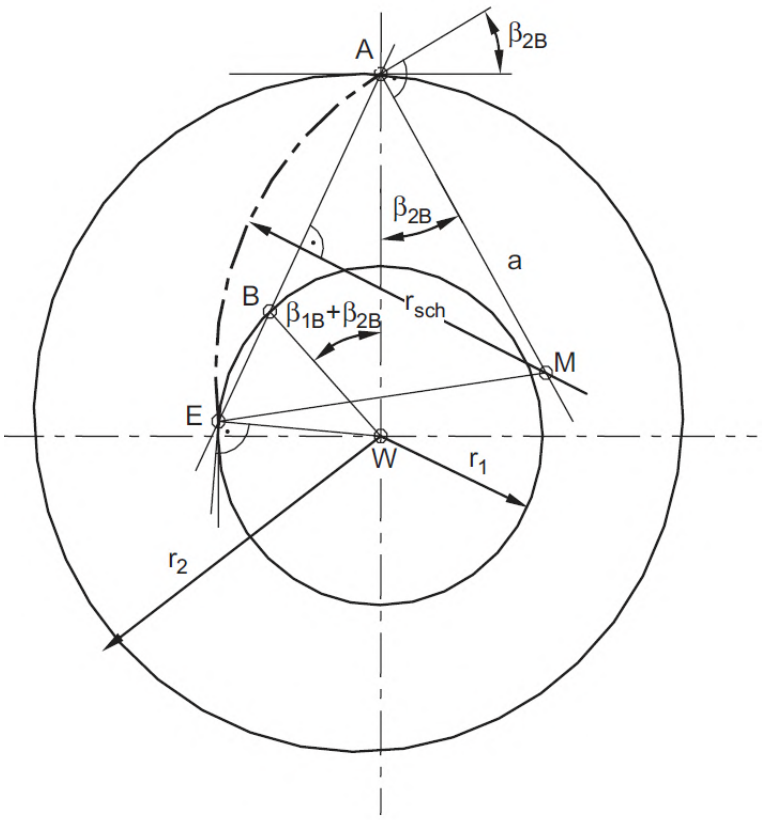

Figure 2.20: Construction of circular blades [1].

Pumping disks with channels of circular sections

A rotating disk with cylindrical holes can be employed as an impeller. The holes are drilled in the radial direction so that $\beta_{1B} = \beta_{2B} = 90°$. The angle can also be chosen lower than 90° for a steeper head curve. Generally, below the BEP, the head is totally flat and unstable close to shut-off. At overload, the head decreases almost vertically because of a cavitating flow in the diffuser [1].

Benigni [36] used this design in a commercial project where the customer insisted on a simple and reliable design. The pump, see figure 2.21, has a specific speed of 13.5 and reached an efficiency of 30%.

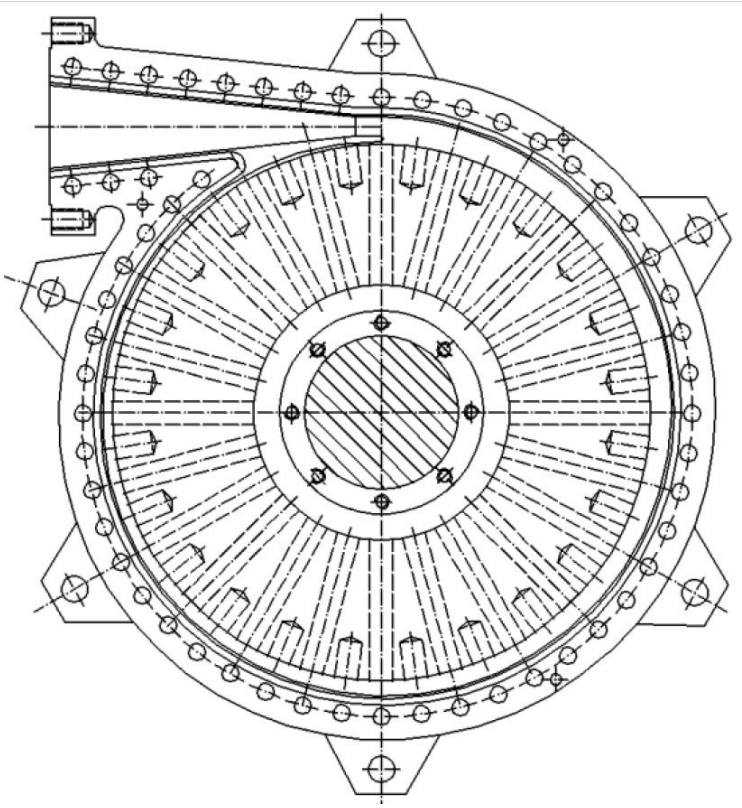

Figure 2.21: Cross-section of pierced disk [36].

Impellers with straight radial blades

In the range of specific speeds from $n_s = 22$ to 44, straight radial blades are often equipped with an annular casing. The impeller possesses a large number of blades, typically 16, 24 or 32, is semi-open to reduce disk friction and has a high outlet width. The hydraulic characteristics are similar to pumping disks with drilled holes, unstable, with an efficiency that can reach up to 45% [1].

Double-acting impeller with straight radial blades

Used for high head, above 300 m, this type of pump showed an efficiency of 50% at $n_s = 33$, benefiting from the lack of disk friction, with a sharp drop in efficiency at lower specific speeds. The head characteristics are usually totally flat, but not unstable. Since flow conditions on both sides of the impeller are very similar, the axial thrust is balanced to a

large extent. Operation on the right of the best efficiency point is limited by cavitation in the collector [1]. The impeller meridional section and 3D-view can be seen in figure 2.22.

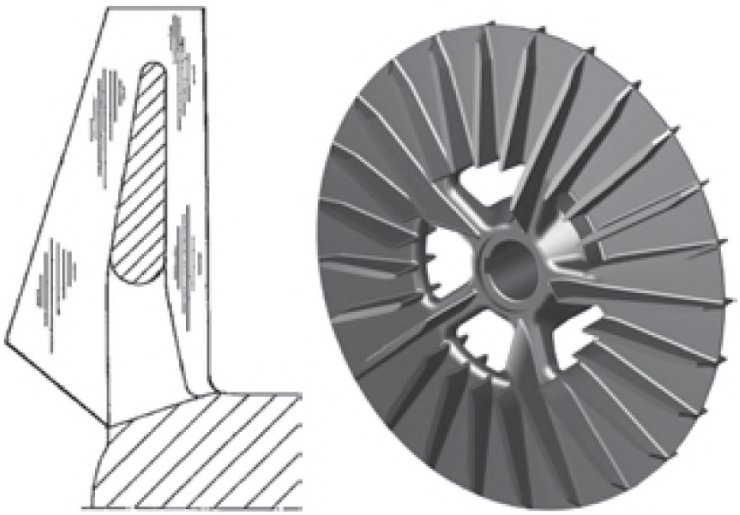

Figure 2.22: Double acting impeller [1].

Thick trailing edge and recirculation channels

Klas et al. [5] [6] studied an impeller with thick trailing edge (figure 2.23), such that the flow passage is narrow with an almost constant cross-section. The idea of such impeller shape is to suppress the impeller vortices. The same impeller was tested with recirculation channels, which were seen to rise the head. The shape of the recirculation channel on the stability was studied and T-shaped channels showed the best stability, however, the total and hydraulic efficiency is smaller compared with other types of impellers.

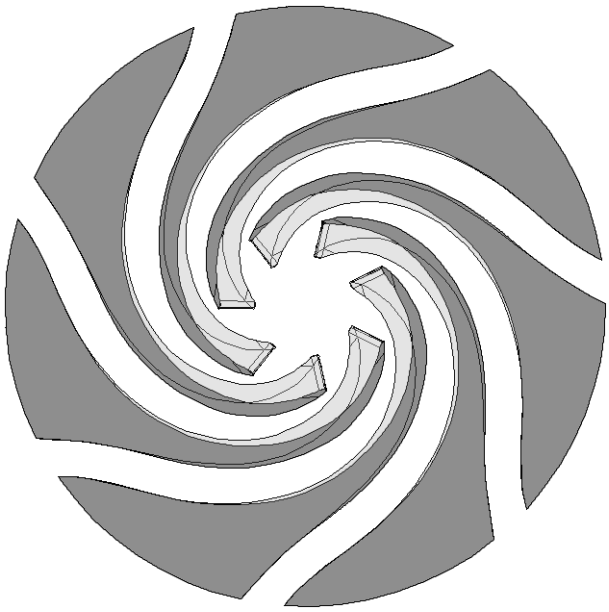

Figure 2.23: Thick blades [7].

2.2.3. Volute

Despite being an important source of losses, the volute is scarcely studied at low n_s. Kagawa et al. [22], started with the principle that at low specific speed, the volute influences the most the pump losses (apart from disk friction) and the position of the BEP. He tested a circular casing, as opposed to classic volute design with increasing area. The design specific speed of the tested pump was $n_s = 27$. Using a circular casing, as opposed to a classic volute, improved both the head and the efficiency, while introducing more instability at partload, see figure 2.24.

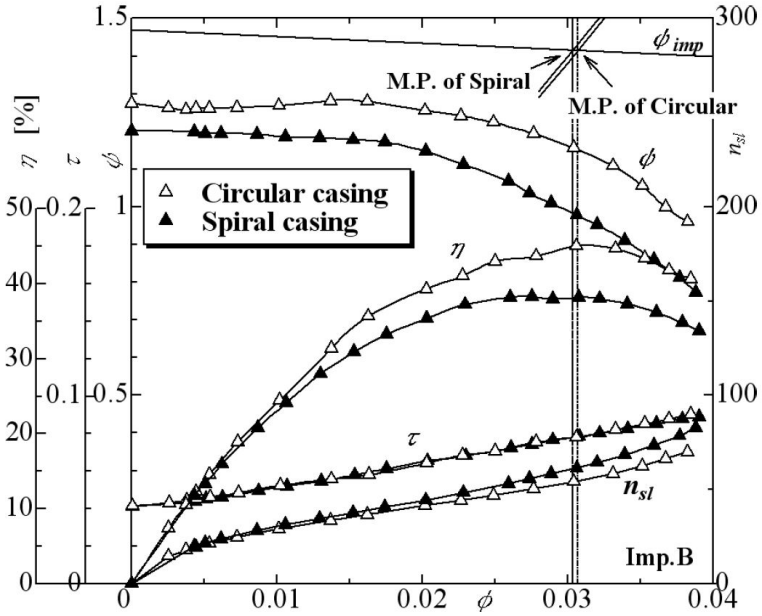

Figure 2.24: Influence of casing type on pump performance [22].

Different tested impellers revealed that the influence of the impeller on the performance (head and efficiency) is very small at such low specific speed. Four impellers were tested with outlet blade angles varying from 30 to 90° and a different number of blades (4 or 6 blades). However using a higher outlet blade angle made the head more unstable, as expected. To reduce the specific speed even more, a spacer was introduced in the circular casing, reducing the volute throat area. The BEP is shifted to lower flow rates, as the specific speed decreases and the head becomes more unstable.

2.3. Closure

This chapter presented the specific challenges that a centrifugal low specific speed pump faces from a hydraulic point of view:

- **Impeller:** With a large diameter and a narrow meridional section, the equilibrium of forces in a low specific speed impeller leads to a flow deflection towards the pressure side of the main blade. As a result, a local eddy develops on the blade pressure side impairing the flow in the impeller and the discharge flow into the volute.

- **Volute:** To accommodate to the large impeller diameter and low flow rate conditions, low specific speed volutes are long and narrow. The friction losses are largely dominant and contribute to a significant part of the total pump losses.
- **Sidewall gaps:** Disk friction is the main source of losses in low specific speed pumps. They can account for more than 50% of the pump losses. The flow in the gaps is complex and no simple formula can accurately predict the losses. The power loss in the gaps is largely independent from the flow rate, further aggravating the impact of the disk friction losses at partload.
- **Head curve instability:** The inherent design of low specific speed pumps make them susceptible to partload head instability.

The design solutions to overcome the stated problems are then presented.

- **Splitter blades:** Additional, smaller blades placed in the impeller channel help breaking the local eddy in the impeller. Additionally, they help raising the pressure developed by the pump without blocking the impeller inlet. This allows for a reduction in diameter and a diminution of disk friction losses.
- **Special designs:** Special designs are presented and often side step from classic impeller design to either ease manufacturing (e.g. pump with drilled holes), suppress disk friction (e.g. double-acting impeller with straight radial blades) or suppress the possibility of secondary flow in the impeller (e.g. impeller with thick trailing edge).
- **Volute:** Circular casing with a constant cross-section has been shown to decrease losses in the volute, at the expense of the pump stability. The volute at low specific speed pump has not been heavily investigated.

Goals

The thesis focuses on hydraulic improvement of low specific speed pump performances and is based on the impeller and volute design. Based on the available literature, the work is focused on the splitter blades design for the impeller. Despite the large amount of research that has already been invested in splitter blades design, rare are the studies presenting their influence on a pump with a specific speed as low as $n_s = 32$. The work will be focused on the influence of the position of a single splitter in a first time, and the addition of a second splitter in the flow passage in a second time. Then, the volute design will also be investigated based on the volute throat area, but also inspect the impact of the spiral development on the flow and performances. The methods used for the described investigation are presented in the next chapter.

3. Methods

Numerical flow simulations are used to evaluate pump performances of all designs investigated in this thesis. Therefore, the simulation of flow is briefly introduced before presenting the turbulence models used in turbo machinery and in this thesis specifically. Numerical simulations are validated with experimental results. The experimental apparatus is then described, along with the manufacturing process of the different parts and the technical problems encountered.

3.1. Flow simulation

3.1.1. Turbulent flows

Real flows are described by partial differential equations which cannot be solved analytically in the general case. By dividing a complex flow domain into a multitude of small cells, these equations can be solved in an approximate manner by numerical methods. Because of their wide range of application, numerical flow calculations ("computational fluid dynamics" or "CFD" for short) have become a special discipline of fluid dynamics.

Most flows and in particular industrial flows are turbulent. Turbulence is described by a chaotic change of field values in space and time. In our case, velocity and pressure. Turbulent flows contain eddies with a range of sizes and energies, see figure 3.1 for a schematic representation.

Such behaviour can be accurately solved with numerical simulation only at the expense of tremendous computing power and only for relatively simple flows (due to computational cost constraints). This method is called Direct Numerical Simulation (DNS).

Large Eddy Simulation (LES) is a mathematical model that reduces the computational cost comparing to DNS by ignoring the smallest eddies and resolving some. Eddies smaller than the mesh are not resolved but modelled with a sub-grid scale model. The mesh therefore sets the minimum eddy size that can be resolved. This type of model is gaining in popularity due to a more widespread availability of large computing power. However the necessary ressources are still considerable.

The more common approach in CFD is the modelling of turbulence rather than a direct solving. The Reynolds averaged Navier-Stokes equations (RANS) or unsteady Reynolds averaged Navier-Stokes equations (URANS) are used for this purpose. The main idea in this model is to separate the chaotic behaviour of field values (see figure 3.1 for velocity) as an average and a fluctuating part.

The unsteady RANS equations for a viscous incompressible fluid are written in equation 3.1. The continuity equation is shown in equation 3.2.

$$\frac{\partial \overline{v_i}}{\partial t} + \frac{\partial \overline{v_i}}{\partial x_j}\overline{v_j} = -\frac{1}{\rho}\frac{\partial \overline{p}}{\partial x_i} + \nu\frac{\partial^2 \overline{v_i}}{\partial x_j \partial x_j} - \frac{\partial}{\partial x_j}\left(\overline{v_i' v_j'}\right) + g_i \tag{3.1}$$

$$\frac{\partial \overline{v_i}}{\partial x_i} = 0 \tag{3.2}$$

where v $[m/s]$ is the fluid velocity, p $[Pa]$ is the pressure, t $[s]$ is the time, ν $[m^2/s]$ the kinematic viscosity of the fluid, x $[m]$ the position, ρ $[kg/m^3]$ the fluid density and g_i $[m/s^2]$ represents external acceleration. In the process of Reynolds-averaging, the

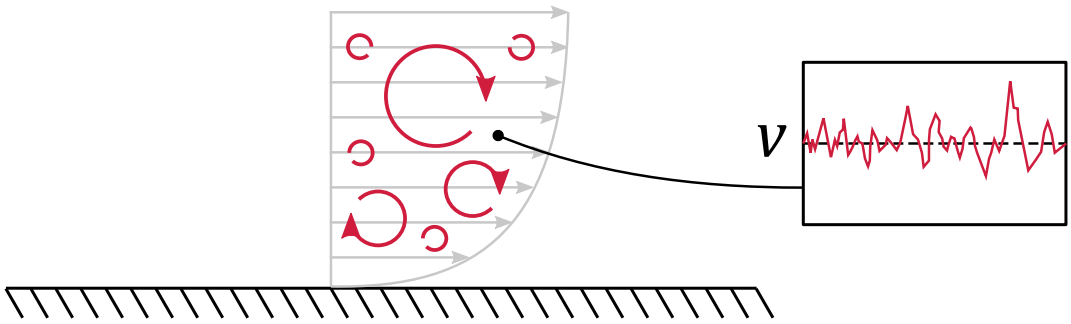

Figure 3.1: Flow eddies and velocity fluctuation in a turbulent flow. Reproduced with permission from [37].

Reynolds stress tensor appears (see equation 3.3). This tensor is unknown and there is a need for turbulence modelling to offer a closure to the problem.

$$\tau_{ij} = \rho\overline{v_i' v_j'} \tag{3.3}$$

3.1.2. Turbulence modelling in turbomachinery

A large number of turbulence models have been developed over the years to satisfy specific needs or improve exisiting models. For example NASA describes and validates more than 20 RANS-turbulence models [38]. Numerical simulations (CFD) are used by engineers to design pumps for decades. The $k-\epsilon$ and the $k-\omega$ SST turbulence models are certainly the most common models used in turbomachinery. Both models include two additional scalar transport equation to the system for k and ϵ or ω depending on the models. These variables physically represent the energy (k), the dissipation (ϵ) and the dissipation rate (ω) of the turbulence and are a statistical representation of the turbulent fluctuations which are not explicitly resolved by the RANS equations. The most popular model used nowadays and the one used in this thesis is the $k-\omega$ SST by Menter [39]. This model is discussed in detail after an introduction to the treatment of variables at the wall.

Wall-treatment

Close to the wall, gradients of velocity and other variables are large. The use of a fine grid resolution is required to accurately resolve the gradients. This method is called the *Low-Reynolds number* method. Usually, this results in cells with high aspect ratio on the wall, reducing the quality of the cell, and a high total cell count. A solution to reduce the cell count at the wall is the use of the *wall-functions* method. The main idea of wall-functions is the modelling of wall gradient rather than a direct solving, see figure 3.2.

Wall functions are the empirical functions that are fitted to the observed behaviour close to the wall, see figure 3.3. The parameter on the x-axis is the non-dimensional wall distance y^+, see equation 3.4.

$$y^+ = \frac{y u_\tau}{\nu} \tag{3.4}$$

With y (m) the absolute normal distance to the wall, u_τ (m/s) the friction velocity and ν (m^2/s) the fluid's kinematic viscosity. The friction velocity is equal to $u_\tau = \sqrt{\tau_w/\rho}$,

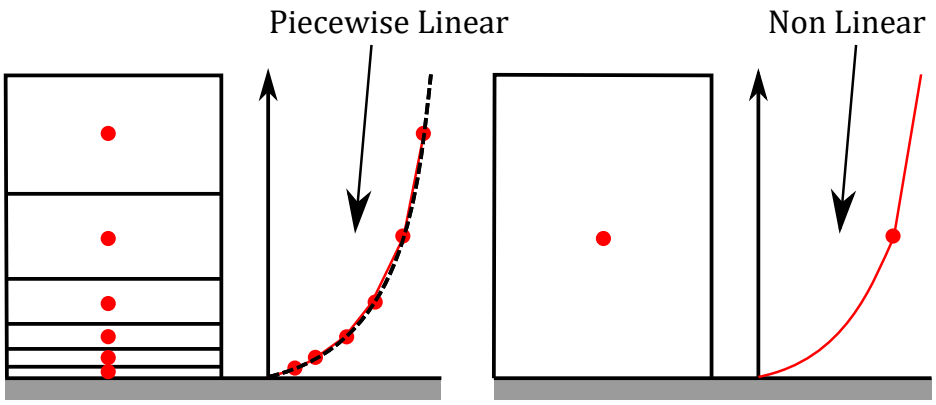

Figure 3.2: Resolved wall gradient (left) and use of wall function (right). Reproduced with permission from [37].

with τ_w (Pa) being the wall shear stress and ρ (kg/m^3) the fluid's density. The parameter on the y-axis is U^+, a dimensionless velocity, equation 3.5.

$$U^+ = u/u_\tau \tag{3.5}$$

with u (m/s) the absolute velocity.

The reference (black line) is obtained from experimental measurements and DNS simulations. With reference to figure 3.3, the standard wall functions are given by equation 3.6 for $y^+ < 5$ (blue line) and equation 3.7 for $30 < y^+ < 300$ (green line).

$$U^+ = y^+ \tag{3.6}$$

$$U^+ = \frac{1}{\kappa} log(Ey^+) \tag{3.7}$$

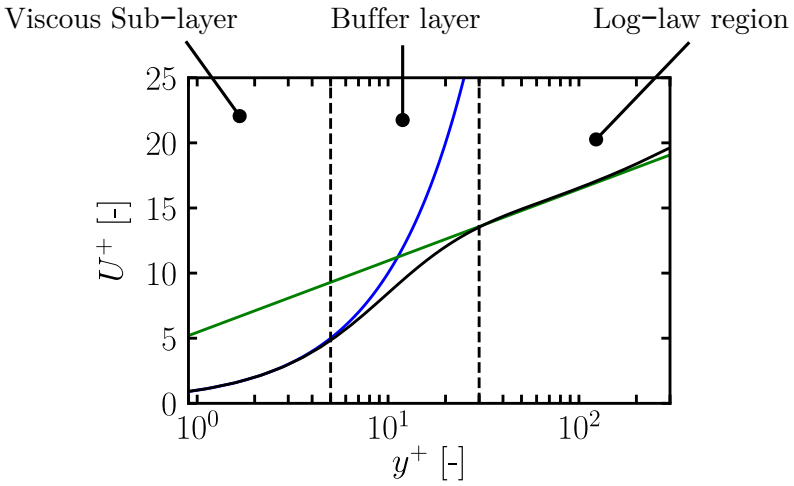

Figure 3.3: Law of the wall. Reproduced with permission from [37].

However, this approach gives large errors in the buffer layer ($5 < y^+ < 30$) and CFD codes do not recommend placing cells in the buffer region. This leads to the construction of two categories of grids, based on the placement of the height of the first cell. Resolved meshes place the first cell in the viscous sub-layer ($y^+ < 5$), and wall-function based

meshes place the first cell in the log-law region ($y^+ > 30$). However, even with an effort placed on the first cell height, there will be zones where y^+ falls in the buffer layer due to the complexity of industrial flows. In practice, most CFD codes use a proprietary blending between the viscous sub-layer and log-law wall functions in the buffer region to limit errors. In the code `ANSYS-CFX`, the `Automatic wall treatment` is the only option and automatically adapts the wall treatment depending on the local value of y^+. The accurate prediction of the velocity close to the wall is critical for the calculation of the wall-shear stress τ_w, and hence the prediction of pressure at walls, onset of flow separation, etc...

Performance prediction using eddy-viscosity models

For turbomachinery applications where the specific speed $n_s > 55$, CFD predictions are often good and lead to a close matching between the simulation and the experiment. For pumps with specific speed $n_s < 55$, discrepancies are observed and effort has been put in the last years to accurately describe low specific speed pump performances by means of CFD. The main actor is Juckelandt [16] and his work will be summarized here.

Juckelandt et al. [8], investigated a pump with a specific speed $n_s = 44$. He showed that the usage of wall-functions on a low specific speed pump leads to erroneous performance prediction (using `ANSYS-CFX`). The turbulence model used was $k - \omega$ SST. When using this model, the predicted BEP is shifted at higher flow rates and the performances at overload are highly over-estimated. He then used the low-Reynolds number method, which requires resolving the boundary layer and compared the results with the experiment. The efficiency computed with different wall treatment methods is compared with the experiment in figure 3.4. The mesh resolving the boundary layer (low-Re) shows a close to perfect agreement with the experiment. The mesh using wall-functions also shows a satisfactory agreement at low flow and at the design point, but fails at high flow. The two meshes have a similar surface mesh. Only the first cell height is changed, to rest either in the viscous sub-layer ($y^+ < 5$) or in the log-law region ($30 < y^+ < 300$). Accordingly, the cell count also changes and a lower number of cells is used for the wall-function based mesh.

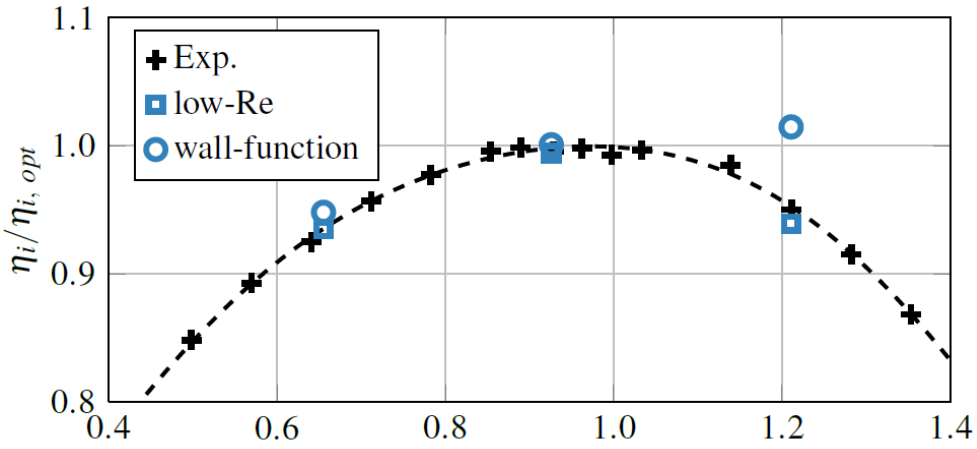

Figure 3.4: Efficiency curve at $n_s = 44$. Wall function (circle) and Low-Reynolds number (square) treatment approach [16].

So, the use of the low-Reynolds number treatment at the wall gave accurate results. This can be understood by looking at the physics of low specific speed pumps. Major discrepancies are observed at overload, where the flow is choked at the tongue due to the small volute throat area. The flow attaches and detaches many times downstream the tongue of the volute, creating a large region of losses. This phenomenon is not captured by the wall-function approach. An illustration of this is visible in figure 3.5, where the turbulence kinetic energy is visualized. In illustration (a), a large zone of turbulence kinetic energy starts at the tongue and is transported in the volute diffuser. This is simply not captured in case (b) which does not capture the onset of separation, resulting in an over-prediction of the performances at high flow.

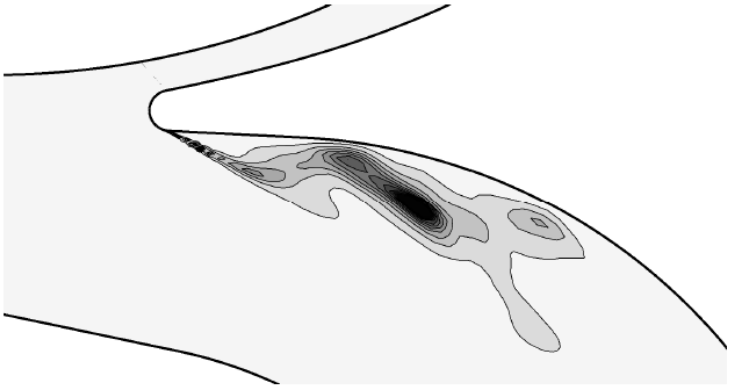

(a) Low-Re method (resolved boundary layer)

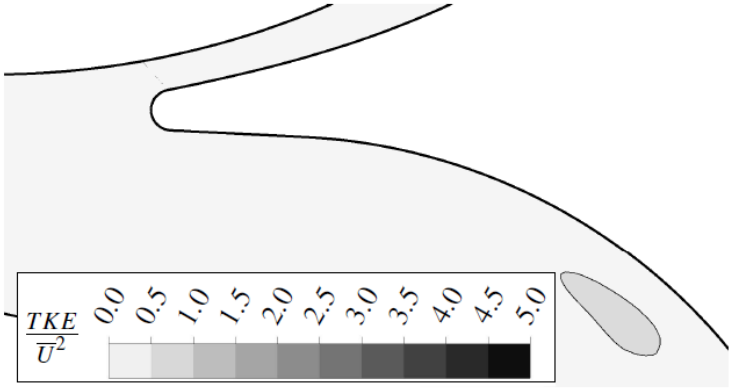

(b) Wall-function method

Figure 3.5: Detachment downstream the tongue at overload indicated by large TKE region [16].

The author also experimentally studied the effect of roughness. Initially, the casing and impeller were manufactured and polished to be hydraulically smooth. To mimic the influence of roughness, transparent adhesive foils were structured with a high-power picosecond laser and placed on the volute wall and outer walls of the impeller. The inside surfaces of the impeller stayed hydraulically smooth. The equivalent sand grain roughness of the structured foils was estimated to be $60\mu m$ [41]. The torque, head and efficiency of the pump with smooth and rough walls were compared. The results are shown in figure 3.6.

The torque with rough walls increased by 6.6% on average due to the additional friction on the rotating walls of the impeller in the sidewall gaps. The head decreases from 7% to 10% in the range of flow rate measured, 70% to 130% of the design flow rate. The head

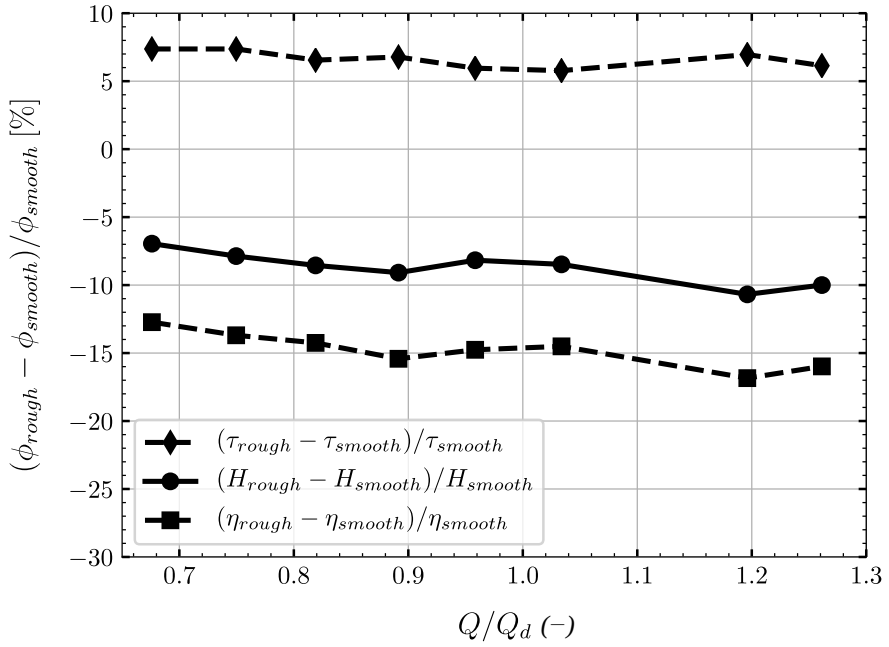

Figure 3.6: Influence of the roughness on the measured hydraulic characteristics. Adapted from [16].

losses increases with the flow rate. The efficiency follows the same trend as the head, with a decrease above 15% lower past the design point. These results show the important effect of roughness at low specific speed ($n_s = 44$ here), and that the importance of roughness estimation is crucial for accurate CFD predictions. It should be noted that the roughness has a stabilizing effect on the head curve, even if this effect is small.

The recommendations of the author to model low specific speed pump by means of CFD are the following:

- Determine the equivalent roughness of differents walls (if not hydraulically smooth).
- Identify sensible areas, i.e. detached flow areas and unformed boundary layer regions. For low specific speed pumps, this applies for leading and trailing edges of the impeller blades, the impeller pressure side, the volute tongue and diffuser, the side wall gaps on hub and shroud sides and the sealing gaps.
- Identify high local errors zones during the convergence process and refine the zones.

The $k-\omega$ SST turbulence model

The $k-\omega$ SST turbulence model is used for all studies performed in this thesis, based on previous studies that successfully predicted pump performances at low specific speed. This turbulence model appeared to solve problems encountered with older turbulence models, namely the $k-\epsilon$ and the $k-\omega$, by blending between the two models. The $k-\epsilon$ turbulence model presents weaknesses in a variety of flow typically present in turbomachinery [1]:

- Flow on curved paths
- Decelerated flows
- 3-dimensional boundary layers

- Rotating components
- Swirling flows
- Strong secondary flows

The production of turbulence kinetic energy is over-predicted in locations with strong velocity gradients (for example near a stagnation point). Therefore, flow separations are not (or insufficiently) recognized which is a major problem in turbomachinery applications. For example, El-Behery [42] presented computations of steady RANS equations to model a simple asymmetric diffuser and compared different turbulence models (Standard $k-\epsilon$, low-Re $k-\epsilon$, Standard $k-\omega$, $k-\omega$ SST, Reynolds Stress Model and $v2-f$ model). See figure 3.7 for a view of the computational domain.

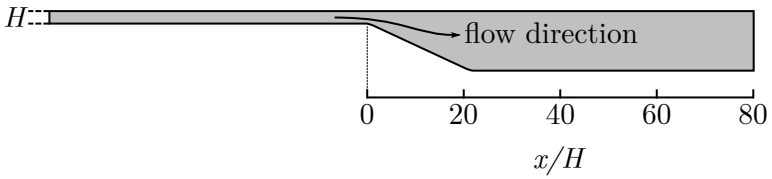

Figure 3.7: Computational domain of asymmetric diffuser [42].

The case is two-dimensional. Three grids were created to vary the first cell height. The average y^+ of the coarse, medium and fine grids are 30, 15 and 1. The number of cells in the flow direction is not changed. The separation and reattachment points are compared to experimental results. Both $k-\epsilon$ based models did not predict any flow separation, regardless of the grid. Other models well captured the flow separation and reattachment points. Notably, the results barely changed with the grids.

The $k-\omega$ turbulence model is believed to be dependant on the freestream turbulence conditions. See for example Kok [43], who suggested that the model empirical coefficients are not tuned correctly.

The $k-\omega$ SST turbulence model attempts to address both weaknesses and gives a better flow prediction close and away from the wall. The transport equations for k and ω are shown in equation 3.8 and 3.9 respectively.

$$\frac{\partial(\rho k)}{\partial t}+\frac{(\rho\bar{v_j}k)}{\partial x_j}=\frac{\partial}{\partial x_j}\left(\left(\mu+\frac{\mu_t}{\sigma_{k3}}\right)\frac{\partial k}{\partial x_j}\right)+P_k-\rho k\omega\beta^*+P_{kb} \tag{3.8}$$

$$\frac{\partial(\rho\omega)}{\partial t}+\frac{\partial(\rho\bar{v_j}\omega)}{\partial x_j}=\frac{\partial}{\partial x_j}\left(\left(\mu+\frac{\mu_t}{\sigma_{\omega3}}\right)\frac{\partial\omega}{\partial x_j}\right)+(1-F_1)\cdot\frac{2\rho}{\sigma_{\omega2}\omega}\frac{\partial k}{\partial x_j}\frac{\partial\omega}{\partial x_j}+\alpha_3\frac{\omega}{k}P_k-\beta_3\rho\omega^2+P_{wb} \tag{3.9}$$

In the ω transport equation 3.9, F_1 is a blending function. If $F_1=0$, the model is equivalent to $k-\epsilon$. If $F_1=1$, the model is equivalent to $k-\omega$. Essentially, near the wall F_1 takes a value of 1 and a value of 0 away from the wall. The function F_1 is given in equation 3.10 and seen in figure 3.8. `tanh` is used so that the transition between the two

models is smooth. The function F_1 is also used to blend between the empirical constants used in each model, e.g. C_μ for the $k-\epsilon$ model and β^* for the $k-\omega$ model.

$$F_1 = tanh(arg_1^4) \tag{3.10}$$

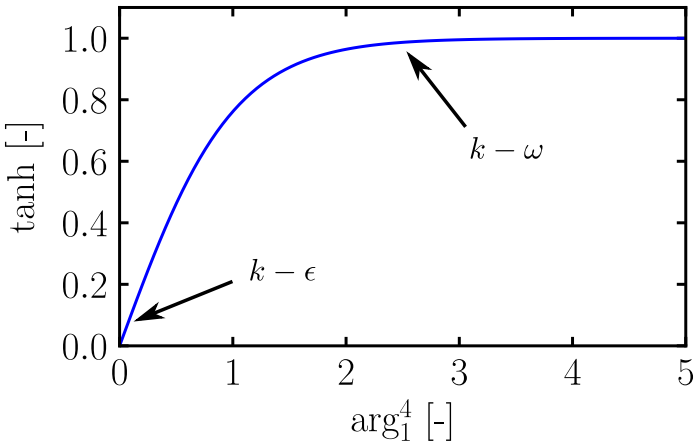

Figure 3.8: Function F_1 as a function of arg_1^4. Reproduced with permission from [37]

The function arg_1 is inversely proportional to the distance between the wall and the cells, so that close to the wall arg_1 takes large values and the $k-\omega$ is used as per figure 3.8.

The use of the function F_1 gives the $k-\omega$ BST model. The $k-\omega$ SST model introduces a viscosity limiter, see equation 3.11, with the the term SF_2 in the denominator. This limiter results in a better agreement with experimental measurements of separated flows.

$$\nu_t = \frac{a_1 \rho k}{max(a_1\omega, SF_2)} \tag{3.11}$$

The function F_2 is another blending function similar to F_1, dependant on the distance to the closest wall. F_2 takes larger values close to the wall, which if too large, limits the viscosity (it is reduced). The viscosity limiter is the primary reason behind the $k-\omega$ SST better agreement with experiments of separated flows.

3.1.3. CFD specifications

The work of the thesis is composed of several studies. Each study has similar CFD specifications and these will be presented here. The specific details of each study are presented along their results.

Domain decomposition

The pump is decomposed into several numerical domains. The suction pipe, the impeller, the sidewall gap on the hub side, the sidewall gap on the shroud side, the volute and the discharge pipe. The impeller may be also decomposed into a stationary part and a rotating part starting right before the leading edge. Figure 3.9 represents the typical domain decomposition used in the different studies.

The insertion of the sidewall gaps in pump computations is more and more widespread, however it still happens to see the gaps not included in CFD computations. The gaps

Figure 3.9: Decomposition of the pump into numerical domains.

are included here because of their importance and impact on the main flow field. Several reasons justify the importance of introducing the gaps in CFD computations. In fact, their inclusion is necessary at low n_s. First the low volumetric efficiency mentioned in section Volumetric efficiency, which directly implies that a large portion of the mean flow of low specific speed pumps circulates back to the suction via the gaps, and thus also influences the flow inside the impeller, especially at low flow rate. Secondly the importance of disk friction with decreasing specific speed is exponentially important as seen in section Disk friction. Analytical or empirical formulas fail to predict the disk friction losses, further strengthening the need of the sidewall gaps inclusion. Finally, the interaction between the volute and the gaps is also important, especially close to the tongue. Juckelandt [16] schematically represented the flow on the sidewall gap of a pump of a specific speed $n_s = 44$ at design point, see figure 3.10. The interaction between the impeller and volute flows is depicted. From 0 to 90° there is an important flow from the volute towards the gap due to the impeller blades passing at the tongue. From 90 to 270°, light exchanges are observed and the main flow from the gap towards the volute occurs in the last section. This representation allows us to understand the complexity of the flow in the gap and its circumferential heterogeneity, hence the need to include the gaps in the numerical model.

The inlet surface is placed at a distance $L/D = 6$ from the impeller inlet relative to the suction pipe diameter and the outlet is placed at a distance $L/D = 13$ from the volute outlet relative to the discharge pipe diameter.

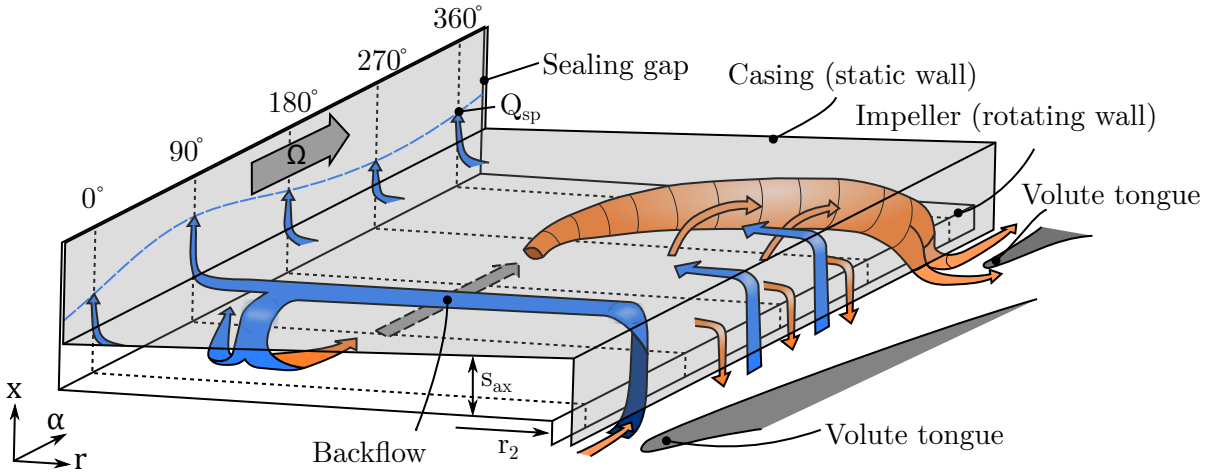

Figure 3.10: Schematic representation of the flow in the sidewall gap (shroud side) at the design point [16].

Numerical grids

The creation of the numerical grid, or mesh, is arguably the most time consuming task of the CFD engineer. Each domain is discretized into small cells in which the Finite Volume Method is applied to describe the flow physics. Although a cell can be a polyhedron with large number of faces, the most common encountered elements are tetrahedrons, prisms and hexahedrons, figure 3.11.

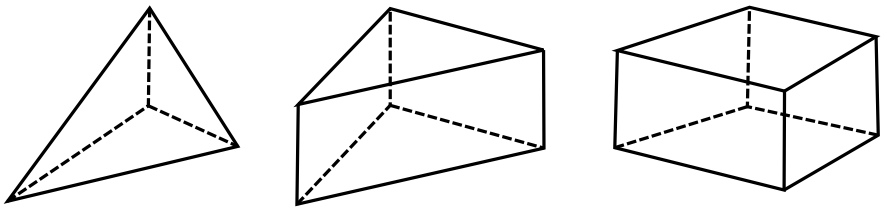

Figure 3.11: Most common cell types in CFD.

Hexahedron type of cell has a numerical advantage in term of computational convergence over unstructured meshes using primarily tetrahedral cells. The generation of structured meshes for complex geometries used in turbomachinery can be time consuming and does not always lead to high quality meshes. In this thesis, two preprocessors are used for mesh generation, all part of the commercial software `ANSYS`. `ANSYS-TurboGrid` is used to generate part of the impeller grids computed in this thesis. This software offers a fast generation of stuctured meshes for minimal user input and is specialised for turbomachinery components. However the user has a limited control of the mesh. `ANSYS-ICEM CFD` is the main preprocessor used in this thesis. This preprocessor can generate structured and unstructured meshes. It was used only for its stuctured mesh generation capabilities. The process of mesh generation is the decomposition of the domain into hexahedral blocks which have faces, edges and vertices later associated with the surfaces, curves and points of the geometry of interest. This is especially a tedious task, but the advantage is a great control of the mesh in term of cell count, quality and expansion ratio. A view of the blocking used for a periodic impeller generation is seen in figure 3.12.

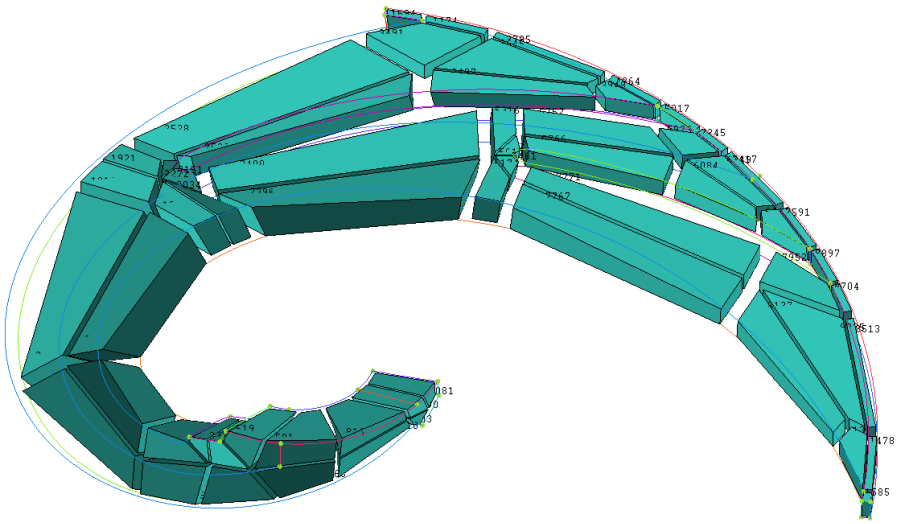

Figure 3.12: Example of blocking structure used for impeller generation (ICEM-CFD).

The mesh quality requirements for a FVM solver are similar but can have specificities. The CFX-Solver Guide [44] suggests three important measures and their limits consisting of an acceptable mesh for the solver.

Non-orthogonality is the main metric that affects the stability of a CFD solution. Figure 3.13 illustrates the principle of non-orthogonality. Unless the two cells are perfect quadrilaterals, the unit normal vector n_f and the centroid-to-centroid vector d_{PN} will not be parallel to each other. The angle between these two vectors is the face non-orthogonality. The maximal allowable value for mesh non-orthogonality angle is below 80°. Below 70° is preferred. A perfect mesh has a non-orthogonality angle of 0°.

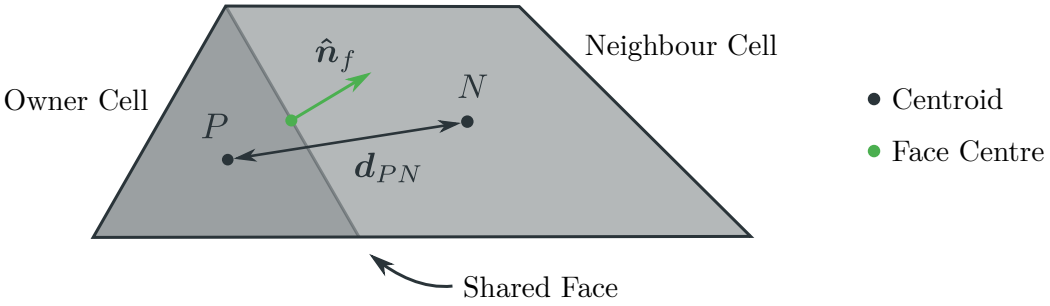

Figure 3.13: Representation of non-orthogonality between 2 adjacent cells. Reproduced with permission from [37].

The mesh expansion factor is a metric measuring the ratio of volumes between two adjacent cells. The maximum accepted value is 20.

The mesh aspect ratio is a metric measuring the ratio of the longest side of a cell to its shortest side. The maximum aspect ratio recommended is below 1000.

Once the mesh quality is sufficient, a grid convergence analysis is performed. The objective of this type of study is ensuring that the results obtained are independent of the grid while using the least possible cell count for an efficient study. This type of analysis is performed at the beginning of each study as the geometries slightly differ for each case.

Boundary conditions & interfaces

The boundary conditions are standard for turbomachinery application. Mass flow is used at the inlet of the pump and average static pressure at the outlet. The impeller is a rotating domain. The interface between static domain is treated with the General Grid Interface (GGI). The interface between stationary and rotating domains depends on the treatment used:

- For studying transient effects, the Transient-Rotor Stator interface is used which allows a rotation of the impeller grid.
- For obtaining initial results for transient simulation, the Frozen Rotor interface is used. In simple terms, this method corresponds to a snapshot of the flow at a given angular position of the impeller.
- For a study of steady performances, the Mixing-Plane interface is selected. This interface averages the variables in a circumferential direction to suppress the interaction between the impeller and the other components.

For transient simulations, the timestep used is $1.72 \cdot 10^{-4}$ s. It corresponds to an impeller grid rotation of 1.5° at 1450 RPM. A sensitivity study of this parameter has not been performed but rather directly taken from literature where it is common to see impeller grids rotated by 0.5° to 3° per timestep depending on the studies.

The accuracy of the solution also largely depends on how the physical quantities vary between cell faces. They can be first order (the physical quantities are constant within a cell), second order (the physical quantities vary linearly) or third order (the physical quantities are quadratic functions within a cell). The influence of the order used in the predicition performances of an industrial pump are seen in figure 3.14. Clearly, calculations with first order truncation errors are not sufficiently accurate for turbomachinery applications. Second order schemes are selected for the computations in this thesis. The option for advection scheme and turbulence numerics used in CFX is set to `High Resolution`. In case of transient simulation, the transient scheme selected is `Second Order Backward Euler`.

To ensure that the simulation is properly converged, the residuals RMS are set to 10^{-5} for both steady and transient simulations. In case of transient simulations, they are run until a cyclic behaviour is observed, which usually corresponds to 7 rotations of the impeller.

Finally the curvature correction option is set. One weakness of the eddy-viscosity models is that these models are insensitive to streamline curvature and system rotation. Based on the work of Spalart and Shur [45] a modification of the production term has been derived to sensitize the standard two-equation models to these effects. More information can be found in the CFX-Solver Guide [44].

3.2. Experimental approach

Part of the results presented in this dissertation are verified experimentally. The results correspond to Study 2: Effect of the addition of 1 and 2 splitters per impeller passage. However it is believed that due to the similarity of pump design and CFD setup in all

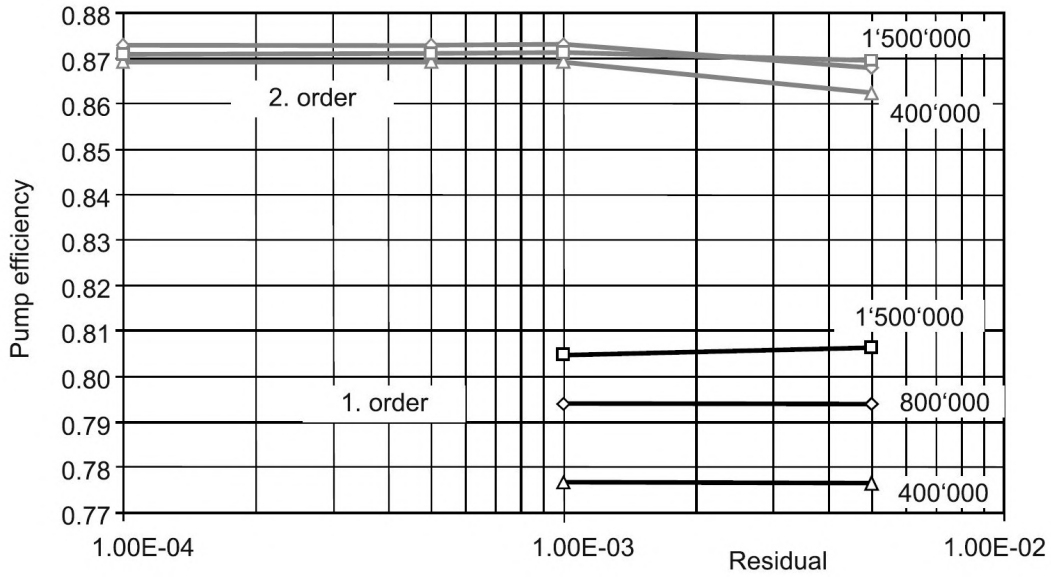

Figure 3.14: Influence of grid resolution and order on the calculated efficiency [1].

studies, the validation presented can also be conclusive for all studies presented in this thesis.

The laboratory of the Viktor Kaplan department of fluid engineering is equipped with a pump test bench than can accommodate for a large number of pumps or turbines. A schematic diagram of the test rig can be seen in Figure 3.15 and a partial view of the physical test bench in operation in Figure 3.16.

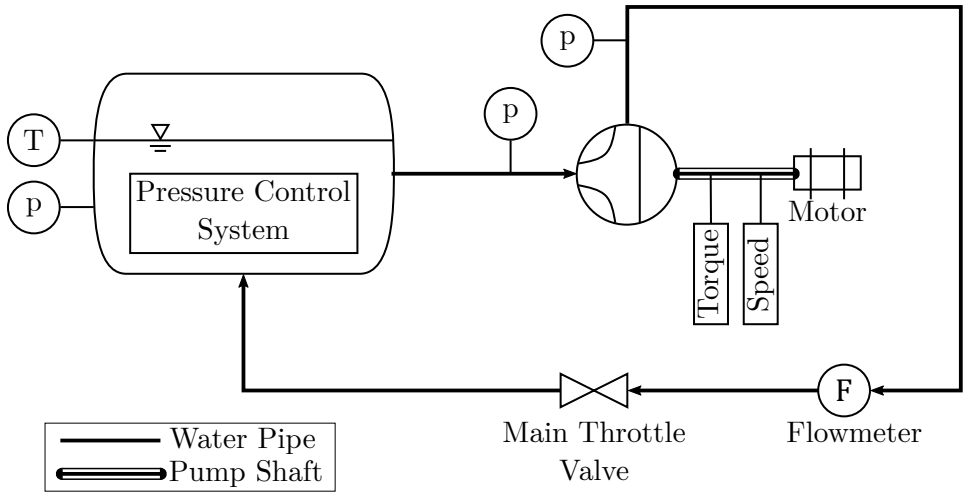

Figure 3.15: Schematic diagram of the test rig.

For cost reduction, the tested pump has been adapted to an existing motor present in the laboratory. The motor used is part of the pump BETA12, and a new volute and impeller were manufactured to fit into its base.

3.2.1. Components manufacturing

A volute casing, three impellers and other components were manufactured. The volute casing is made from 2 blocks of Aluminium 5754, a material with a good corrosion re-

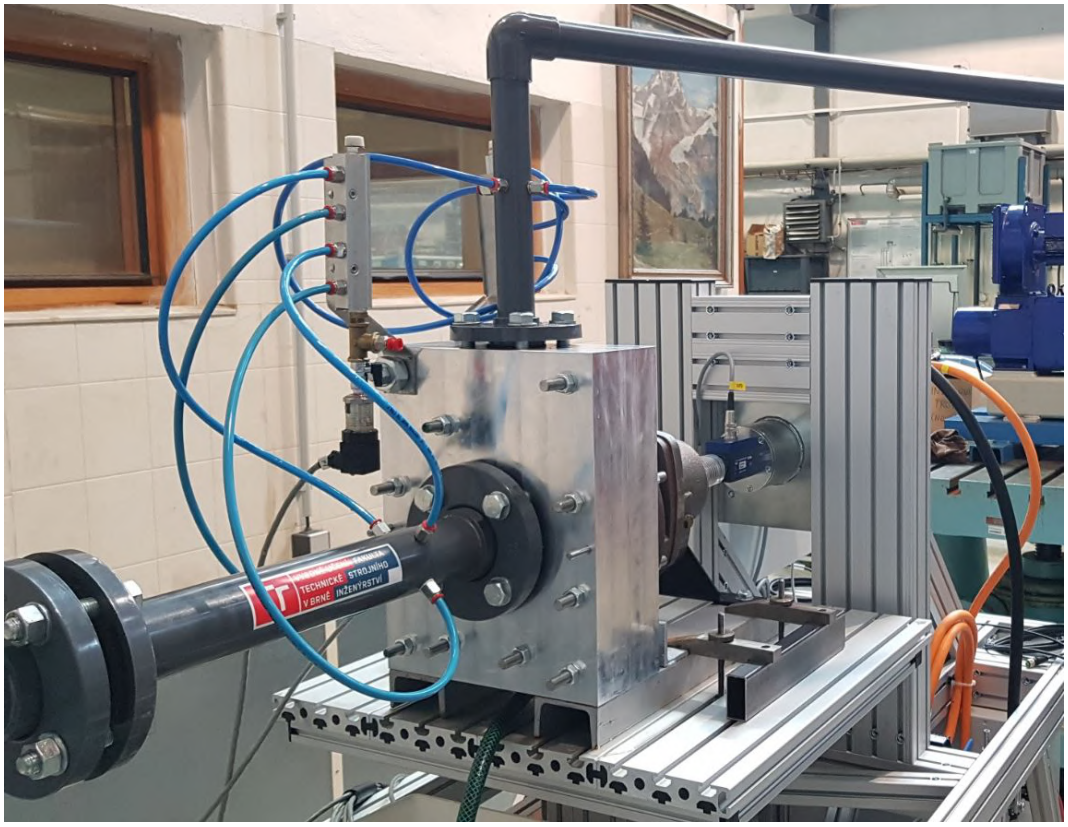

Figure 3.16: Partial view of the test rig.

sistance. The centering of the two parts of the casing is done thanks to two tapper pins M8. Both parts were CNC-machined to ensure smooth surface finishing, essential for the volute component at low specific speed as seen in section Volute losses. A sealing ring made of hard PVC has been pressed into the casing at the inlet section. Half of the casing (hub side) is seen in figure 3.17.

The impellers are 3D printed using the Fused Deposition Modeling (FDM) technology with Nylon 12 as a single part. This method and material were used for a pump with comparable specific speed with higher performances by Olimstad [46]. The impellers were then post-processed at the faculty with a manual lathe to make space for the shaft sleeve and accurately dimension the sealing gap. However, the 3D printing of the impeller revealed to be a complex process. Each impeller was printed as a single piece with supports from the material SR 110 from Stratasys, later dissolved with a liquid principally containing sodium hydroxide. To print the impeller in a single piece, supports had to be printed inside the impeller channels.

The experiments on the three impellers were done in several phases and in the first phase, a single impeller was prepared and tested. This was to ensure that the 3D printed model was mechanically resistant and able to transfer the pressure to the fluid as it was required. The first preliminary tests failed as the impeller was able to deliver only half the required pressure at the design point. The failure was due to the presence of supports inside the impeller channels invisible to the eye due to the thin flow passage, see figure 3.18.

The time to dissolve the supports has been raised from the usual 48h to more than 150h to make sure all supports were dissolved and out of the channels. The secondary tests, without supports gave satisfactory results and the two other impellers, with additional

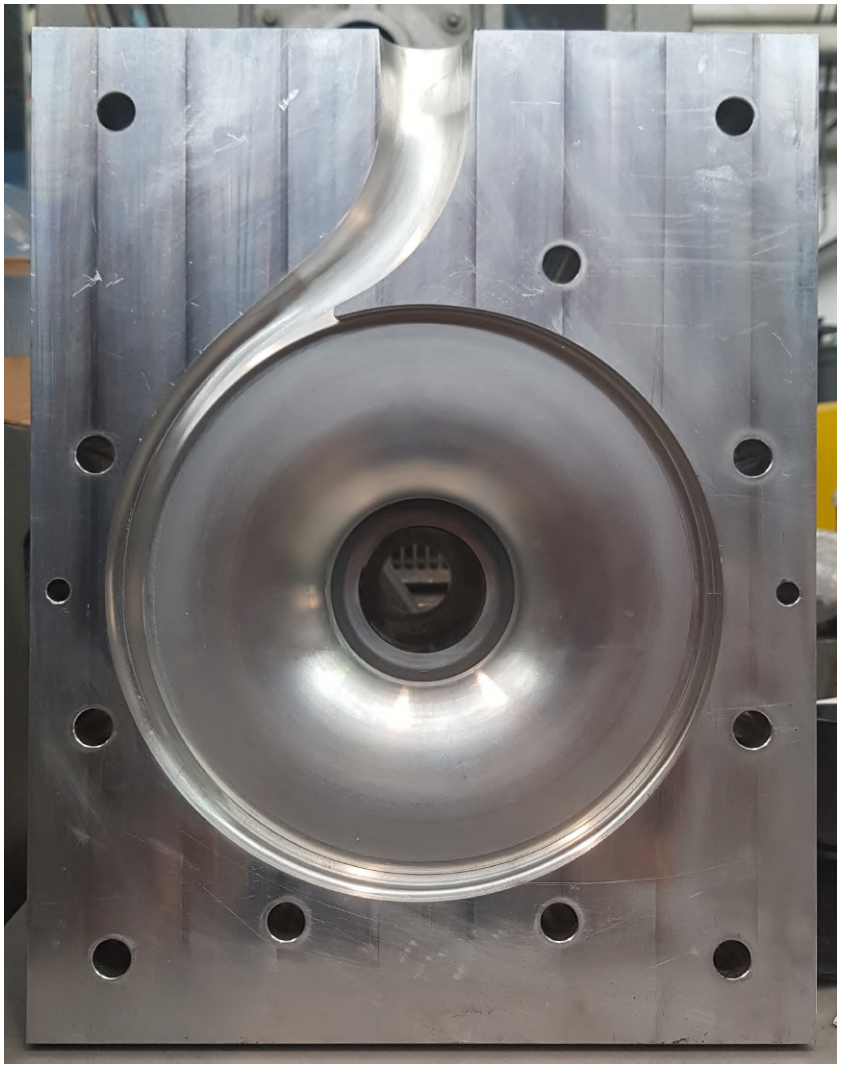

Figure 3.17: Casing (Hub side).

blades in the channel were ordered. A second complication is related to the fact that it was not possible to print the two later impellers with the exact same settings. The first impeller could be printed on a flat surface but the two other had to be printed on an inclided plane to avoid heat deformation, which is a common trouble with the material Nylon 12. As a result, the surface structure of the two later impellers is different, see figure 3.19. But without the supports inside the channels, both tests were successful on the first try.

Other parts, such as the shaft sleeves, the shaft nut and the seal ring were made at the faculty with the use of both manual and CNC lathe. Table 3.1 lists all manufactured components, their material, method of fabrication and provider.

3.2.2. Measurement and uncertainty

The parameters of interest are the head, the efficiency, the torque and the flowrate. These parameters are measured experimentally. The instrumentation used is described below:

- Inductive flowmeter DN80/PN16, ELA, spol. s r.o. Measuring range $0 - 60\ l/s$. Current output $0 - 20\ mA$. Measurement uncertainty $\pm 0.3\%$ of the measured value.

Figure 3.18: Impeller 3D printing supports inside channels due to insufficient time in the solution of sodium hydroxide.

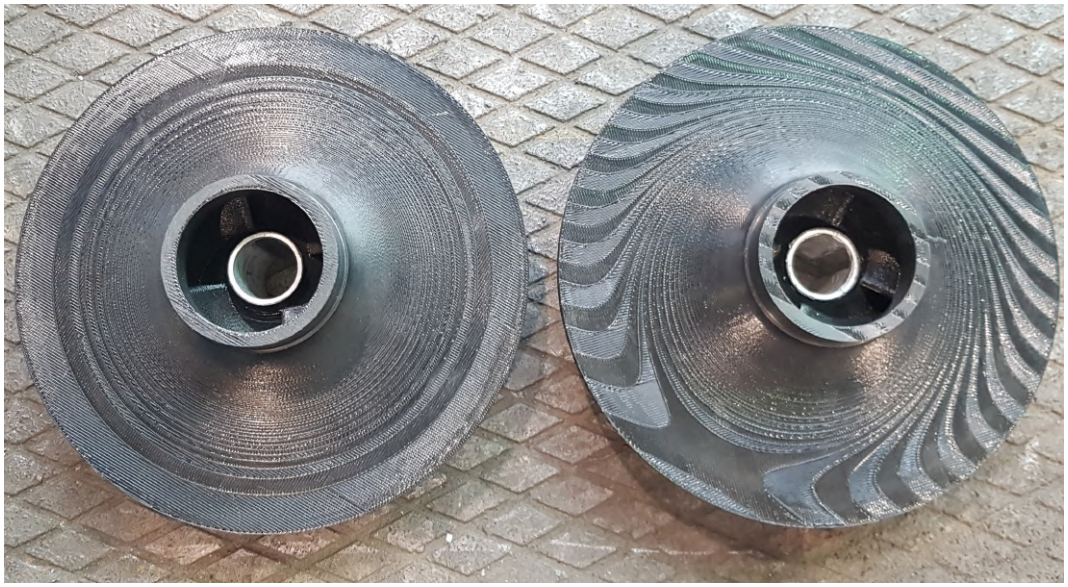

Figure 3.19: Impeller surfaces difference for Case 0sp (left) and Case 1sp (right). Case 2sp has the same surface finish as Case 1sp.

- Torque transducer T21WN, Hottinger Brüel Kjaer GmbH. Measuring range $0.1-20$ Nm. Measurement uncertainty $\pm 0.2\%$ of the measured value.
- Torque transducer T21WN, Hottinger Brüel Kjaer GmbH. Measuring range $0-20000$ RPM. Measurement uncertainty $\pm 0.2\%$ of the measured value.

Table 3.1: List of manufactured components.

Component	Material	Method	Provider
Casing (part 1)	Aluminium 5754	CNC	OMOS, s.r.o.
Casing (part 2)	Aluminium 5754	CNC	OMOS, s.r.o.
Impeller 1	Nylon 12	FDM	MCAE Systems, s.r.o.
Impeller 2	Nylon 12	FDM	MCAE Systems, s.r.o.
Impeller 3	Nylon 12	FDM	MCAE Systems, s.r.o.
Shaft sleeve (x3)	Aluminium	CNC	internal
Shaft nut	Aluminium	CNC	internal
Ring Seal	Hard PVC	Lathe	internal

- Pressure transducer DMP 331, BD SENSORS, Ltd. Measuring range $0 - 1.6$ *bar* (inlet sensor) and $0 - 4$ *bar* (outlet). Measurement uncertainty $\pm 0.35\%$ of the measured value.

The measurement of the rotational speed is included in the torque transducer. For a parameter ϕ, the absolute uncertainty is given by the parameter u_ϕ. The relative uncertainty is given by u_ϕ/ϕ and is expressed in percent. The uncertainty calculation for each parameter is presented in the following sections.

Flowrate

The flowrate is directly recorded from the flowmeter. The absolute measurement uncertainty is given by equation 3.12.

$$u_Q = 0.003Q \tag{3.12}$$

with Q $[l/s]$ the measured value.

Torque

The torque is directly recorded from the torque transducer. The absolute measurement uncertainty is given by equation 3.13.

$$u_{M_k} = 0.002M_k \tag{3.13}$$

with M_k $[Nm]$ the measured value.

Rotor speed

The rotor speed is directly recorded from the torque transducer. The absolute measurement uncertainty is given by equation 3.14.

$$u_N = 0.002N \tag{3.14}$$

with N $[RPM]$ the measured value.

Pressure

The pressure is directly recorded from the pressure transducer. The absolute measurement uncertainty is given by equation 3.15.

$$u_p = 0.0035p \tag{3.15}$$

with p $[Pa]$ the measured value.

In pump measurements, it is often the pressure difference between two probes that is of interest. In that case, the uncertainty would be given by equation 3.16.

$$u_{\Delta p} = 0.007\Delta p \tag{3.16}$$

Head

The formula applied to calculate the head is presented in equation 3.17.

$$H = \frac{p_2 - p_1}{\rho g} + \frac{v_2^2 - v_1^2}{2g} + h_2 - h_1 \tag{3.17}$$

with p_2 $[Pa]$ the pressure at the pump outlet, p_1 $[Pa]$ the pressure at the pump inlet, v_2 $[m/s]$ the fluid velocity at the pump outlet and v_1 $[m/s]$ the fluid velocity at the pump inlet. $h_2 - h_1$ $[m]$ represents the static pressure difference between the two pressure sensors. The static pressure (p_{2s} at the outlet, p_{1s} at the inlet) is measured directly from the pressure probes in a flooded system. Because the flowrate is measured and not the velocity, the formula for the head measurement applied is (equation 3.18) :

$$H = \frac{p_2 - p_1}{\rho g} + \frac{8Q^2}{g\pi^2}\left(\frac{1}{d_1^4} - \frac{1}{d_2^4}\right) + \frac{p_{2s} - p_{1s}}{\rho g} \tag{3.18}$$

with d_1 (m) the suction pipe diameter and d_2 (m) the discharge pipe diameter. The uncertainty calculation is given by equation 3.19.

$$\begin{aligned} u_H &= \sqrt{\left(\frac{\partial H}{\partial \Delta p} \cdot u_{\Delta p}\right)^2 + \left(\frac{\partial H}{\partial Q} \cdot u_Q\right)^2 + \left(\frac{\partial H}{\partial \Delta p_s} \cdot u_{\Delta p_s}\right)^2} \\ &= \sqrt{\left(\frac{1}{\rho g} \cdot u_{\Delta p}\right)^2 + \left(\frac{16Q}{g\pi^2}\left(\frac{1}{d_1^4} - \frac{1}{d_2^4}\right) \cdot u_Q\right)^2 + \left(\frac{1}{\rho g} \cdot u_{\Delta p_s}\right)^2} \end{aligned} \tag{3.19}$$

Efficiency

The formula applied to calculate the efficiency is presented in equation 3.20.

$$\eta = \frac{\rho g H Q}{(M_k - M_{k,static})N \cdot \pi/30} \tag{3.20}$$

Since the quantity of interest is the hydraulic efficiency, the static torque is subtracted from the measured torque. The static torque is measured by flooding the pump and rotating the shaft (without impeller). The static torque includes the resistance torque from the seals and bearings. The uncertainty calculation is given by equation 3.21.

$$u_\eta = \left(\left(\frac{\partial \eta}{\partial M_k} \cdot u_{M_k} \right)^2 + \left(\frac{\partial \eta}{\partial M_{k,static}} \cdot u_{M_{k,static}} \right)^2 + \left(\frac{\partial \eta}{\partial Q} \cdot u_Q \right)^2 + \left(\frac{\partial \eta}{\partial H} \cdot u_H \right)^2 + \left(\frac{\partial \eta}{\partial N} \cdot u_N \right)^2 \right)^{1/2} \quad (3.21)$$

Each term of equation 3.21 is expanded below.

$$\begin{aligned}
\frac{\partial \eta}{\partial M_k} \cdot u_{M_k} &= -\frac{\rho g H Q}{(M_k - M_{k,static})^2 N \cdot \pi/30} \cdot u_{M_k} \\
\frac{\partial \eta}{\partial M_{k,static}} \cdot u_{M_{k,static}} &= \frac{\rho g H Q}{(M_k - M_{k,static})^2 N \cdot \pi/30} \cdot u_{M_{k,static}} \\
\frac{\partial \eta}{\partial Q} \cdot u_Q &= \frac{\rho g H}{(M_k - M_{k,static}) N \cdot \pi/30} \cdot u_Q \\
\frac{\partial \eta}{\partial H} \cdot u_H &= \frac{\rho g Q}{(M_k - M_{k,static}) N \cdot \pi/30} \cdot u_H \\
\frac{\partial \eta}{\partial N} \cdot u_N &= -\frac{\rho g H Q}{(M_k - M_{k,static}) N^2 \cdot \pi/30} \cdot u_N
\end{aligned}$$

Example

An applied example of the uncertainty calculations is presented in this section. It is done for the pump Case 1sp, presented in Study 2: Effect of the addition of 1 and 2 splitters per impeller passage. The uncertainties are calculated for three points: at a low flow rate, close to the design point and at a high flow rate. Table 3.2 presents the three points chosen to illustrate the uncertainty calculation.

Table 3.2: Points chosen to illustrate the calculation of uncertainty.

$Q\ (l/s)$	$M_k\ (Nm)$	$M_{k,static}\ (Nm)$	$H\ (m)$	η
0.34	2.63	0.82	14.31	0.17
1.71	3.76	0.82	13.20	0.50
3.89	5.14	0.82	4.66	0.27

Tables 3.3 and 3.4 present respectively the absolute and relative values of the measured uncertainties. With relative uncertainties below 1% for the parameters of interest, it is assumed that the measurements are accurate enough for the purpose of the study.

Table 3.3: Absolute uncertainties.

$u_Q\ (l/s)$	$u_{M_k}\ (Nm)$	$u_{M_{k,static}}\ (Nm)$	$u_H\ (m)$	u_η
0.0010	0.0053	0.0016	0.0998	0.0015
0.0051	0.0075	0.0016	0.0910	0.0041
0.0117	0.0103	0.0016	0.0272	0.0020

Table 3.4: Relative uncertainties.

u_Q/Q	u_{M_k}/M_k	$u_{M_{k,static}}/M_{k,static}$	u_H/H	u_η/η
0.3%	0.2%	0.2%	0.7%	0.8%
0.3%	0.2%	0.2%	0.7%	0.8%
0.3%	0.2%	0.2%	0.6%	0.7%

3.3. Closure

The methods used for the investigations performed in this thesis are the numerical simulations of flows and experiments to validate the results. The first part of the chapter focuses on the description of the numerical tools used, after a careful review of the specifics of the simulation of low specific speed pumps. The software and CFD specifications (domain decomposition, numerical grids, boundary conditions, ...) are presented. In a second part, the experimental apparatus and instrumentation used is described. The uncertainty calculations are detailed for each parameter of interest with an example on actual measured values.

The details and results of the studies performed using the presented tools are exposed in the next chapters.

4. Results: Splitter blade study

This chapter presents the influence of splitter blades on a low specific speed pump. Therefore, it is focused on the impeller design, and is divided into two sections:

- Study 1: Effect of a single splitter variation
- Study 2: Effect of the addition of 1 and 2 splitters per impeller passage

The first section presents the design of the impeller used in all studies, followed by the numerical analysis of several splitter blades position. The volute casing used in this section is from the BETA14 pump, see Klas [6]. The second study is focused on the influence of the addition of a second splitter per impeller passage. The volute casing used is re-designed to be smaller, providing a closer fit between the pump design point and its best efficiency point. The pump used in this second study is also scaled down by a factor 1/1.6 and experimental results are presented.

4.1. Study 1: Effect of a single splitter variation

The objective of this study is the analysis of the influence of a splitter blade position in the passage of a given impeller design. The effect on the main parameters (head, efficiency and head stability) are of interest.

4.1.1. Impeller design

The original pump used as a base for the thesis is the BETA14 pump studied by Klas in references [5, 6]. The impeller used by Klas was non-conventional and used thick trailing edges, see figure 2.23. For this study, the casing geometry used is the BETA14 pump casing. The thick-trailing edges impeller is a very special design, and this study aims to use classic impeller geometries. The impeller is thus redesigned with an in-house code based based on quasi-potential flow theory. The main dimensions of the impeller are similar (inner and outlet diameter, shape of meridional section), but the outlet width has been reduced from 10 to 6 mm. The number of main blades used is set to 4, per recommendations from Yuan [32] when using splitter blades. The outlet blade angle of the main blades is chosen to be 25 degrees. This is a small value for low specific speed pumps which tends to have high values of outlet blade angles, but it is recommended to avoid Q-H curve instabilities.

After the geometrical constraints and main parameters are fixed, the theory of the compound lamellar flow (CLF), also called quasi-potential flow approach is used for the blade construction. This theory has been implemented in a in-house code. This code was used to design the impeller. Pochylý and Stejskal developed both the theory and the code. The theory is fully presented in references [47, 48] and partially presented here. The CLF is derived to be a compromise between potential flow (low velocity near the hub, thus very small blade inlet angle resulting into low suction ability) and Francis method (assumption of constant velocity profile, thus far from the reality). Using the CFL approach (quasi-potential method), the meridional flow is set to be more or less close to one of these methods. This choice enables to influence the progression of the blade angle

β which is one of the key factors influencing the performance of the runner [1, 49]. Using the curvilinear coordinates, it is possible to easily construct curves and surfaces in the space. The Bezier surface described by equation 4.1 is geometrically very flexible and a mathematically convenient tool.

$$A_{II} = b_2 \left(\pi d_2 sin(\beta_2) - Z \cdot s_2\right) \mathbf{x}(u^1, u^2) = \sum_{i=0}^{n} \sum_{j=0}^{m} \mathbf{b}_{i,j} B_i^n(u^1) B_j^m(u^2) \tag{4.1}$$

The curvilinear coordinates u^1, u^2 are chosen so that coordinate curves create orthogonal grid. The third coordinate represents the wrap angle $u^3 = \phi$. In such case the tangential vectors g_i, depicted in figure 4.1, are perpendicular to each other.

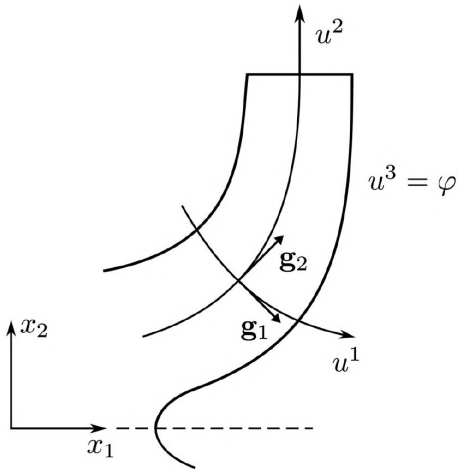

Figure 4.1: Orthogonal curvilinear coordinates in the meridional cross section [47].

The shape of curve, respectively surface, is determined by choosing polygon's points $\mathbf{b}_{i,j}$ to determine the orthogonal grid. The direction of u^2 corresponds to streamline of meridional velocity. Under this assumption, the Euler turbomachinery equation is modified and the formulas for specific energy $Y = gH$ derived in form of equations 4.2-4.3, where $F \equiv c_m g_2$, $\alpha = \frac{g_1 r}{g_2}$, $\gamma = \frac{g_1 g_2}{r\Omega}$ and λ is the vorticity contribution ($\lambda = 0$ for potential flow, otherwise the flow is rotational). More details on the theory might be found in [47, 48].

$$\frac{1}{\sqrt{g}} \frac{\partial F}{\partial u^1} = \frac{\lambda}{r^2} \left(\frac{Y}{\Omega} - \Omega r^2 \right) \tag{4.2}$$

$$\frac{\partial}{\partial u^2}(\alpha F) + \gamma \frac{\partial Y}{\partial u^3} = 0 \tag{4.3}$$

For the basic blade design, it is necessary to consider the flow without spiral vortices. This assumption is fulfilled by special form of rotational flow, so called quasi-potential flow, according to condition $rot(\mathbf{v}) \cdot \mathbf{v} = 0$. The function $\mathbf{v} = \kappa grad(\Phi)$ satisfies the previous condition. The meridional flow is calculated considering equation 4.3 and flow kinematics must fulfill the continuity equation which is interpreted in curvilinear coordinates by equation 4.4.

$$\frac{g_1(u^1,1) r(u^1,1) g_2(u^1,u^2)}{g_1(u^1,u^2) r(u^1,u^2)} c_{m2} = \frac{\kappa(u^1,u^2) Q}{2\pi \int_0^1 \frac{\kappa(u^1,u^2) g_1(u^1,u^2)}{g_2(u^1,u^2)} r(u^1,u^2) du^1} \tag{4.4}$$

Based on the value of κ, it is possible to obtain different velocity profiles of meridional velocity, for example:

- Francis method $\mathbf{c_m} = A(u^2)$, $\kappa(u^1, u^2) = g_2$
- Irrotational flow $rot(\mathbf{c_m}) = 0$, $\kappa(u^1, u^2) = 1$
- Rotational flow (CLF) $rot(\frac{1}{\kappa}\mathbf{c_m}) = 0$, $\kappa(u^1, u^2) = g_2^n$, where $n \in [0, 1]$

The meridional profile is built using Bezier surface controlling the evolution of flow cross-section. The blue points are control points of Bezier surface, see figure 4.2. The meridional shape is interactively modeled by the movements of control points.

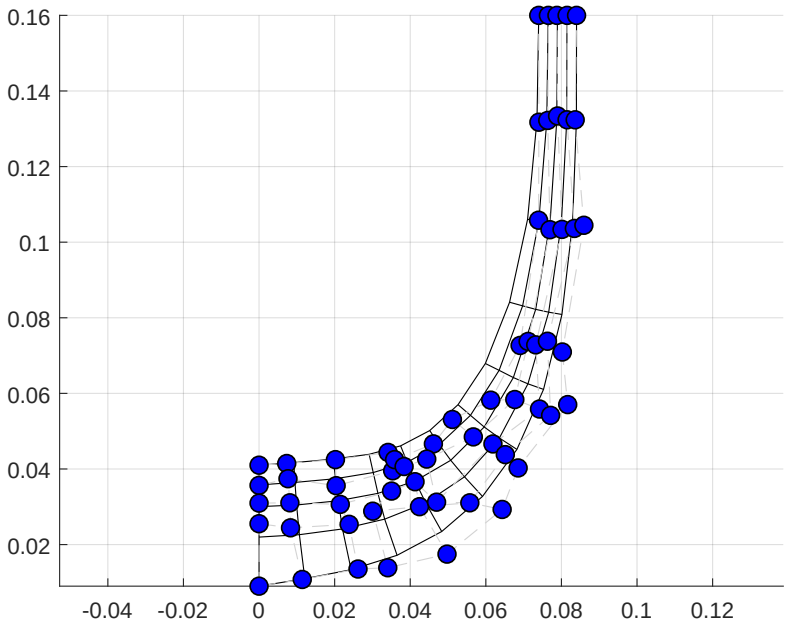

Figure 4.2: Meridian as a Bezier surface with control points.

In next step the meridional velocity is calculated for the input parameters, as shown in figure 4.3.

The output of the described in-house code is a file readable by the parametric impeller design software `Ansys-BladeGen`, which outputs the fluid and solid zones of the impeller. The constructed impeller is then slightly optimized using `Ansys-BladeGen` and preliminary CFD calculations, especially to align the leading edge with the flow. The main pump parameters can be seen in Table 4.1.

4.1.2. Splitter blade configuration

The splitter blades are constructed in the software `ANSYS-BladeGen`. The splitter design is based on the main blades' design and is modified according to three parameters. The parameters are presented in the state-of-the-art section Splitter blades and re-explained here, based on figure 4.4.

- The parameter a sets the position of the leading edge of the splitter d_{sp}, hence it directly controls the splitter blades' length, see equation 2.11.

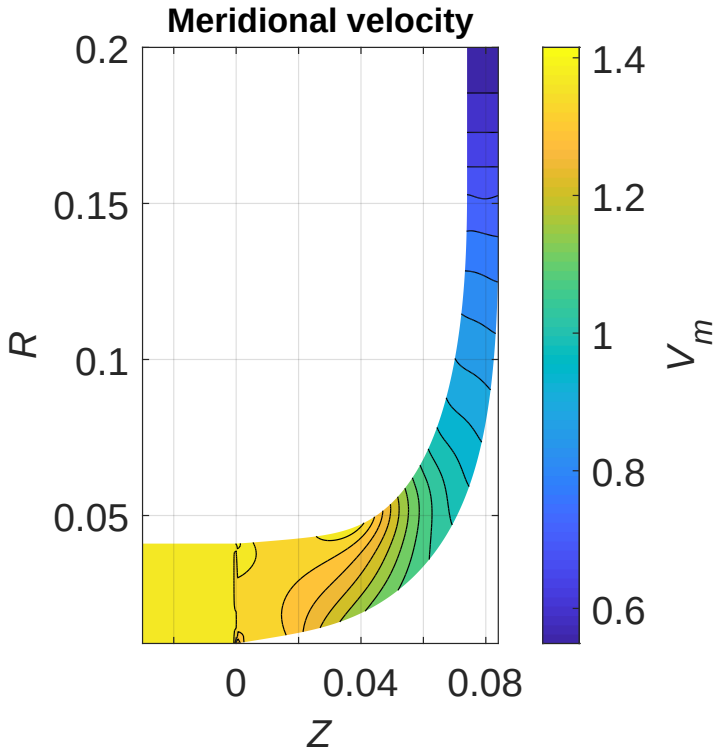

Figure 4.3: Contours of meridional velocity.

Table 4.1: Pump parameters (Study 1).

Designation	**Symbol**	**Value**	**Units**
Rotor speed	N	1450	RPM
Design head	H_d	32	m
Design flow rate	Q_d	0.0069	$\mathrm{m^3{\cdot}s^{-1}}$
Specific speed	$n_s = 3.65N\frac{Q_d^{0.5}}{H_d^{0.75}}$	32	-
Impeller outlet diameter	d_2	320	mm
Impeller outlet width	b_2	6	mm
Impeller outlet blade angle	β_{2B}	25	deg
Main Blade number	Z	4	-

- The parameter θ sets the circumferential position of the splitter in the passage, i.e. closer to the suction or pressure side of the main blade.
- The parameter α_{sp} controls the outlet blade angle of the splitter, or rather the blade angle difference between the main blade and the splitter blade so that $\alpha_{sp} = \beta_{2B,splitter} - \beta_{2B,main}$.

The last parameter α_{sp} changes the outlet blade angle, which implies a change in the total blade shape. To illustrate this fact, figure 4.5 represents different values of α_{sp} used and their influence on the blade angle β. To simplify the design and make it easily reproducible, the blade angles are defined by a spline with 3 control points. Control points 1 and 2 are fixed and only the third one, controlling β_{2B} is changed. At $\alpha_{sp} = 0$, the development of the blade angle is the same as the main blade. At $\alpha_{sp} = -5$, the outlet

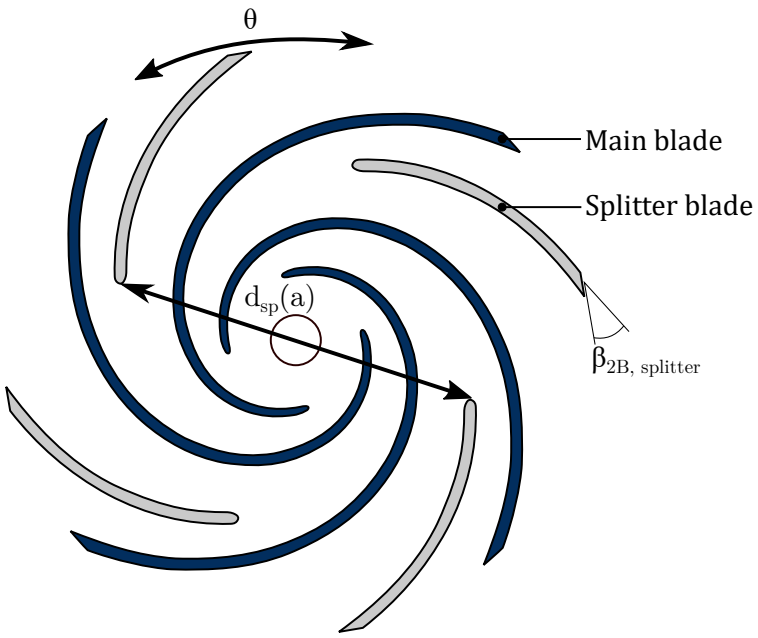

Figure 4.4: Splitter blades parameters.

blade angle is $\beta_{2B,splitter} = 20°$ and at $\alpha_{sp} = 10$, the outlet blade angle is $\beta_{2B,splitter} = 35°$. This change impacts only the blade angles of the splitter and the main blades' definition is strictly the same for all cases.

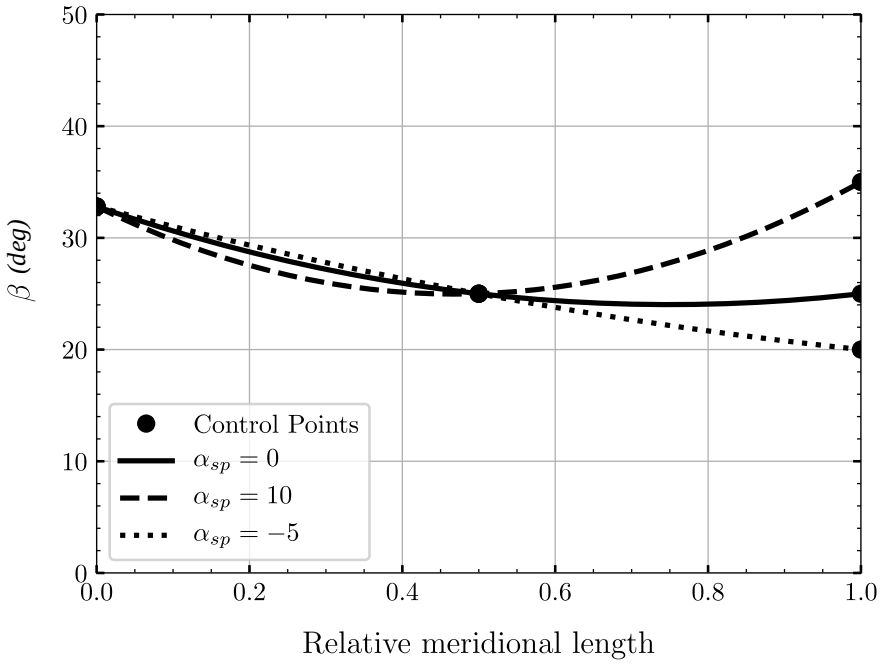

Figure 4.5: Evolution of the tangential blade angle of the splitters over the meridional length for α_{sp} changes.

4.1.3. CFD Setup

To ensure consistency between the different impeller meshes, the software `ANSYS-TurboGrid` is used to generate the different impeller meshes. The mesh of other domains (suction pipe, sidewall gaps, volute and discharge pipe) are all meshed in `ANSYS-ICEM`. Due to the complexity of the volute geometry downstream the tongue, tetrahedral and wedge elements have been used at the transition between the volute and the discharge pipe. Nonetheless, 97% of elements are hexahedral. The wall-treatment chosen for this study is the wall-function approach, despite the extensive explanation presented in the Methods chapter stating that a low-Reynolds number mesh should be used for the simulations of low specific speed pumps. The choice of the wall-treatment is acceptable in that case because the volute throat area of the pump BETA14 is over-designed for the specific speed used, and the choked-flow at the throat area leading to a large turbulence kinetic energy zone downstream the tongue does not appear here. This is confirmed by the results showing that at 160% of the design flow rate, the best efficiency point, largely governed by the volute throat area, is not yet reached. Moreover, a large number of designs are tested with the main focus of the study being the influence of the splitters on the main characteristics and not specific flow details. To ensure the quality of the results, a grid independence study is performed on two parameters, the head and the hydraulic efficiency, see figure 4.6. The final mesh has 8,6 million cells (for Case 1) and an average value of y^+ around 30 at the design flow rate. The mesh can be seen in figure 4.7.

The CFD parameter used for the study are precised in section CFD specifications.

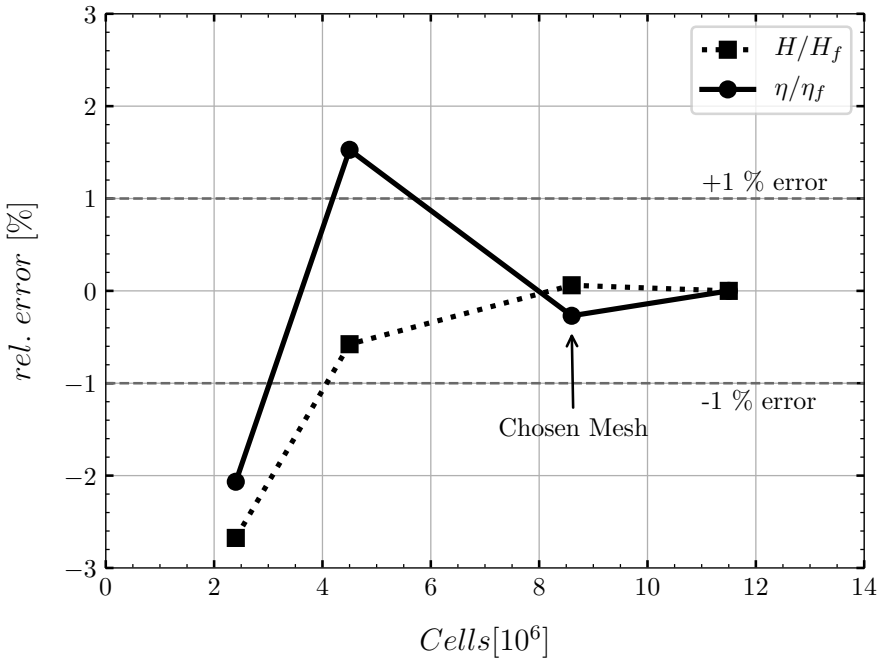

Figure 4.6: Grid independence study. The head and the hydraulic efficiency are evaluated as a function on the number of cells.

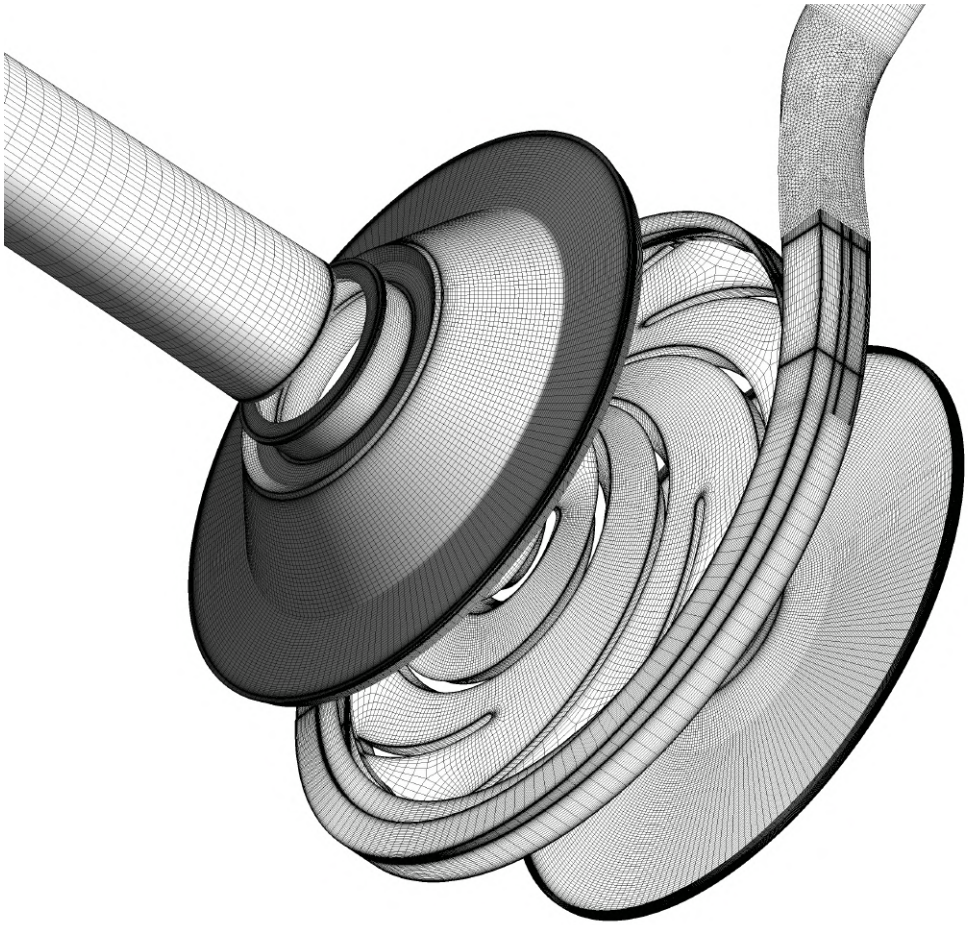

Figure 4.7: View of the grid of all domains for the chosen grid.

4.1.4. Design of Experiments

A design of experiment is performed to evaluate the influence of the different parameters on the head, efficiency and a parameter measuring the torque of the splitter blade (T_{sp}) relatively to the main blade torque (T_{main}) called the relative splitter blade torque ($T_{sp,rel}$).

$$T_{sp,rel} = \frac{T_{sp}}{T_{sp} + T_{main}} \tag{4.5}$$

A full factorial experiment with three parameters and two levels (2^3) is realized, leading to 8 designs tested. The different levels and parameters can be observed in Table 4.2. The parameter a controls the leading edge diameter and results in a splitter blade leading edge placed at 0.54 d_2 for the lower level and 0.77 d_2 for the higher level. The offset pitch fraction θ is set closer to the suction side for the lower level, $\theta = 0.3$, according to recommendations in Yuan [32]. It is compared with the higher level, $\theta = 0.5$, when the splitter is placed in the middle of the main blades. The deflection angle of the splitter blades α_{sp} is set to -5 and 10 degrees for low and high levels respectively, to observe a large difference in outlet blade angles. The 8 cases and results are shown in Table 4.3, and the splitter blades configuration can be seen in figure 4.8. The main blades are black and the splitter blades white.

By looking at Table 4.3, the first obvious conclusion is about the hydraulic efficiency weakly influenced at the designed point by the splitter blades configurations. The max-

Table 4.2: Parameters and levels of the design of experiments.

	Factors	a $(-)$	θ $(^\circ)$	α_{sp} $(^\circ)$
Level	-1	0.4	0.3	-5
	1	0.7	0.5	10

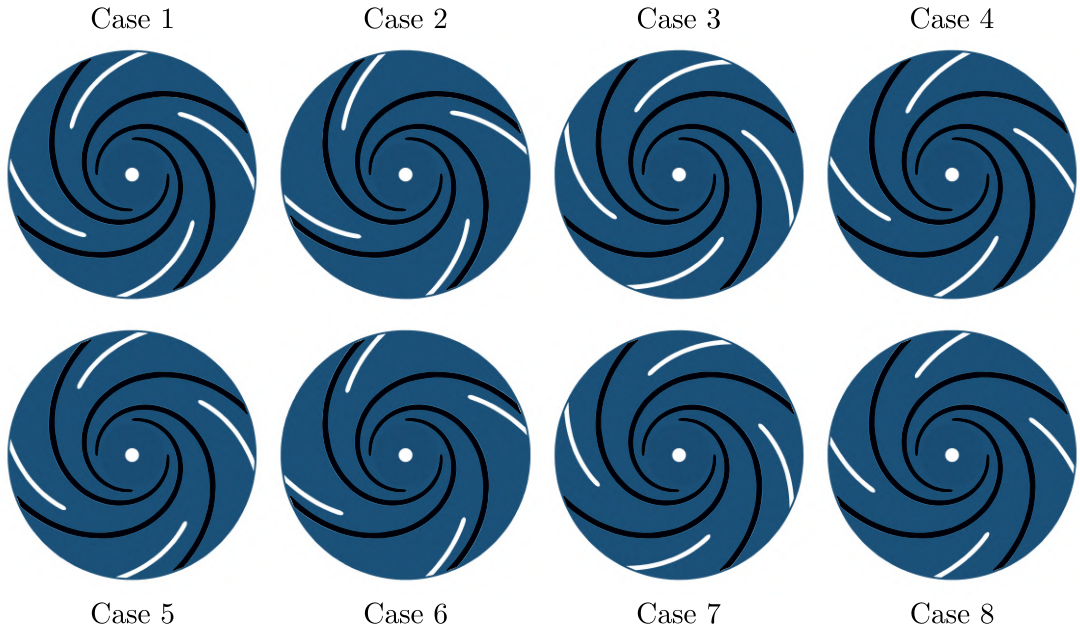

Figure 4.8: Positions of each splitter blade configuration tested.

Table 4.3: Results of simulations.

Case	a $(-)$	θ $(^\circ)$	α_{sp} $(^\circ)$	H (m)	η $(-)$	$T_{sp,rel}$
1	0.4	0.3	-5	32.93	0.56	0.24
2	0.4	0.3	10	31.95	0.55	0.40
3	0.4	0.5	-5	32.95	0.56	0.34
4	0.4	0.5	10	33.67	0.55	0.41
5	0.7	0.3	-5	32.78	0.55	0.16
6	0.7	0.3	10	31.76	0.55	0.20
7	0.7	0.5	-5	31.92	0.55	0.14
8	0.7	0.5	10	33.12	0.55	0.17

imum change over the 8 tested design is about 2%. It indicates that the tested splitter blades do not have a large impact on the efficiency in these configurations for this pump. The graph of main effects and interactions (figure 4.9 and figure 4.10) tells us about the impacts of the different parameters on the head and the relative splitter blade torque. A similar graph can be plotted for the efficiency but is considered irrelevant due to the small variation of efficiency observed.

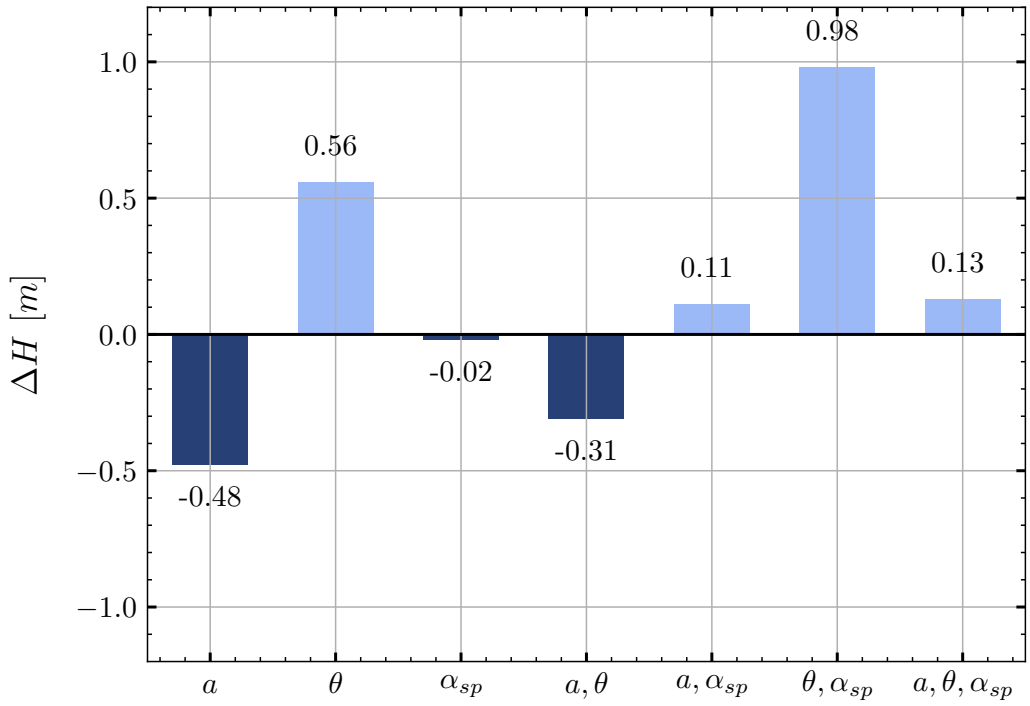

Figure 4.9: Main effects and interactions of the DOE for the Head.

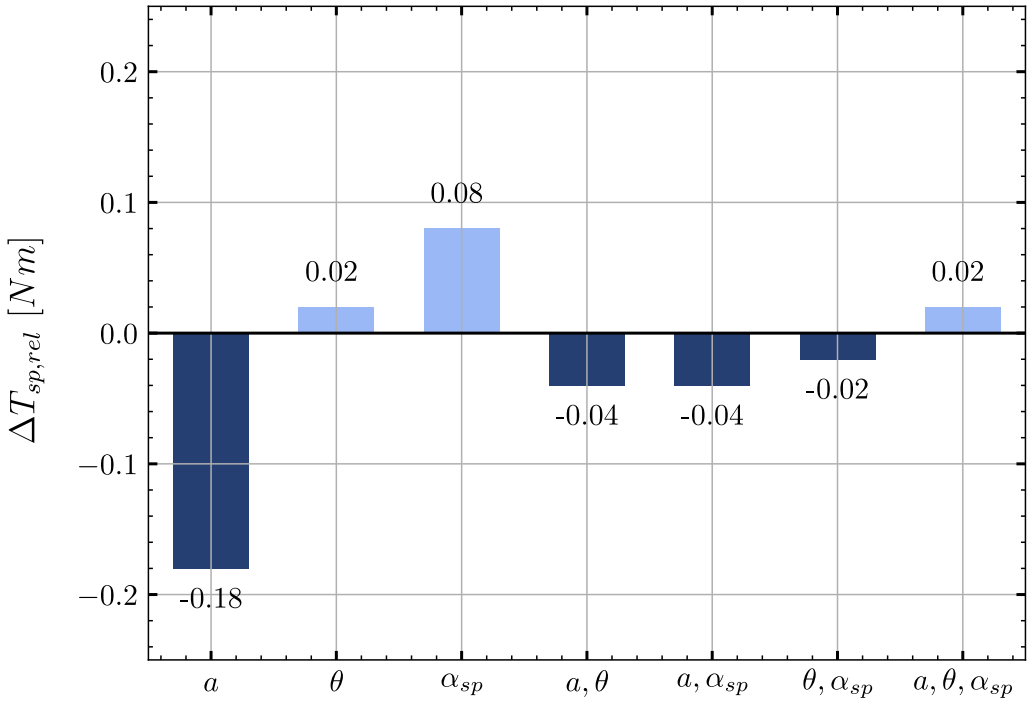

Figure 4.10: Main effects and interactions of the DOE for the Relative Splitter Blade Torque.

The following conclusions can be made about the influence of the parameters on the head at the designed point:

- Main effects
  - The value of -0.48 indicates that when the parameter a (related to the inlet diameter) raises, there is a head loss of 0.48 m. A raise of a indicates smaller splitters. Accordingly, longer splitter blades enhance the head.
  - The head is higher when $\theta = 0.5$. Splitters placed in the middle of the channel enhances the head, for the configurations tested.
  - The relative splitter angle α_{sp} does not have any direct impacts on the head here, although it is expected to have a positive impact on the head, because the head rises with the outlet blade angle.
- Interactions
  - The main interaction is between (θ, α_{sp}). High levels for both parameters place the splitter in the middle of the channel, with a high blade outlet angles (Case 4, 8). The two highest head computed are for these two designs.

In previous studies, higher outlet blade angles for splitter were seen to always rise the head of the pump. Here, it is not directly observed. It is due to Cases 2 and 6, where the upper level for the factor α_{sp} is used, coupled with the lower factor for θ. The resulting position of the splitters is too close to the suction side of the main blades, impairing the work done by the splitters.

For $T_{sp,rel}$, only a and α_{sp} have a relevant effect. As for the head, longer splitter enhances $T_{sp,rel}$. α_{sp} has a positive effect here, indicating that splitters with higher outlet blade angles lead to a higher relative splitter blade torque. These two conclusions follow classic blades' design expectations.

To understand the influence of splitter blades on the whole characteristic curves, unsteady simulations are performed for all designs, except Cases 2 and 6, as it is concluded that the splitters were badly placed. The head characteristics without splitter are also computed, to see the general impact of splitter on the characteristic curves. For all computed designs, 3 points of the curves only are plotted, for time saving purposes at flow rates $Q = [0.3; 1.0; 1.6]Q_d$.

To measure the steepness of the head characteristics, we define a parameter measuring the head drop H_{drop} between the computed head at part load and at the design point. This parameter does not directly indicate if the pump characteristic is stable or unstable, because the head of the pump close to shut off is not evaluated here. The information about instability will only be sure if H_{drop} is positive.

$$H_{drop} = H_{Q=0.3Q_d} - H_{Q=1.0Q_d} \tag{4.6}$$

To evaluate the influence of single parameters, we compare the head drop of the different cases two-by-two.

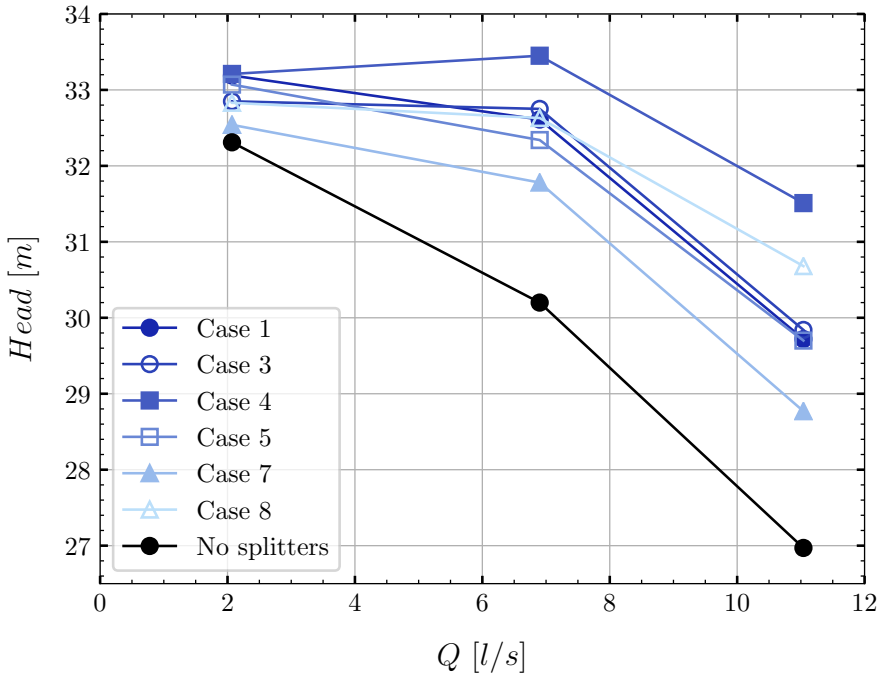

Figure 4.11: Head curve characteristics, unsteady simulations.

Table 4.4: Head drop between part-load and design flow rate.

Case	H_{drop} (m)
1	0.59
3	0.10
4	-0.24
5	0.73
7	0.76
8	0.19
no splitter	2.10

- Influence of a (splitter length): Cases (1-5), (3-7), (4-8) are pairs where θ and α_{sp} are similar and a only changes. The head drop for Cases 5, 7 and 8 is higher than their counterpart. As a result, smaller splitter blades lead to steeper head characteristic, as expected.

- Influence of θ (pitch ratio): Cases (1-3), (5-7) are pairs where α and α_{sp} are similar and only θ changes. Case 1 has a steeper head characteristic than its counterpart. Case 5 and 7 roughly have the same slope. On average, splitters with smaller pitch ratio (closer to the suction side) seem to lead to steeper head characteristic, but the influence is not as clear as other parameters.

- Influence of α_{sp} (splitter outlet blade angle): Cases (3-4), (7-8) are pairs where a and θ are similar and only α_{sp} changes. Cases 3 and 7 have a steeper head characteristic than their counterpart. Splitters with smaller outlet blade angle lead to steeper head characteristic.

According to this simple analysis, the steepest head characteristic should be given by Case 5 (short splitter, closer to the suction side of the main blade, with a smaller outlet blade angle), and the most flat/unstable by Case 4 (long splitters, in the middle of the channel, with a larger outlet blade angle), as it is shown in Table 4.4. For these two cases, additional points are calculated to have more precision about the head characteristics, and most importantly to evaluate the head at part load to conclude about the stability of the pumps. The efficiency (figure 4.13) and shaft power (figure 4.14) are also evaluated.

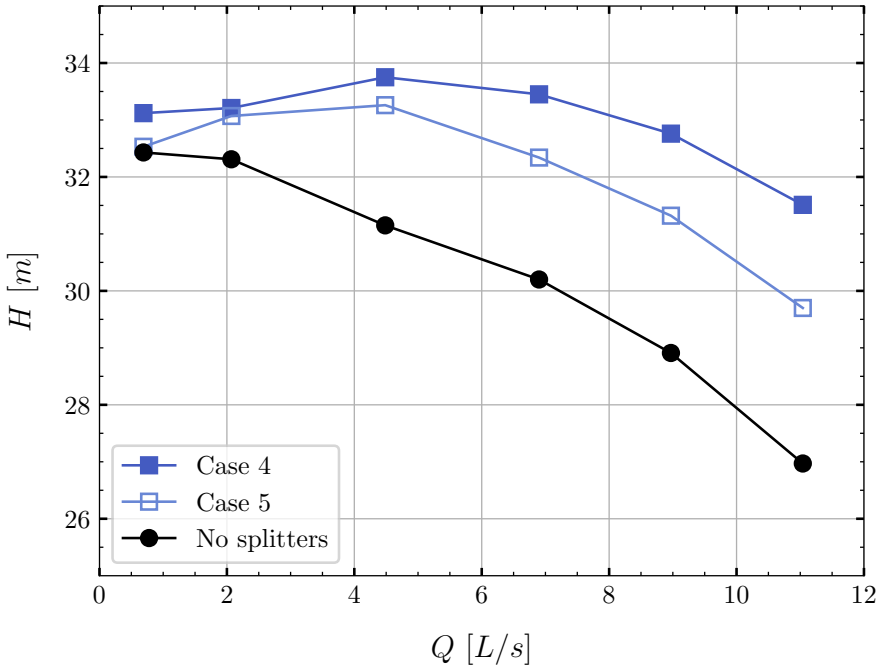

Figure 4.12: Efficiency curve characteristics, unsteady simulations.

For both cases, the head curve largely flattens comparing to the impeller without splitters. At part load, even for Case 5 presenting a large H_{drop}, instability is shown at very low flow rates. The evolution of the efficiency is almost exactly similar for all cases, showing that the splitters do not affect this parameter in this study. In addition, it is clear that the best efficiency point has not been reached, indicating that the computed pumps operate at part-load. Indeed, by looking at the throat area of the volute and comparing it with recommended values from [50], the volute is largely over-designed. The ratio A_{vs}/A_{II} is plotted in figure 4.15 as a function of the specific speed, where A_{vs} is the volute throat area and A_{II} is defined as follow:

$$A_{II} = \pi d_2 b_2 sin(\beta_{2B}) \tag{4.7}$$

The grey area corresponds to the region of highest efficiency. The actual ratio A_{vs}/A_{II} is equal to 0.46, as it should be equal to 0.19 at a specific speed of 32 according to figure 4.15. The actual throat area is thus close to 2.5 times the recommended one and its ratio corresponds to a pump with a specific speed of $n_s = 82$.

As a conclusion, the following statements can be made about the effect of splitter blades on a low specific speed pump:

- Splitter blades, in all configurations, will enhance the head and introduce a flattening or even instability of the head characteristic.

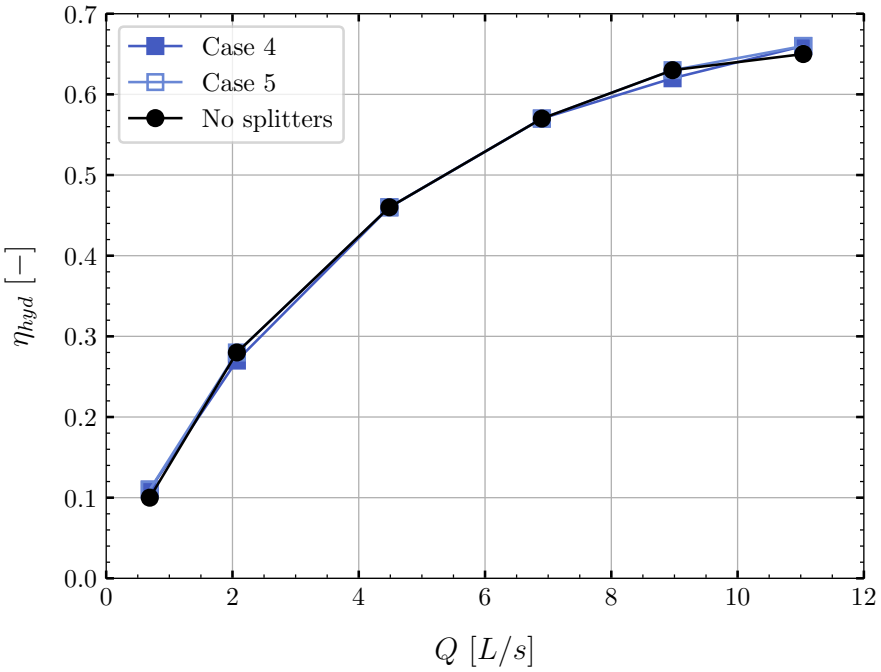

Figure 4.13: Power curve characteristics, unsteady simulations.

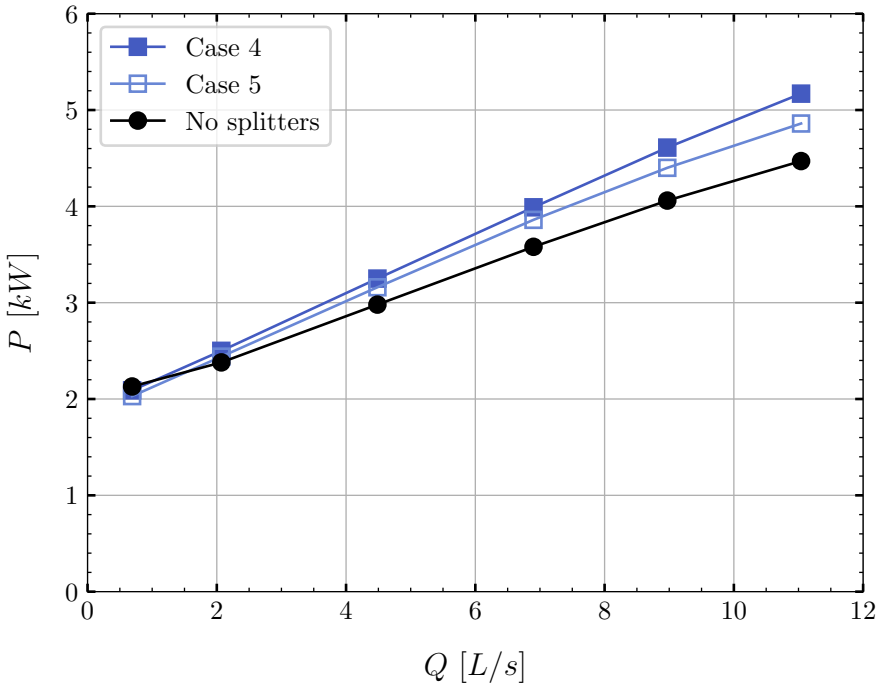

Figure 4.14: Head curve characteristics, unsteady simulations.

- Longer splitter blades with high outlet blade angles show the strongest instability (Case 4), as the head at the designed flow rate ($1.0Q_{design}$) is higher than the head at part-load ($0.3Q_{design}$).
- The circumferential position of the splitter in the channel has a smaller impact than the other 2 parameters studied, although a placement closer to the suction side of the main blade is shown to be favorable for stability purposes.

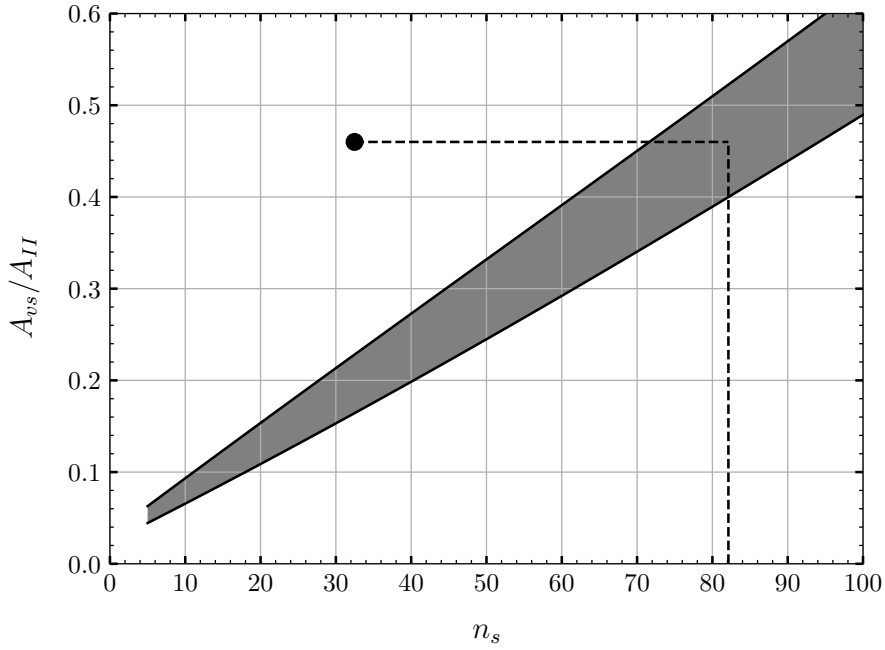

Figure 4.15: Volute throat area recommended values.

- The combination of high outlet splitter blade angles close to the suction side of the main blades lead to ineffective splitter as the head is poorly improved, due to flow blockage in the impeller channel (Case 2 and 6).

These conclusions are in accordance with other studies on the influence of splitter blades.

4.2. Study 2: Effect of the addition of 1 and 2 splitters per impeller passage

The objective of this study is the analysis of the influence of the addition of one and two splitter blades per impeller passage. The difference with the previous study lies in the fact that the optimal placement of a single splitter is not of interest here. Rather, the general influence of the addition of a second splitter on the main flow features is the target of the study.

The pump studied differs from the previous one. First, the volute design has been changed to a more appropriate one at this specific speed with a smaller volute throat area, although the BEP is still located at higher flowrate than the design point. The volute design is a result of a study presented in the Volute throat area study. The volute design is unconventional, as it does not respect the classic design rule of the conservation of angular momentum, or constant cross-sectional velocity. The area of the volute rapidly increases close to the throat area. This design choice has been made to ensure high performance of the pump at high-flow, and avoid a rapid head drop due to the choked flow at the volute throat. Lastly, the pump is scaled by a ratio 1/1.6 compared to the previous study. The impeller diameter is reduced from 320 mm to 200 mm. That modification is made to reduce the cost of the experiment used to validate the numerical results of this study. The main parameters of the pump are also scaled using the affinity laws for a constant

rotor speed and a different diameter. The new pump parameters used in this study are seen in table 4.5.

Table 4.5: Pump parameters (Study 2).

Designation	Symbol	Value	Units
Rotor speed	N	1450	RPM
Design head	H_d	12.5	m
Design flow rate	Q_d	0.00168	$m^3 \cdot s^{-1}$
Specific speed	$n_s = 3.65N\frac{Q_d^{0.5}}{H_d^{0.75}}$	32	-
Impeller outlet diameter	d_2	200	mm
Impeller outlet width	b_2	3.75	mm
Impeller outlet blade angle	β_{2B}	25	deg
Main Blade number	Z	4	-

4.2.1. Splitter blade configutation

Three impellers are designed. The first impeller has 4 main blades. The second impeller has 8 total blades (4 main blades and 4 long splitters) and the third impeller has 12 total blades (4 main blades, 4 long splitters and 4 short splitters), see Figure 4.16 for the splitter leading edge position and Figure 4.17 for a visualization of the splitters in the impeller. The splitter blades follow the definition of the main blades (i.e., blade centerlines follow the same blade angle). The long splitter is not located in the middle of the passage but displaced towards the suction side of the main blade. The short splitter is placed between the pressure side of the main blade and the suction side of the long splitter blade. Preliminary computations revealed that placing the short splitter in this position rather than close to the suction side of the main blades helped in the suppression of the local eddy in the impeller channels. Because the influence of splitter blades is of interest in this study, the three cases are labelled Case 0sp, Case 1sp and Case 2sp, respectively, for the case with zero, one and two additional splitter blades per impeller passage. The sidewall gaps have a constant thickness of 2 mm for the gap on the hub side and 3.125 mm for the gap on the shroud side. The splitter blades parameters can be seen in table 4.6.

Table 4.6: Splitter parameters (Study 2).

	a	d_{sp}/d_2	θ	α_{sp}
splitter 1	0.48	0.63	0.35	0
splitter 2	0.64	0.74	0.63	0

4.2.2. CFD Setup

The guidelines presented in the Methods chapter are respected in this study. As a result, a mesh adopting the Low-Reynolds number treatment method is used. The average value of y^+ at all walls is 1.3. This criteria is not respected at the trailing edge of the impeller

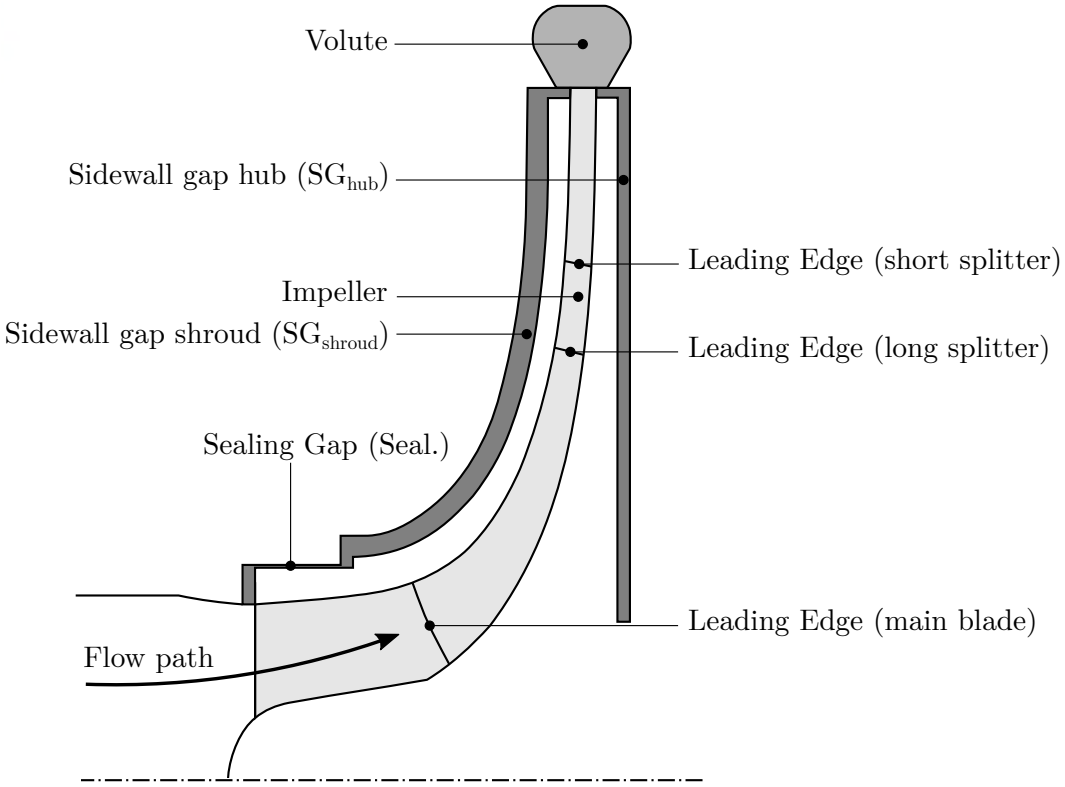

Figure 4.16: Meridional section and placement of leading edges for the 3 studied cases.

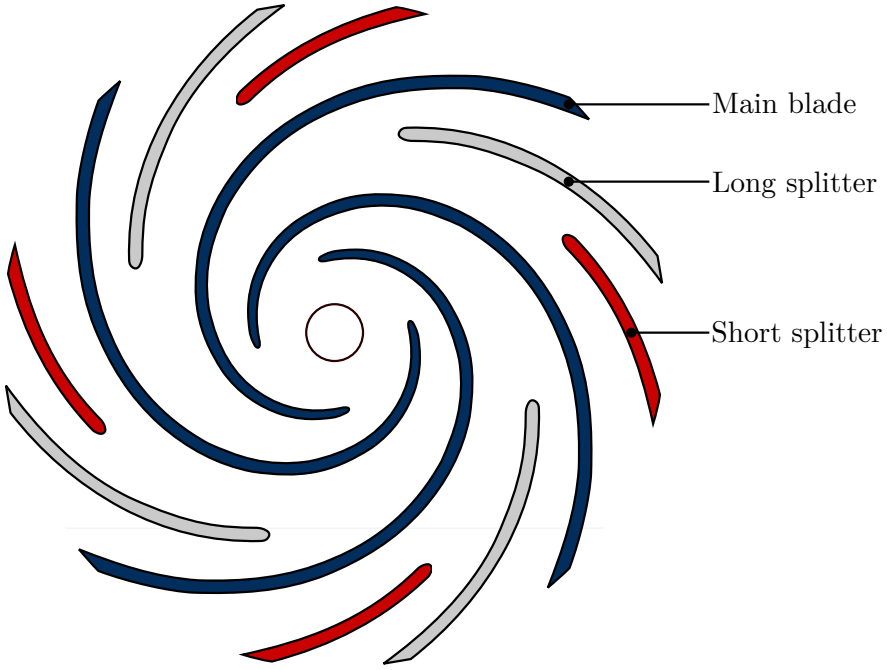

Figure 4.17: Splitter blades position for the 3 studied cases.

where flow separation is evident. The meshes of the different fluid domains are created using the pre-processor `ICEM-HEXA 19.1` and are fully hexahedral. Due to the inability of `ANSYS-TurboGrid` to mesh an impeller with 2 splitters, it has been decided to mesh all impellers with `ICEM-HEXA 19.1` to have a similar blocking strategy and so a similar

mesh to avoid potential numerical differences. A grid convergence analysis is performed for Case 0sp on three parameters: the head, the torque and the efficiency. The results can be seen in figure 4.18. The total cell count of each case is 15.4, 16.6 and 17.2 million cells for Case 0sp, Case 1sp and Case 2sp, respectively. The difference in mesh size is due to the impellers only. The addition of splitters requires a larger mesh count, especially due to additional walls in the channels where the mesh needs to be refined. The full mesh for Case 0sp can be seen in figure 4.19 and the mesh of the three impellers in figure 4.20.

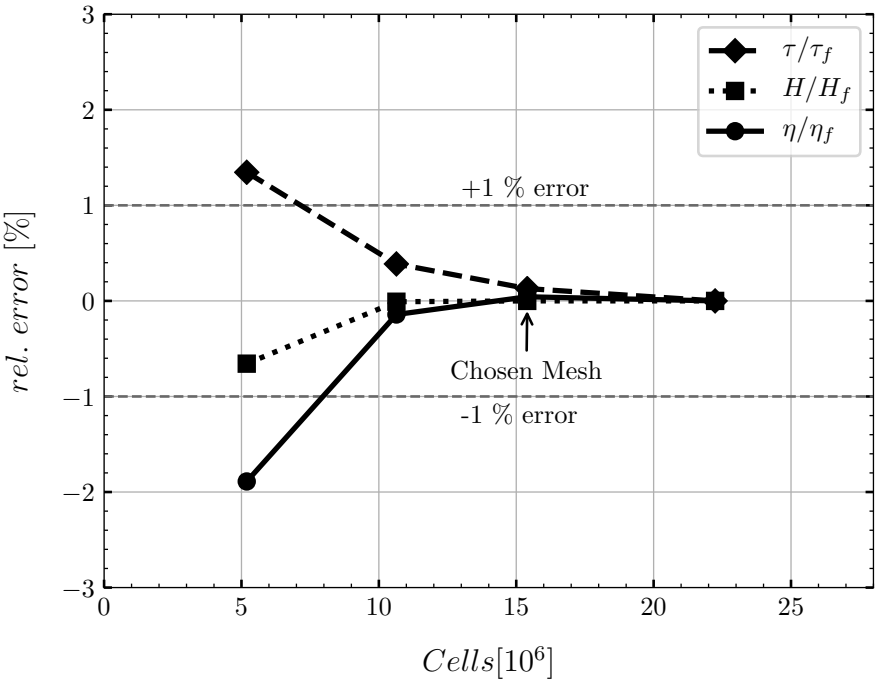

Figure 4.18: Grid convergence analysis results for Case 0sp.

4.2.3. Experimental validation

The validation of the numerical results is done for the three impellers. The impellers are 3D printed using the Fused Deposition Modeling (FDM) technology with Nylon 12. This method and material were also used for a pump with comparable specific speed with higher performances by Olimstad [46]. The volute casing is CNC-milled from 2 blocks to ensure smooth hydraulic surfaces. The material used is Aluminium 5754, that has good corrosion resistance. The inductive flow meter, torque transducer and pressure transducers, respectively, have errors of ±0.3%, ±0.2% and ±0.35% of the measured value. The complete experimental setup is presented in the section Experimental approach. This part aims to only present the results.

The steady state condition of the system was observed before recording a point of the characteristic curve. Each point is the result of averaging over 30 seconds with a sampling frequency 2000 Hz. The results for the head and the hydraulic efficiency are seen in Figure 4.21, Figure 4.22 and Figure 4.23 for Case 0sp, Case 1sp and Case 2sp, respectively. The standard deviation for each measurement is shown in the grey band (Type A uncertainty). The standard deviation of the measured variables is plotted instead of the measurement uncertainties (Type B uncertainty), because the uncertainty of each measured parameters is less than 1%. The standard deviation reaches up to 8% of the measured value for the

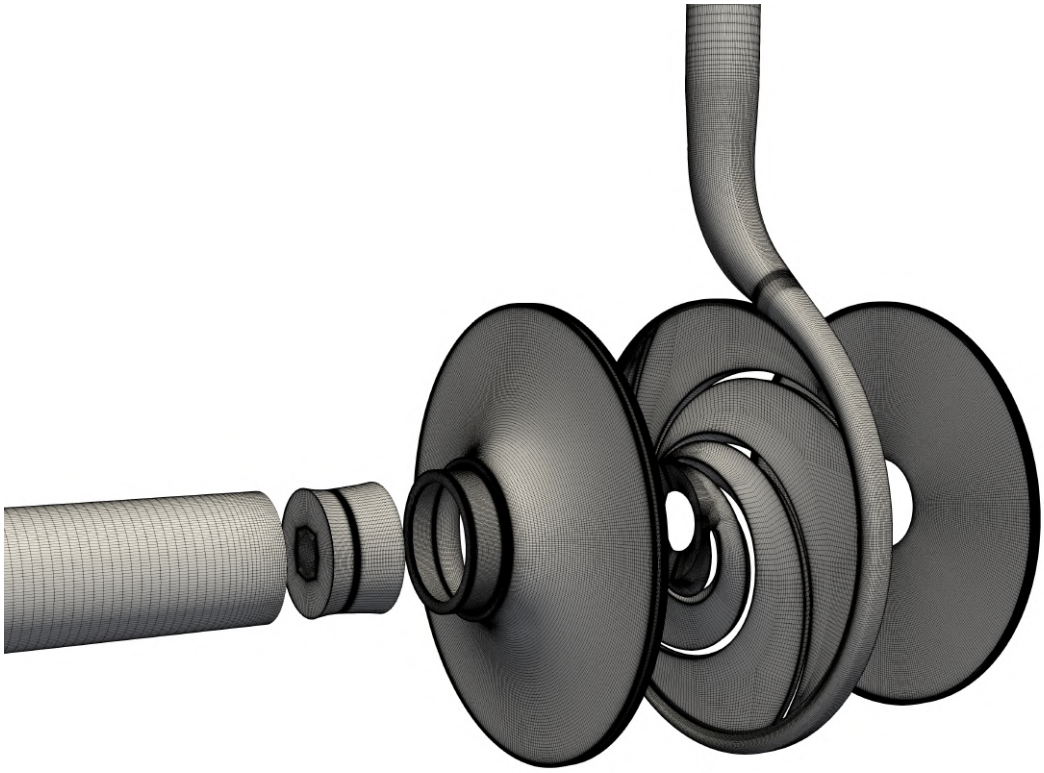

Figure 4.19: View of the grid for Case 0sp.

Figure 4.20: View of the impeller grid for Case 0sp, Case 1sp and Case 2sp.

head for Case 0sp. The results of the CFD computations are also presented on these figures and serve as validation of the numerical results.

The experimental and numerical results are in good agreement for the head especially. For the hydraulic efficiency, a discrepancy is observed for all cases. The efficiency for all cases is similar and averages to 56% for the CFD and 50% for the experiment at the design point. The discrepancies in efficiencies may have several causes but the main one certainly resides in the fact that the impellers are 3D printed, and so their surface roughness influences the torque produced. It should also be noted that the hydraulic efficiency has been calculated by subtracting the static torque of the pump. The static torque has been

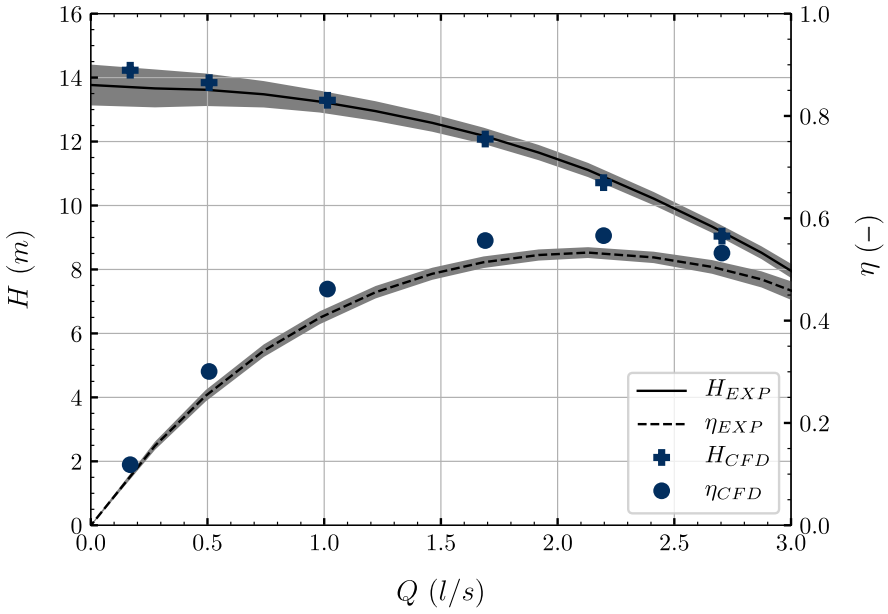

Figure 4.21: Head and efficiency as a function of the flow rate for Case 0sp.

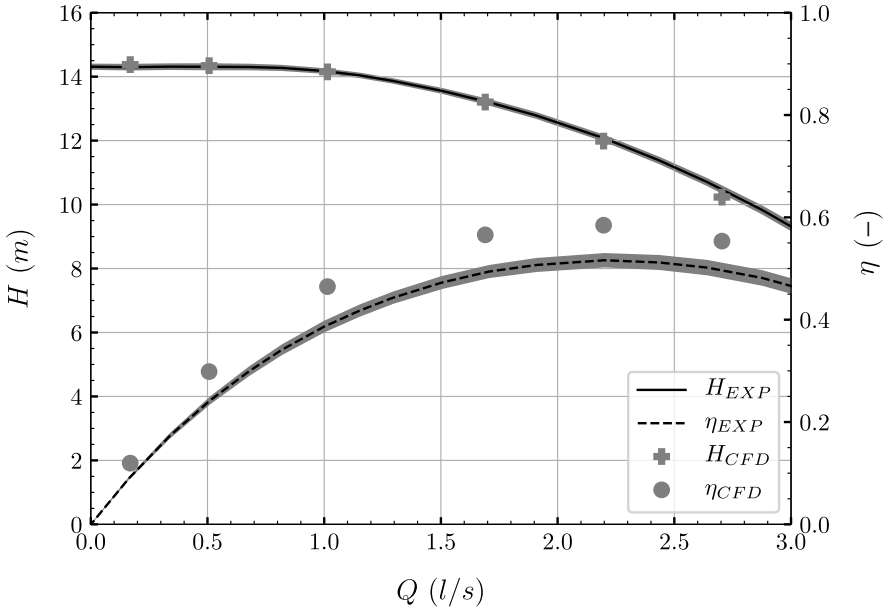

Figure 4.22: Head and efficiency as a function of the flow rate for Case 1sp.

measured by flooding the hydraulic circuit without impeller and by rotating the shaft at the rated speed. This way, the presented hydraulic efficiency does not include losses in the shaft seal and bearings. Another interesting point is the standard deviation amplitude of the measured pressure, which is considerably reduced with the presence of splitter blades, indicating that the pressure and flow rate fluctuations decrease, providing a more stable flow delivery with lower pulsations.

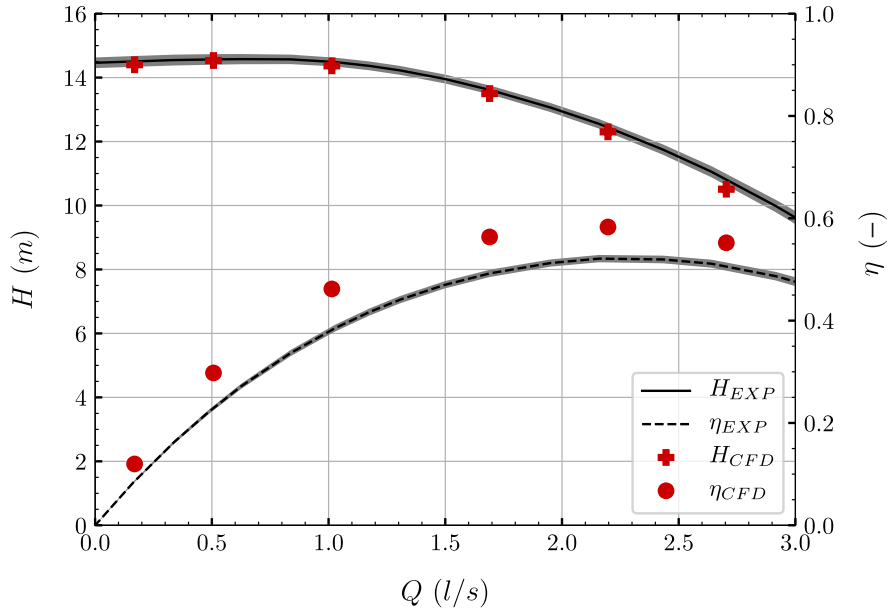

Figure 4.23: Head and efficiency as a function of the flow rate for Case 2sp.

4.2.4. Results and Discussion

Comments on the integral results (head, hydraulic efficiency) are based directly on the experimental values. Comments on flow features and loss analysis are based on CFD results. All results are time-averaged.

Integral parameters

The integral results showing the head and the efficiency on a single graph for all cases are plotted in Figure 4.24. The first noticeable point is that the head increases with the addition of splitters. At the design point, the increase in head relative to Case 0sp is 8.2% and 11.3% higher for Case 1sp and Case 2sp, respectively. The hydraulic efficiency shows a different trend based on the case. At low flow, it is Case 0sp, without splitters, that presents the highest efficiency. This trend is reversed at high flow. The maximum hydraulic efficiency for each case is similar at 52%, but is always located at higher flow rates than the design point. The BEP is located at values Q/Q_d of 1.24, 1.30 and 1.34 for Case 0sp, Case 1sp and Case 2sp, respectively, showing that the introduction of splitters displaces the BEP to higher flow rates.

It is clear that the introduction of splitters in impeller passages has a negative impact on the stability of the head curve at low flow. The head is stable for Case 0sp, strictly flat for Case 1sp and raises slowly from the shut-off point for Case 2sp until $Q/Q_d = 0.37$. It should be noted that the numerical simulations were able to capture the slight head instability for Case 2sp.

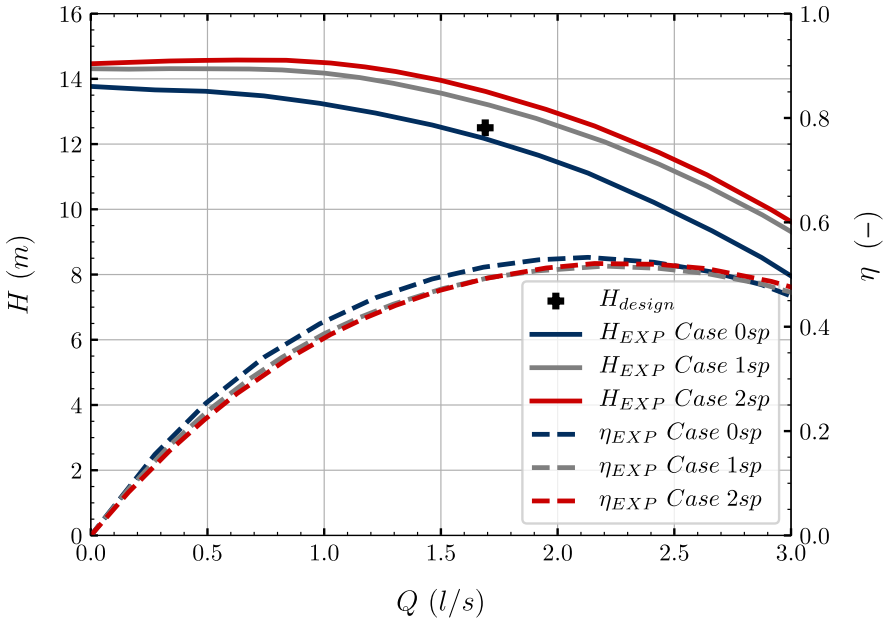

Figure 4.24: Experimental results for the 3 tested impellers.

Loss analysis

To better understand the influence of splitter blades on the pump performance, a power loss analysis is performed in each numerical domain. For a domain i, the formula to calculate the power loss in the domain $P_{L,i}$ is given by equation (4.8).

$$P_{L,i} = \sum P_{\tau,i} + P_{in/out,i} \tag{4.8}$$

$P_\tau = \omega\tau$ is the power transferred to the fluid measured at rotating walls, where ω is the rotating speed of the wall in rad/s and τ the torque in Nm. The second part $P_{in/out} = \int \frac{p_T}{\rho} d\dot{m}$ measures the power entering and leaving a domain. Essentially, this formula is related to the total pressure loss in each numerical domain.

All losses are scaled by the shaft power at the design point for each respective case, to allow for a comparison of relative losses. The numerical domains investigated are the impeller, the volute and the sidewall gaps (shroud and hub side separately). The losses in the suction pipe are not considered because very low.

First, the total relative losses are plotted as a function of the flow rate in Figure 4.25.

At low flow, the relative losses are slightly higher for Case 0sp but very similar at design point and higher flow rates. This is expected as the hydraulic efficiency is similar for all cases. The detail of relative losses per domain can be seen in Figure 4.26. The impeller relative losses are similar over the whole range of flow rates. Despite the addition of splitter blades and absolute increase of power losses (skin friction of additional blades and shock loss at the leading edges), the impeller relative losses are not impacted. Gülich [1] suggests that the introduction of disruptive elements in the flow passages of low specific speed impellers implies virtually no loss due to the transfer of energy which is mostly centrifugal. The relative losses in the sidewall gaps (both hub and shroud side) are higher for Case 0sp. The losses in the gaps are mainly a function of the impeller diameter and the rotor speed, so the absolute losses for all cases are similar. Because Case 0sp develops less power (due to lower blade number), the relative power dissipation in the gaps is higher. The volute is the domain where Case 1sp and Case 2sp have significantly higher relative

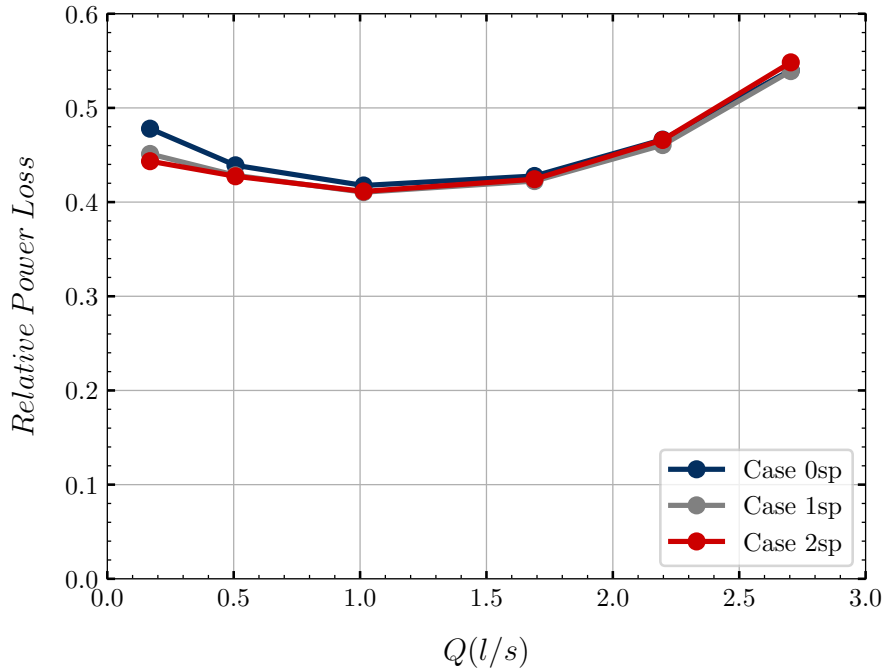

Figure 4.25: Relative total losses.

losses than Case 0sp. At the design point, the relative losses are 21% and 17% higher for Case 2sp and Case 1sp, respectively, compared to Case 0sp.

The reason for the increased volute losses is not straightforward, as the splitter blades' role is also to provide a better flow guidance and output a more uniform flow into the volute. In fact, the main known effect of splitter blades on the impeller flow is the suppression of the jet-wake flow pattern. The reason for this pattern is a local eddy located on the pressure side of the blade and visualized in Figure 4.27, which represents the relative velocity in the impeller at the design point for all cases. There is a region with zero relative velocity, where the local eddy appears, for Case 0sp, and the introduction of splitter blades suppresses this eddy. More uniform values of the relative velocity are present in the impeller as a result. At the splitter blades' leading edges, an acceleration of the relative velocity can be seen on the suction side, indicating that the blades are not aligned with the flow. Despite this fact, we saw that the relative impeller losses are not affected by the splitter blades.

An analysis of the flow at the outlet of the impeller allows to quantify the influence of the splitter blades on the flow entering the volute. Velocity components are extracted at $r = r_2$ using the post processor `CFD-Post` with a discretization of 0.5 degrees in the circumferential direction and 9 points in the spanwise direction totalling 6480 data points extracted at the impeller outlet surface.

The slip factor γ, see Equation (4.9), is a parameter quantifying the deviation of the flow from the blade angles.

$$c_{u2\infty} - c_{u2} = (1 - \gamma)u_2 \tag{4.9}$$

$c_{u2\infty}$ is the circumferential flow velocity at the impeller outlet obtained in a perfectly blade congruent flow, c_{u2} is the actual circumferential flow velocity and u_2 is the blade tip velocity. A value $\gamma = 1.0$ means a blade-congruent flow. Smaller values of γ means more deviation between flow and blade angles. The slip factor is plotted against the flow rate in Figure 4.28. It is clear that the introduction of splitter blades has a positive impact

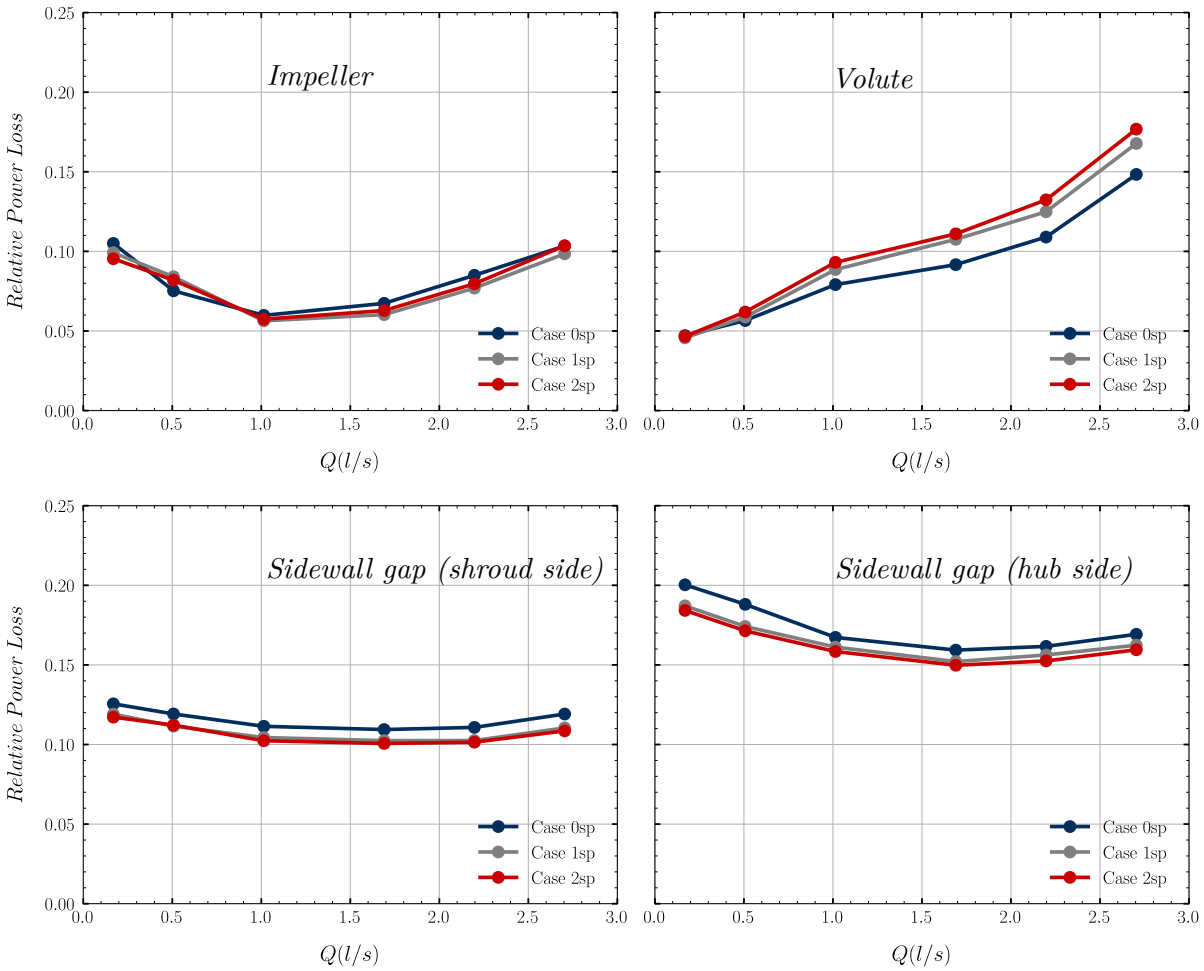

Figure 4.26: Scaled relative losses per domain.

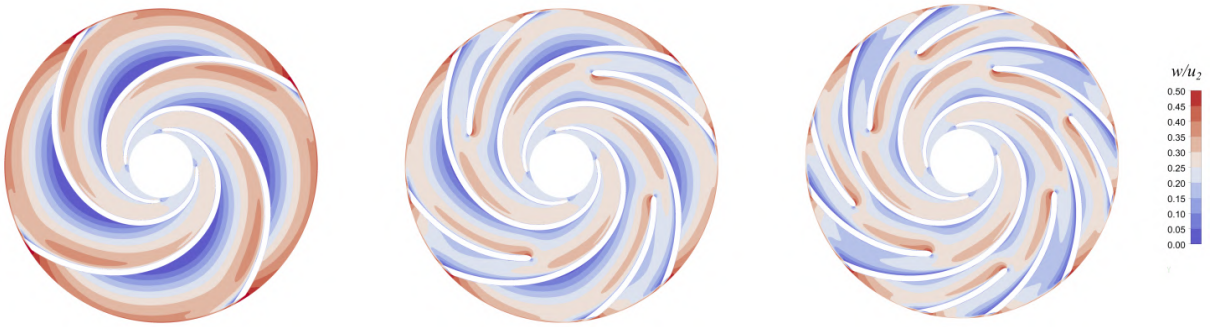

Figure 4.27: Relative velocity comparison at design point.

on the slip factor and that high values are obtained thanks to their presence. Values for Case 1sp and Case 2sp are up to 10% and 15% higher than Case 0sp at the design point.

Higher slip factors are a consequence of a higher circumferential velocity c_{2u} at the impeller outlet, which leads to a higher pump head based on the Euler equation of turbomachinery. However, the absolute velocity c_2 at the impeller outlet is also higher with the introduction of splitters, which leads to higher wall friction losses in the volute. This can be seen in the wall shear stress at the volute wall. Figure 4.29 represents the ratio of the wall shear stress on the volute wall between the Case 2sp and the Case 0sp. The wall

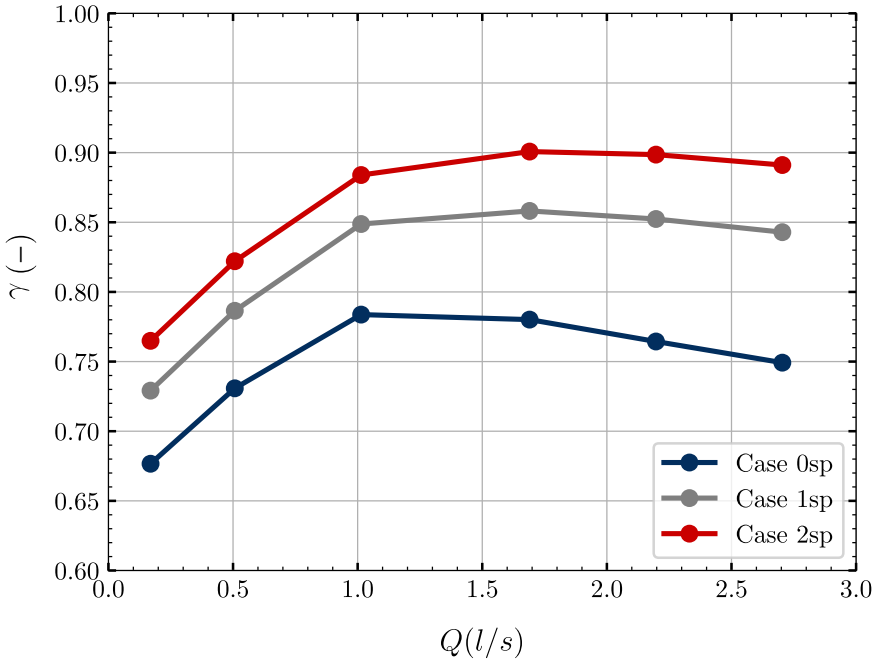

Figure 4.28: Slip factor as a function of the flow rate.

friction is higher in the whole spiral section of the volute. Large ratio is observed in the diffusing part due to small values of the absolute wall shear stress in that region. On average, the wall shear stresses at the volute wall for Case 2sp and Case 1sp are 21% and 15% higher than Case 0sp. This fact explains the high power losses in the volute seen in Figure 4.26. Here, the benefit of the splitter blades in other domains are balanced with the friction in the volute domain.

Flow in the impeller

The influence of the splitters on the impeller flow and especially the local eddy is investigated. Figures 4.30 and 4.31 show the time-averaged streamlines in the impeller at all flow rates for the three designs investigated. To each row corresponds a different flow rate starting from $10\%Q_d$, then $30\%Q_d$ and $60\%Q_d$ for figure 4.30 and starting from $100\%Q_d$, then $130\%Q_d$ and $160\%Q_d$ for figure 4.31. Each column presents a different design starting from Case 0sp on the left, Case 1sp in the center and Case 2sp on the right.

Starting from the lowest flow rate at $10\%Q_d$, the influence of splitters on the flow is already clear. For Case 0sp, three large eddies are present on the pressure side of the main blade, leaving approximately half the impeller channel for healthy streamlines to develop. The fact that the streamlines displayed are time-averaged shows that these eddies rotate with the impeller and are not appearing and disappearing at a certain frequency. For Case 1sp, the flow is already enhanced and a single large eddy is present on the main blade pressure side. A small eddy is also present on the splitter pressure side. For Case 2sp, the large eddy on the pressure side is suppressed as the short splitter does not leave enough space for the eddy to develop. It seems that the flow is improved on the pressure side of the main blade and that as a result, the flow rate is smaller on the suction side of the main blade, leading to a small eddy development there. Eddies are also present on the pressure side of both splitters. At $30\%Q_d$, a large eddy remains on the pressure side of the main blade for Case 0sp. The streamlines go around the eddy and get closer to

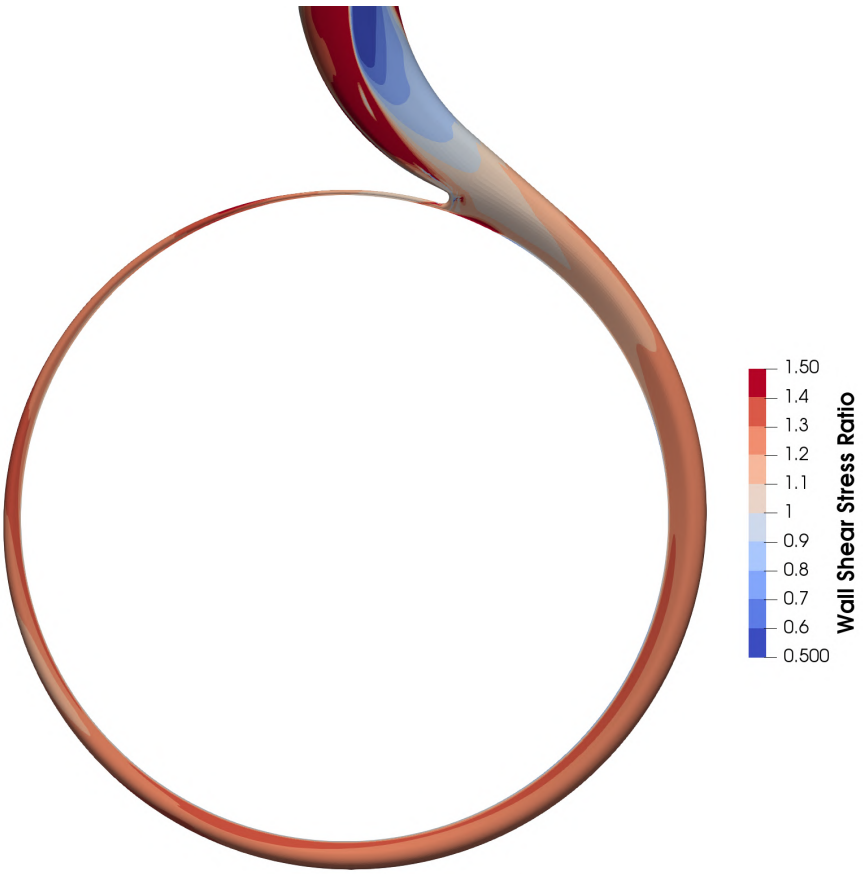

Figure 4.29: Volute Wall Shear Stress ratio (Case 2sp relative to Case 0sp) at design point.

the trailing edge on the pressure side. These streamlines have a flow angle close to zero degree. Case 1sp shows a great improvement of the streamlines as only two small eddies are present on the pressure side of the main blade. The flow close to the suction side is relatively well. For Case 2sp, no local eddies are present on the pressure side of the main blade at all and a small eddy is present on the suction side, as for the previous flow rate. At 60%Q_d, Case 0sp presents the same flow features as the precedent flow rate, simply with a smaller local eddy. The deflection of the streamlines compared to the blade angles remains important. For Case 1sp and Case 2sp, the local eddies are totally suppressed and the flow is adequate for the most part. A large flow deflection is observed for Case 1sp between the main blade pressure side and the splitter, that is less apparent for Case 2sp. The splitters do not give enough space to the flow for being highly deflected.

At the design point at 100%Q_d, for Case 0sp the flow is once again very similar as with the previous flow rate. The local eddy is smaller but still present, the flow is largely deflected towards the impeller outlet and the relative velocity difference between the pressure and suction side is substantial. For Case 1sp and Case 2sp, the flow is for the most part healthy. Slight misalignment of the leading edge compared to the streamlines is observed. At higher flow rate, for 130%Q_d and 160%Q_d, the comments are alike. For Case 0sp, the local eddy finally disappears. The streamlines are still highly deflected at the impeller outlet and a low velocity zone is present on the pressure side of the main blade. For Case 1sp and Case 2sp, the flow is more uniform compared to Case 0sp, despite local acceleration present at leading edges of splitter blades.

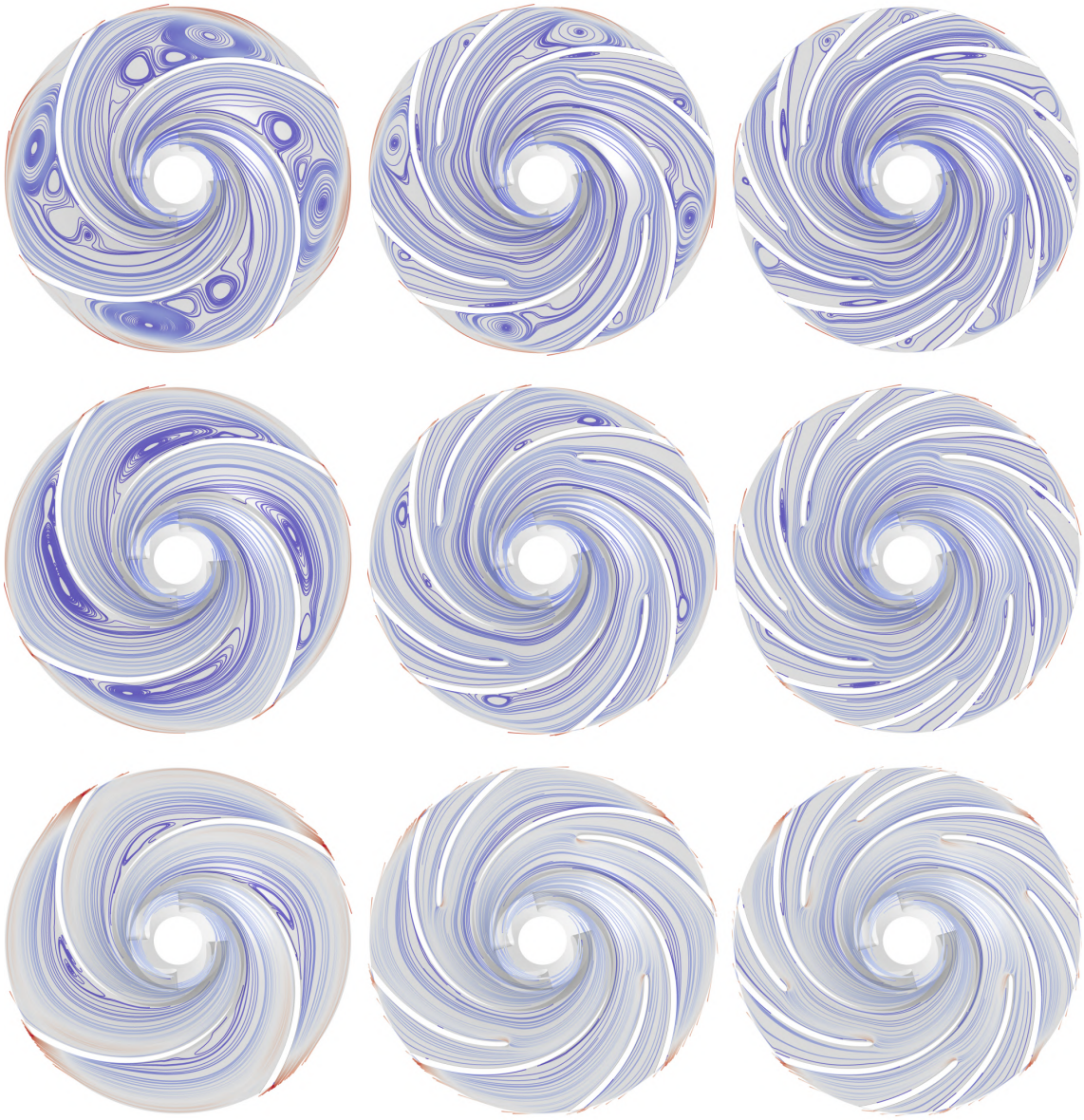

Figure 4.30: Streamlines of time-averaged flow. From left to right: Case 0sp, Case 1sp, Case 2sp. From top to bottom: $Q = 10\%Q_d$, $Q = 30\%Q_d$, $Q = 60\%Q_d$.

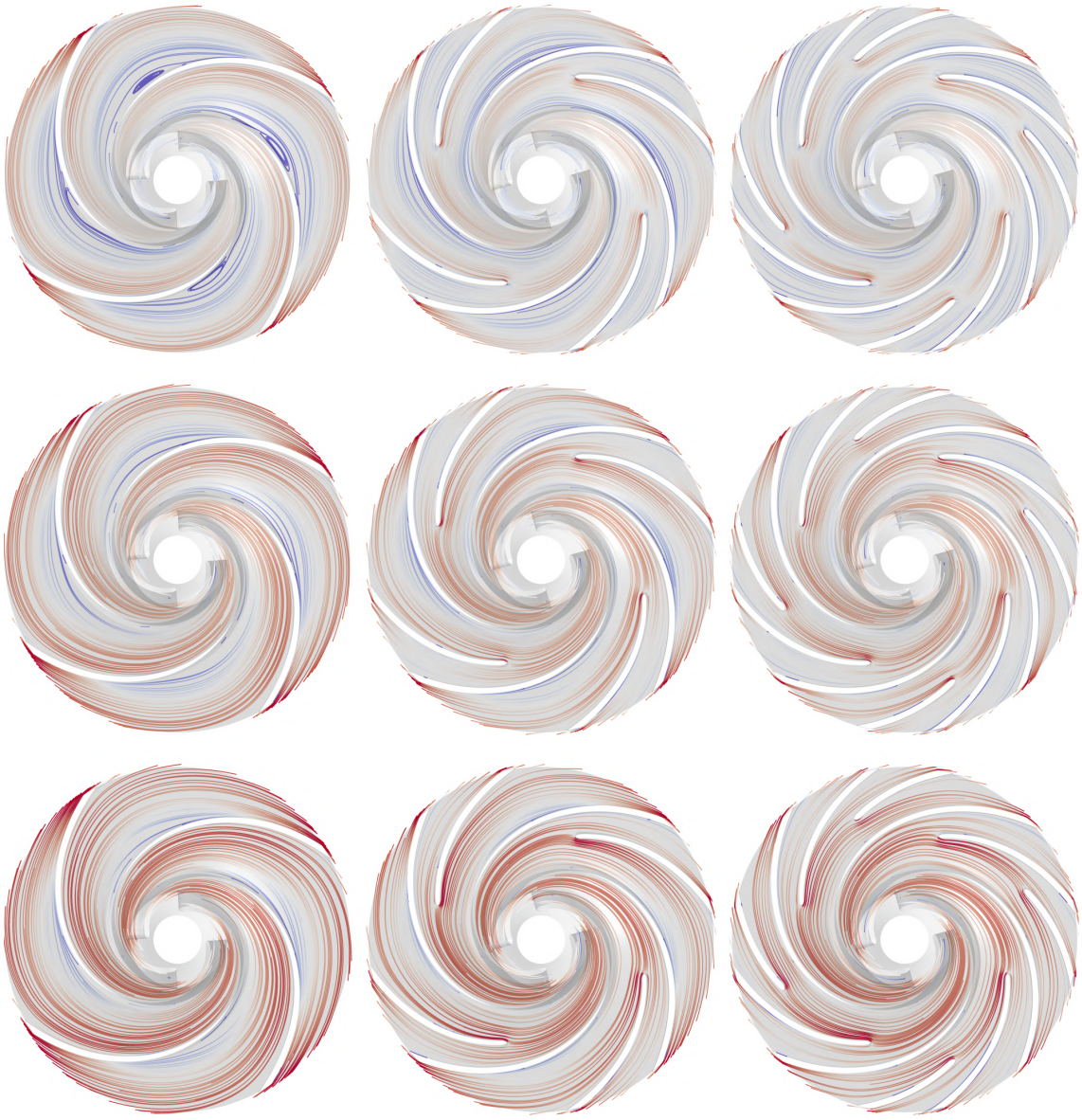

Figure 4.31: Streamlines of time-averaged flow. From left to right: Case 0sp, Case 1sp, Case 2sp. From top to bottom: $Q = 100\%Q_d$, $Q = 130\%Q_d$, $Q = 160\%Q_d$.

Effect of splitters on pump transients

A simple analysis of the effects of splitter blades on transients of the pump is made. The objective is to evaluate if splitter blades help in the reduction of oscillation of transient flow features. The results are based on both experimental and numerical results.

Analysis based on experimental results

The pressure fluctuations in the suction and discharge pipe are analyzed thanks to the pressure transducer installed in the test bench, see figure 3.16. The probe p_1 in the suction pipe is placed 150 mm upstream the leading edge of the impeller. The probe p_2 in the discharge pipe is placed 365 mm from the center of rotation of the impeller.

The quantity of interest is the peak-to-peak difference of the oscillation. The variable Δp_1 in figure 4.32 represents this difference. The signal represented is the pressure in the suction pipe at the design point for Case 0sp. On the x-axis, the period t represents 1 impeller rotation, or about $0.041s$. It is clear that the pressure oscillation is directly affected by the blade as 4 peaks are observed during a single period.

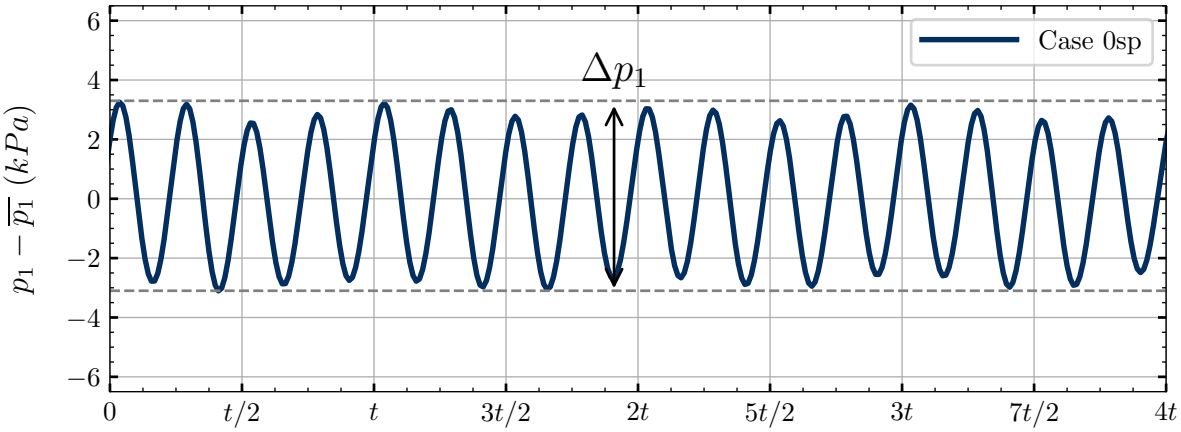

Figure 4.32: Pressure measured in suction pipe at design point, Case 0sp.

The peak-to-peak difference is plotted against the flowrate for Case 0sp, Case 1sp and Case 2sp for probes p_1 (figure 4.33) and p_2 (figure 4.34).

At shut-off, the pressure fluctuations in the suction pipe Δp_1 are higher for Case 0sp, about three times more than Case 2sp. The pressure fluctuation then diminishes to be in the same order of magnitude close to the design point. Past the design point, fluctuations for all cases are roughly equal and start to increase. The main difference between the three cases is at part-load. It can be assumed that the flow at the impeller outlet is responsible for the observed differences. As seen in figure 4.30, the flow in the impeller is greatly improved at low flow thanks to the splitter blades. The recirculated flow from the outlet of the impeller towards the impeller eye is pulsating with the blade passing the tongue of the volute. For Case 0sp, the large velocity difference at low flow in a single impeller channel (due to most of the channel blocked by eddies) creates large pressure pulsation in the pump travelling back to the suction pipe. This phenomenon is reduced with the presence of splitter blades. As the flow increases, the flow in all impeller becomes more uniform. The difference in pressure pulsation between cases also reduces and the advantages of splitter blades on that issue disappears. In the discharge pipe, the pressure fluctuations Δp_2 leads to different results. Overall, the three cases have a similar trend

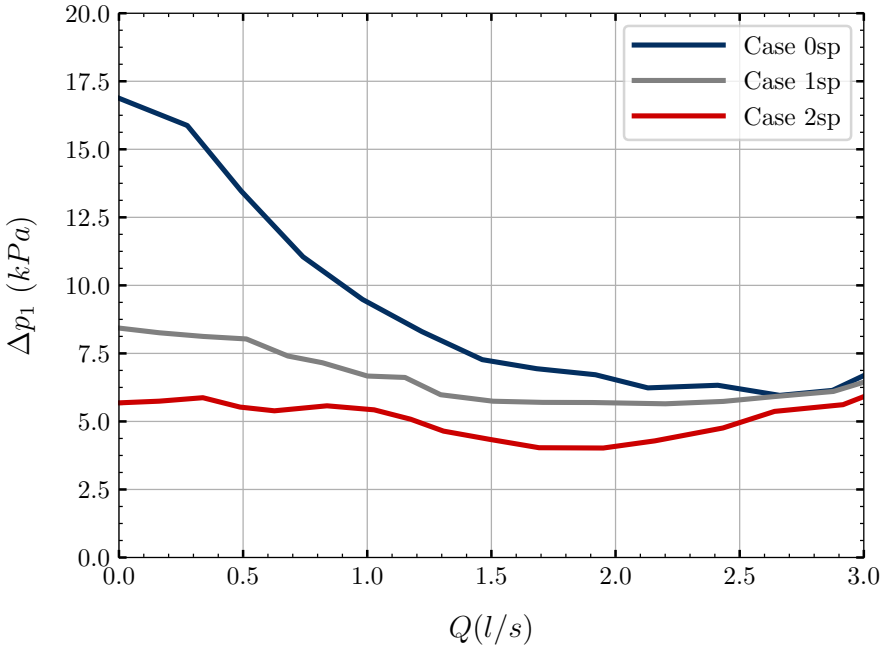

Figure 4.33: Peak-to-peak pressure difference, suction pipe.

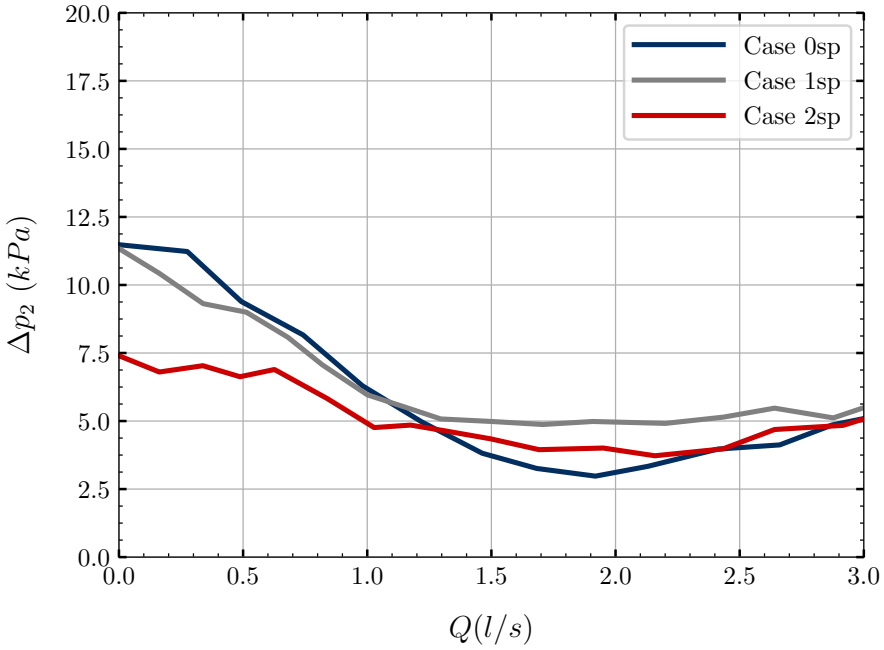

Figure 4.34: Peak-to-peak pressure difference, discharge pipe.

and Δp_2 reduces with increasing flow rates. At shut-off, Case 2sp presents the lowest pressure fluctuations. Because the probe p_2 is located relatively far from the impeller, it is difficult to conclude about the results. The pressure pulsations may have already been damped.

Analysis based on numerical results

The oscillation of hydraulic forces on the impeller is also to be taken into account, both radial and axial. Because no devices were available to record those forces experimentally, CFD results will be used in this part of the analysis. The same principle is applied as with

the pressure probes and the peak-to-peak force difference is of interest. For the radial and axial forces, the value of interest is given by equations 4.10 and 4.11 respectively.

$$\Delta F_{rad} = F_{rad,MAX} - F_{rad,MIN} \tag{4.10}$$

$$\Delta F_{ax} = F_{ax,MAX} - F_{ax,MIN} \tag{4.11}$$

Because the hydraulic forces were not discussed yet, they are plotted alongside the peak-to-peak oscillation in figure 4.35 (radial force) and figure 4.36 (axial force).

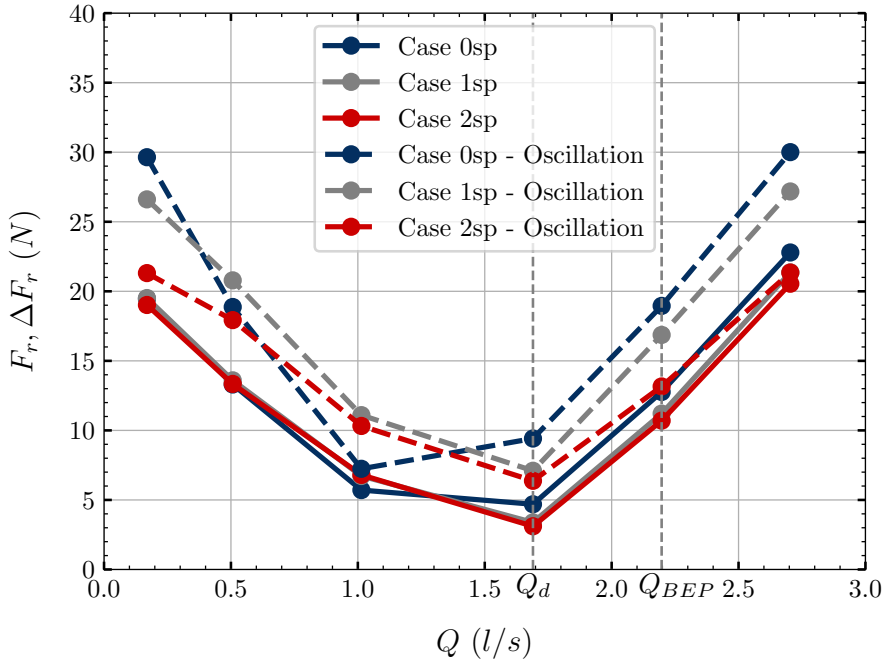

Figure 4.35: Radial force and peak-to-peak force difference.

Figure 4.35 shows both the radial force average values (solid line) and ΔF_r (dashed line). The first observation is that the splitter blades scarcely impact the radial force in the pump as the values are comparable at all flow rates. Secondly, the oscillation of the radial force is higher than its averaged value. The case with 2 splitters, Case 2sp, shows slightly lower values of ΔF_r on average, but once again the results are comparable.

Figure 4.36 shows both the axial force average values (solid line) and ΔF_{ax} (dashed line). The axial force in the pump is related to the head produced by the impeller. As a result, the axial force produced by Case 1sp and Case 2sp is higher than Case 0sp. About the oscillations of the axial force ΔF_{ax}, there is a clear trend, displaying once more the fact that Case 0sp is source of greater oscillation in the pump at low flow. As with the pressure oscillations in the suction pipe, the oscillation gets smaller with increasing flow rate.

Summary of study 2: Effect of the addition of 1 and 2 splitters per impeller passage

As a conclusion, the study focuses on the influence of added splitter blades in the flow passages of a very low specific speed impeller. The main conclusion on the integral results is that the head is enhanced by splitter blades, the BEP is displaced to higher

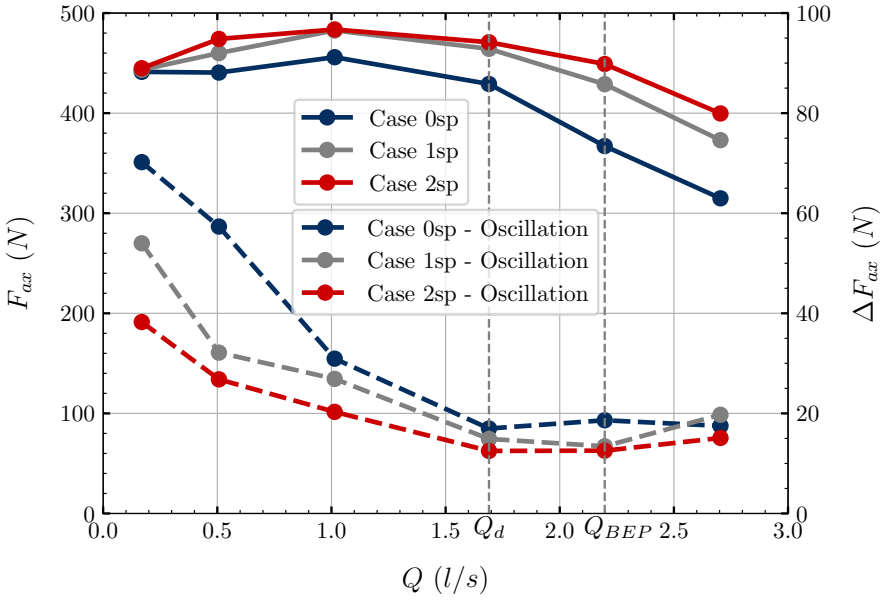

Figure 4.36: Axial force and peak-to-peak force difference.

flow rates and the head curve stability is negatively influenced by the introduction of splitter blades. The maximum efficiency is almost unaffected by the introduction of splitters. The enhanced pump performance is the consequence of an improved slip factor at the outlet of the impeller thanks to the presence of the splitter. The flow is more blade congruent. The analysis of the losses in each domain of the pump leads to the conclusion that the introduction of splitter does slightly improve the flow in the impeller and sidewall gaps. The improved flow in the impeller leads to a higher absolute velocity at the impeller outlet which balances the benefits cited above with additional wall friction losses in the volute. Nonetheless, the splitter blades have an overall beneficial effect as they enhance performances while not affecting the efficiency. The case with 2 splitter blades also displays advantages over the case with 1 splitter and suggests that increasing the number of splitters might be beneficial as skin friction and shock losses in the impeller are minimal, as displayed by the loss analysis. The streamlines in the impeller show the eddies that develop on the pressure side of the blade if splitters are not present. The presence of splitter greatly helps in breaking those eddies. No major eddy is present in the flow even at 10% of the design point for Case 2sp. The eddies present in the impeller Case 0sp at low flow directly influence the pressure and forces pulsations in the pump at low flow, due to the jet-wake flow pattern. At higher flow, when the streamlines are healthier, the pressure and force oscillations are similar for all cases. Splitters blades show advantages mainly at low flow for transient effects.

4.3. Partial conclusion about splitter blades

The part of the thesis focused on the impeller design is summarized here. Two studies have been presented, both heavily focused on splitter blades. In term of impeller design, the constant of the two studies is the meridional section shape and the 4 main blades. The variables being either the shape of the splitters (study 1) or number of splitters (study 2). Another difference between the two studies is the casing used. Casings used in both

studies are oversized, meaning the Best Efficiency Point is reached at a higher flow rate than the design point.

The reference impeller has 4 main blades. Any splitter design tested had qualitatively the same impact on the head:

- Increase of head at all flow rates.
- Increase in instability (by a flattening of the head curve or the introduction of instability)

These impacts have been quantified in the first study. For a given design, with the objective of reaching a high head, the designer should use long splitter blades with a high outlet blade angle as seen with Case 4 in study 1, which gave a head 11% higher than the case without splitters. The stability of the curve is negatively impacted. A designer who favours stability and needs to use a low specific speed pump should in a first time avoid the use of splitter blades. If, for various constraints, the head needs to be raised without the possibility to increase the diameter, the designer should investigate which of the following options is advantageous:

- No splitters, raise the blade outlet angles.
- Addition of a splitter, low outlet blade angles.

The second study, with the addition of the second splitter in the impeller passage confirmed that the addition of yet another splitter is beneficial for the head. Most importantly, a common finding from both studies and all tested designs, is that the efficiency is barely affected by the introduction of splitters. This makes a low specific speed impeller with splitter more efficient with the same head performances.

For example, let us take that for a given diameter $d_{2,initial}$, a design with splitters provides a 11% head raise at the design point (as observed in the performed studies). Using the pump affinity laws for constant rotor speed, a new diameter $d_{2,new}$ for the splitters design could be equal to $0.95 \cdot d_{2,initial}$ to give the same head as the case with no splitters. Thanks to the reduced diameter, the disk friction losses would diminish. Disk friction losses being proportional to the diameter to the power of five, disk friction losses would be reduced by about $1 - 0.95^5 = 23\%$. With reduced friction losses, the efficiency of the smaller, scaled pump would be raised.

The analysis of the streamlines in the impellers at all flow rates showed that the splitters blades indeed break the eddies that develop in the impeller passage. The effect is stronger at low flow rates. This is transcribed in the flow transient, where at low flow, impellers with splitters present lower pressure pulsations and hydraulic forces oscillations thanks to an improved impeller flow.

5. Results: Volute throat area study

This chapter is focused on the volute component and has two objectives. The first is related to the recent state-of-art (Juckelandt, 2016 [16]) which revealed that when using RANS models to simulate low specific speed pumps, the wall function approach overestimates the head and the efficiency, especially at overload. The first part of the chapter is focused on validating this statement by comparing the influence of different wall-treatment methods on the pump performances and validating the statements made by the author. The second objective is to evaluate the influence of the volute throat area on the pump characteristics. Three volutes of different sizes are computed numerically. After finding benefits from smaller and larger volute on the flow, a different volute design is proposed to deliver higher performance at all flow rates.

5.1. Volute design

The pump, on which computations are performed in this section, has a specific speed $n_s = 32$. The impeller used is the same as previous studies. The design is presented in section impeller design. The volute in this section is the design parameter, particularly the volute throat area. Three volutes are designed, named V_1, V_2 and V_3. From design V_1 to V_3, the throat area A_{vs} of each volute is increased. Specifically, different ratios A_{vs}/A_{II} are obtained by changing the input flow rate for the specific speed. The parameter A_{II} is related to the outlet of the impeller, see equation 5.1.

$$A_{II} = \pi d_2 b_2 sin(\beta_{2B}) \tag{5.1}$$

By changing the input flow rates as Q_d, $2Q_d$ and $3Q_d$, the specific speed of the pump is artificially changed and a new ratio A_{vs}/A_{II} is obtained based on figure 5.1. In this figure, the grey area represents the recommended ratio A_{vs}/A_{II} as a function of n_s for optimal efficiency. The newly obtained volute throat areas are marked A_{vs1}, A_{vs2} and A_{vs3} for designs V_1, V_2 and V_3. The pump parameters and volute throat area are shown in table 5.1.

Table 5.1: Pump parameters.

Designation	Symbol	Value	Units
Rotor speed	N	1450	RPM
Design head	H_d	32	m
Design flow rate	Q_d	0.0069	$m^3 \cdot s^{-1}$
Specific speed	$n_s = 3.65N\frac{Q_d^{0.5}}{H_d^{0.75}}$	32	-
Impeller outlet diameter	d_2	320	mm
Impeller outlet width	b_2	6	mm
Impeller outlet blade angle	β_{2B}	25	deg
Main Blade number	Z	4	-
Volute throat area 1	A_{vs_1}	496	mm^2
Volute throat area 2	A_{vs_2}	670	mm^2
Volute throat area 3	A_{vs_3}	806	mm^2

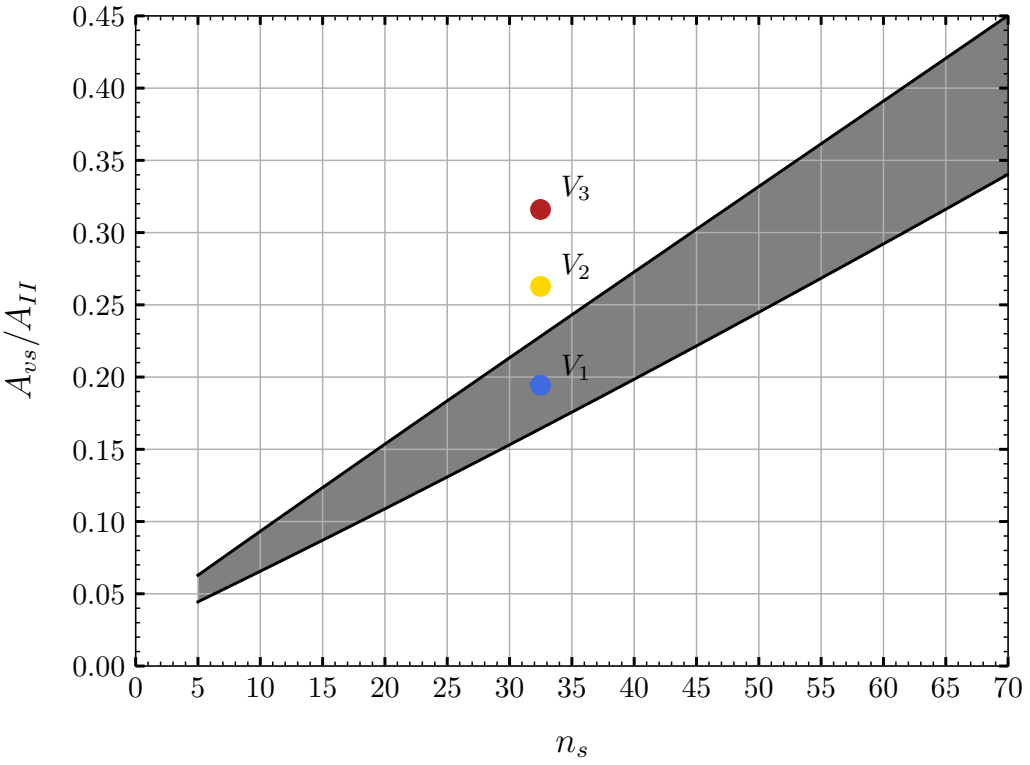

Figure 5.1: Volute throat area ratio vs. specific speed..

The volute development is constructed based on the classic rule of the conservation of angular momentum. The other volute parameters, such as the volute inlet width, tongue position and diameter, are calculated from Gulich recommendations [1], and kept constant for the three designs, so that only volute area development and the volute throat area are changed between the three designs. The specific cross section shape of each volute is constructed with the same in-house code used in section impeller design developed by Pochylý and Stejskal [47, 48], that also has the ability to design volutes. The starting point is the construction, for each volute, of the volute throat area. A Bezier surfaces with control points is used for this purpose, figure 5.2.

The second step is the construction of several sections along the circumference of the volute. Figure 5.3 represents ten curves, the sections of a volute. This is the final output of the in-house software. The given curves serve as an input for a CAD software where a simple sweep over the cross-sections creates the the spiral part of the volute. The diffuser is constructed for each design with the same parameter for consistency and proper comparison of the designs. The outlet surface of the volute has the same diameter and position as the original BETA14 pump.

Figure 5.4 presents a cross-section of the different components of the pump, also showing the sections of the 3 volutes and their size difference.

5.2. Mesh and CFD specification

The pump is modelled with a mesh adopting the Low-Reynolds number method (LR) to resolve the boundary layer, and a mesh modelling the boundary layer with the wall

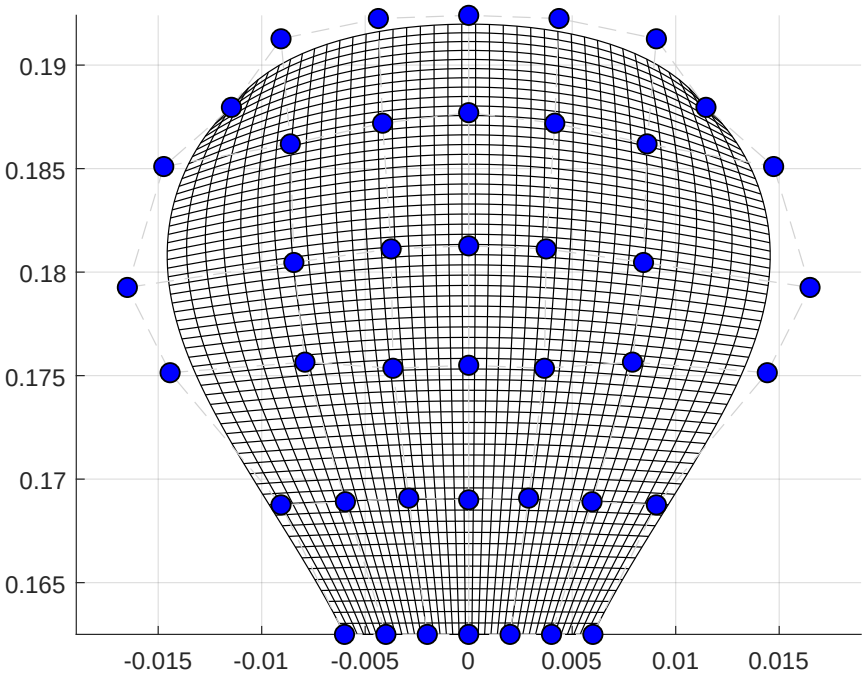

Figure 5.2: Volute design with Bezier surface.

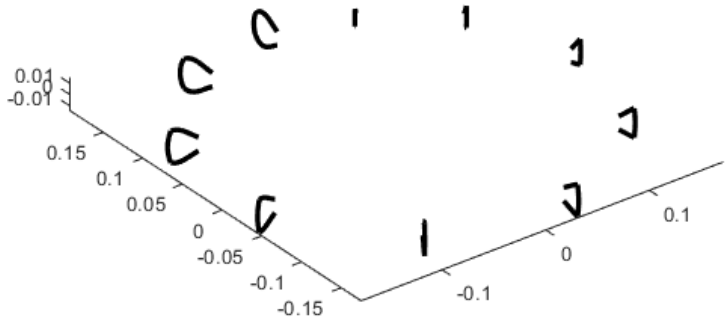

Figure 5.3: Volute sections as output of in-house code.

function approach (WF). For a given wall treatment method, only the volute geometry and mesh are changed. With 3 volute geometries (V_1, V_2, V_3) and 2 different wall treatment methods (WF, LR), a total of 6 cases are made, and noted $V_{1,WF}$, $V_{1,LR}$, $V_{2,WF}$, $V_{2,LR}$, $V_{3,WF}$, $V_{3,LR}$.

The meshes of the different fluid domains are created using the pre-processor `ANSYS-ICEM`, except for the impeller, where `ANSYS-TurboGrid` is used. A mesh sensitivity analysis is performed for the case $V_{1,LR}$. The wall requirement respects the condition $y^+ \leq 1$ almost at all surfaces, except at the trailing edge of the impeller blades, where flow separation is obvious. Figure 5.6 presents the results of y^+ for the chosen mesh where the sidewall gaps have been excluded for visualization clarity. During the mesh convergence analysis, the first cell height is kept constant not to affect the wall treatment, and the core mesh is uniformly changed in the the domains. The torque τ, head H and hydraulic efficiency η are evaluated, and the results are shown in Figure 5.5. The final mesh has a total of 16.6 million hexahedral cells, and can be fully seen in Figure 5.7.

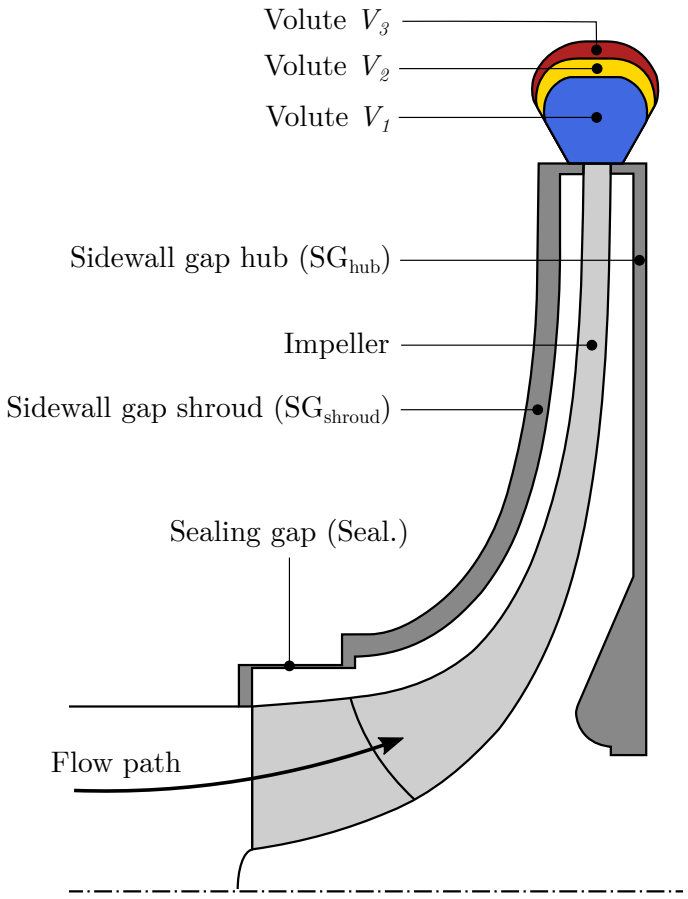

Figure 5.4: Section of fluid domains.

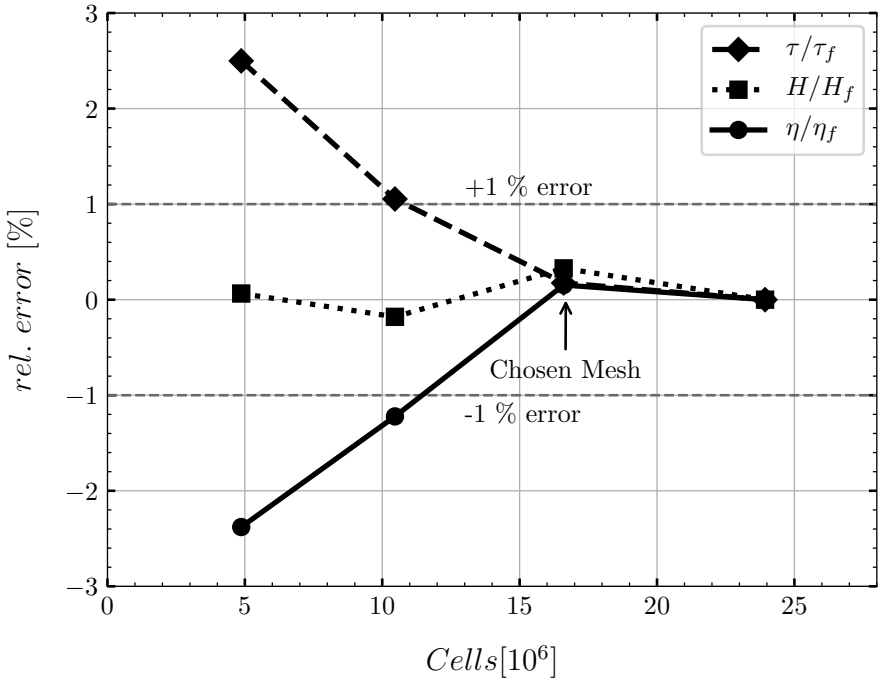

Figure 5.5: Mesh convergence analysis.

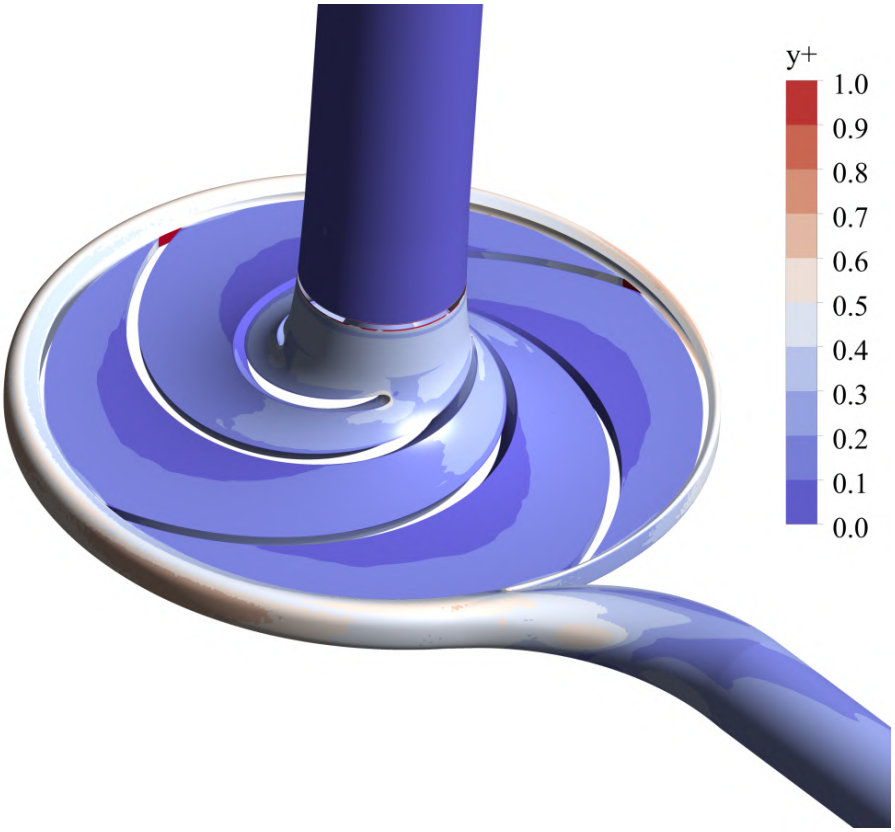

Figure 5.6: View of y^+ for the chosen grid for Case $V_{1,LR}$.

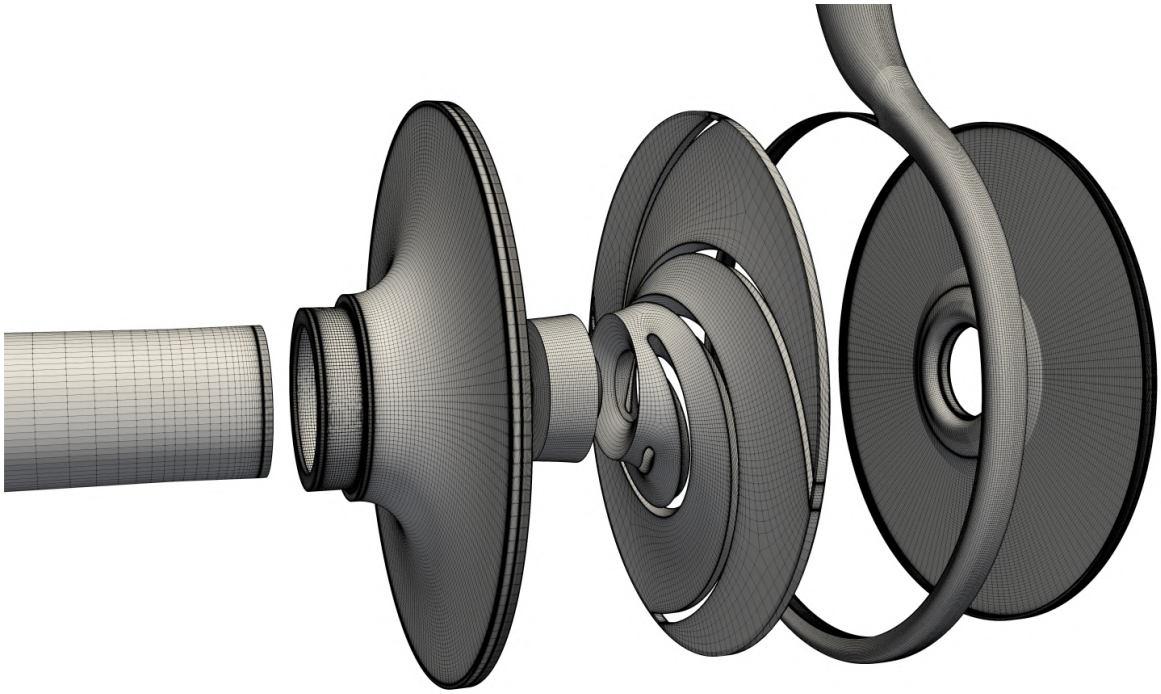

Figure 5.7: View of the chosen grid for Case $V_{1,LR}$.

For meshes using the WF method, only the first cell height is changed, and is about 140 times bigger to achieve a y^+ between 30 and 300 everywhere. The case $V_{1,WF}$ has 4.2

millions cells, 4 times less than the case using the LR approach. The difference between the two meshes can be se in figure 5.8, which shows a section of the volute mesh.

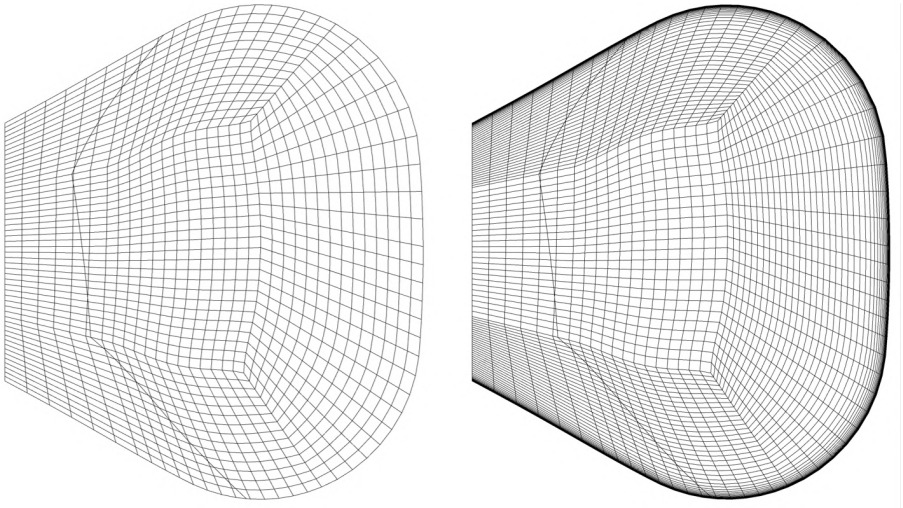

Figure 5.8: Section of volute mesh for case $V_{1,WF}$ (left) and case $V_{1,LR}$ (right).

The total number of transient computations performed is 36 (6 flow rates, 3 different volute, 2 wall treatment methods).

5.3. Part 1: Wall functions vs. Low-Reynolds number approach for wall treatment

A comparison between the two wall treatment methods is performed. The difference of performance prediction for both methods is evaluated. For a quantity ϕ, the calculation is as follows:

$$\Delta_\phi = \frac{\phi_{WF} - \phi_{LR}}{\phi_{LR}} \cdot 100\% \tag{5.2}$$

The difference Δ_ϕ is evaluated for the head and the hydraulic efficiency over the whole operating range for the 3 different volutes. Figure 5.9 presents the results.

At partload, the difference Δ_ϕ is reasonably low for all designs and variables. The difference between the two wall-treatment methods gives similar results. At the design point, the error increases for V_1, while staying low for the other cases. At high-flow, Δ_ϕ dramatically rises to more than 20% for both evaluated variables. The difference increases with the flow rate for volutes V_2 and V_3 as well and the same behaviour is observed, but is comparatively low with an error of about 5% and 7% for V_2 and V_3 respectively at the maximum flow rate. The value of Δ_ϕ is always positive for the head coefficient and the efficiency, indicating that the WF approach over-predicts the performances comparing to the LR approach.

The head and efficiency are plotted in figures 5.10, 5.11 and 5.12 for cases V_1, V_2 and V_3 respectively. For the first case V_1, the BEP is clearly displaced to higher flow rates with the WF approach. The same behaviour is present for other volute designs at a lower scale, and the performance prediction for both wall treatments is closer.

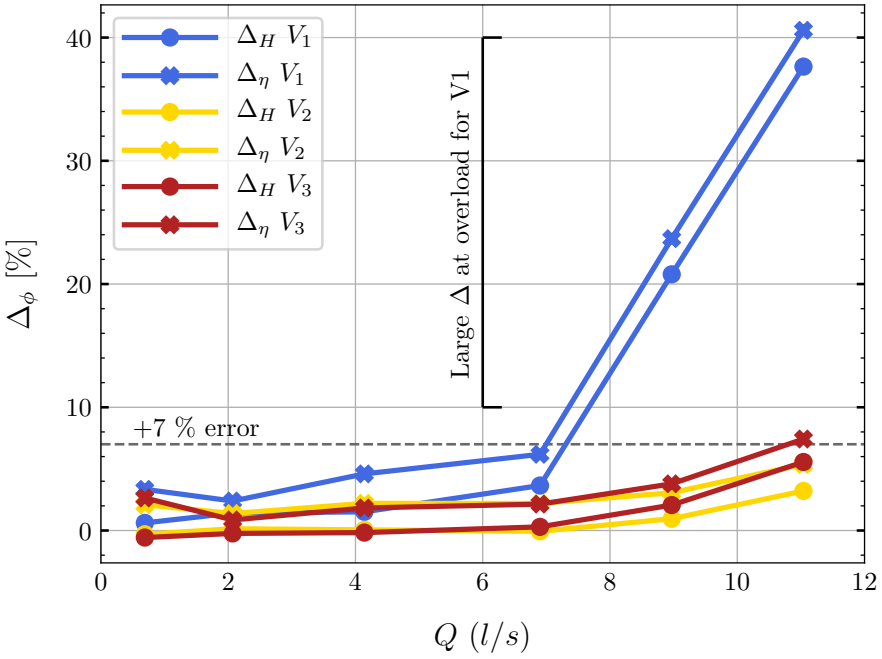

Figure 5.9: Difference Δ_ϕ for cases V_1, V_2 and V_3.

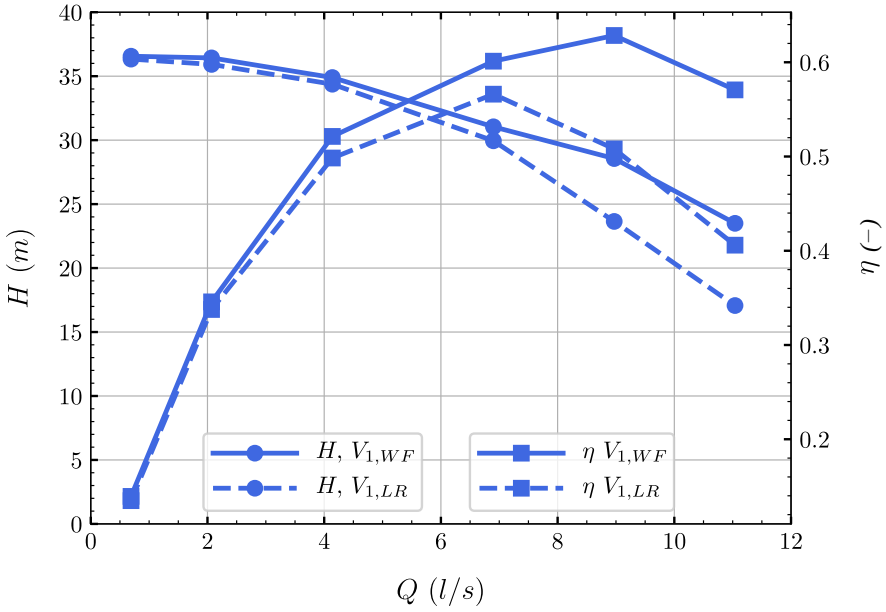

Figure 5.10: Head and efficiency of the cases $V_{1,WF}$ and $V_{1,LR}$.

To understand the reason behind the large discrepancies at high-flow, the power losses $P_{L,i}$ in each domain i are computed. The power losses in the suction pipe are neglected.

$$P_{L,i} = \sum P_{\tau,i} + P_{in/out,i} \tag{5.3}$$

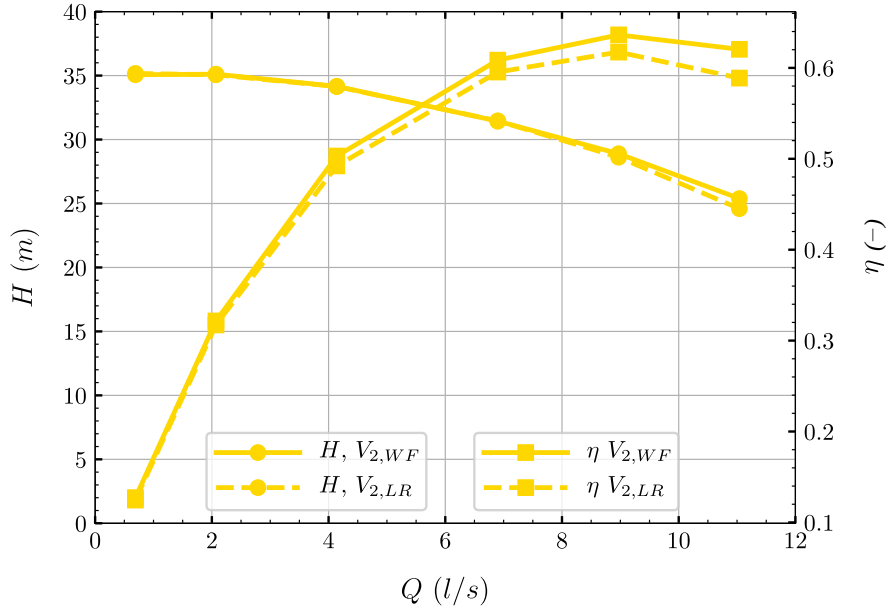

Figure 5.11: Head and efficiency of the cases $V_{2,WF}$ and $V_{2,LR}$.

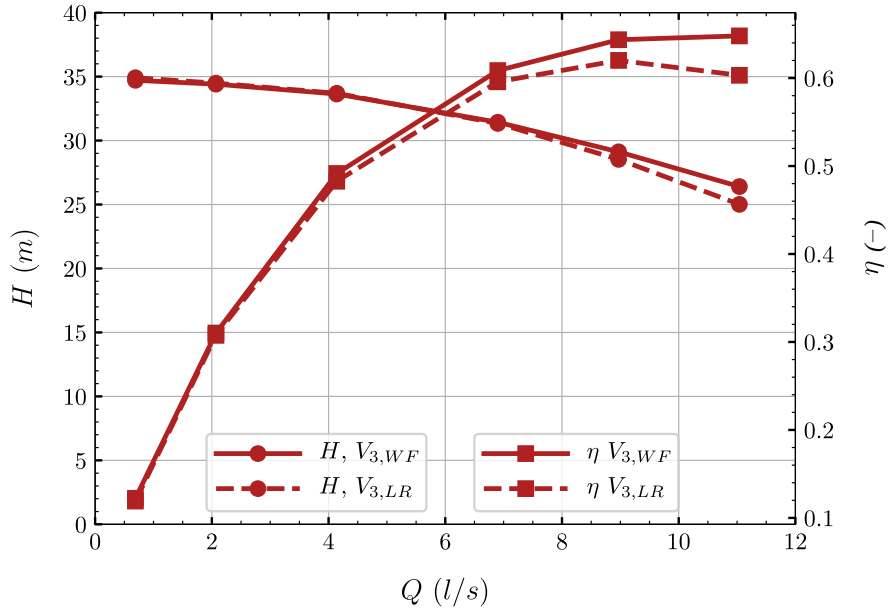

Figure 5.12: Head and efficiency of the cases $V_{3,WF}$ and $V_{3,LR}$.

$P_\tau = \omega\tau$ is the power transferred to the fluid measured at rotating walls and $P_{in/out} = \int \frac{p_T}{\rho} d\dot{m}$ measures the power entering and leaving a domain. The losses are scaled by the theoretical useful power transferred to the fluid at the design point $P_{u,d}$.

$$P_{u,d} = \rho g H_d Q_d \tag{5.4}$$

The results are presented at high-flow, at $Q/Q_d = 1.6$ in figure 5.13. For the three designs, the losses are usually slightly higher in every domain for LR cases. However, the main differences between the two wall-treatment methods WF and LR is located in the volute where losses using the LR methods are significantly higher than when using the

WF methods. This is true for case V_1 in particular. This loss analysis confirms that the large Δ_ϕ observed in the head and hydraulic efficiency at high-flow is due to erroneous prediction of volute losses. According to Juckelandt [8], this difference is explained by a detachment zone downstream the tongue not captured when using wall-functions. Such a detachment zone can be identified by plotting countours of the turbulence kinetic energy (TKE), see figure 5.14. Clearly, high TKE is observed downstream the tongue. For the three volutes, the TKE is larger for LR computation compared to the computations using the WF approach, especially for design V_1.

This confirms that the behaviour observed by Juckelandt [8] is also observed here. The WF erroneous predictions seem to be linked to the flow physics. Enlarging the throat area reduces the velocity downstream the tongue. As a consequence, the zone of large TKE, where detachment also occurs is reduced and the difference between performance predictions is reduced. Essentially, using an oversized volute, such as for cases V_2 and V_3 displaces the BEP to higher flow rates but is beneficial for the flow at high load.

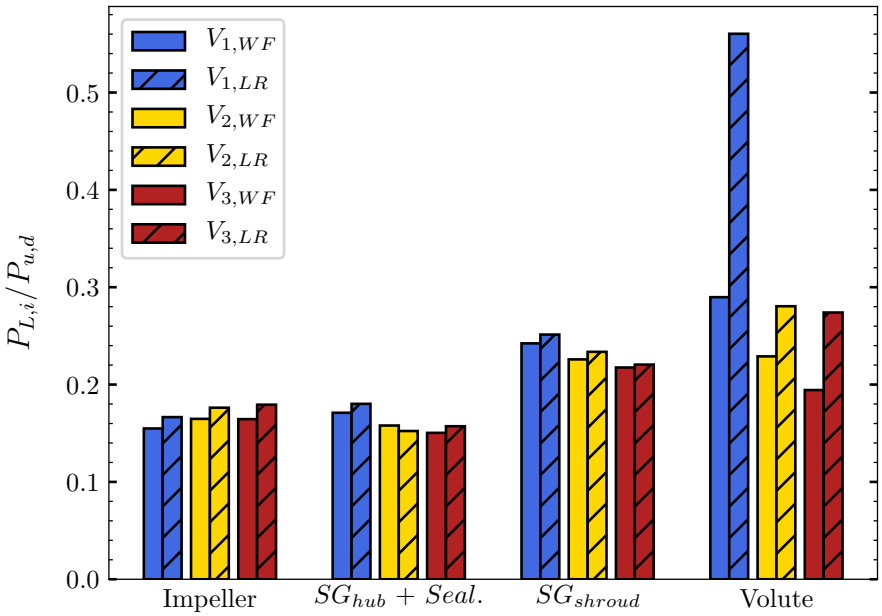

Figure 5.13: Relative losses per domain and per case as per equation 5.3 at $Q/Q_d = 1.6$.

5.4. Part 2: Volute throat area influence on the pump performance

In this section, only the results obtained with the Low-Reynolds number approach are discussed. The head and efficiency for the 3 cases are presented in Figures 5.15 and 5.16. As the volute dimension increases, the head at low-flow diminishes, and the head at high-flow increases, leading to a flattening of the head curve. For bigger volutes, the efficiency is slightly lower at low-flow and the BEP is displaced to higher flow rates. Although the expected behaviour is verified, it is not linear between the three volutes, as $V_{2,LR}$ and $V_{3,LR}$ have similar predicted head and hydraulic efficiency with a large difference comparing to $V_{1,LR}$. The volute enlargement is beneficial at the design point and at high-flow, where both the head and the efficiency are improved. The physics for such

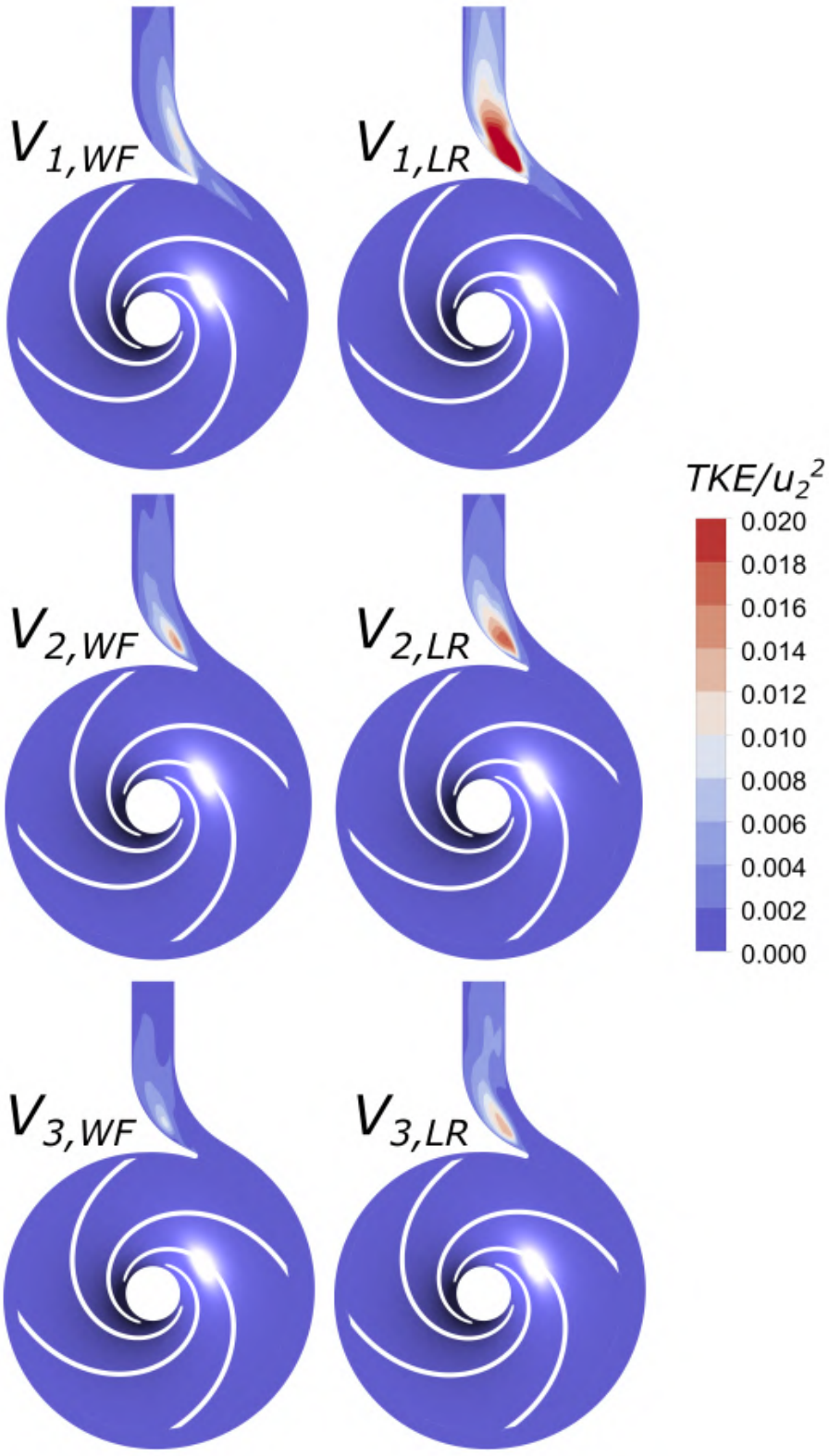

Figure 5.14: Scaled TKE for all cases at $Q/Q_d = 1.6$.

performance improvement were discussed in the previous section: a larger volute, in particular a large volute throat area, reduces the TKE downstream the tongue, as it can be seen by looking at the right side of the Figure 5.14.

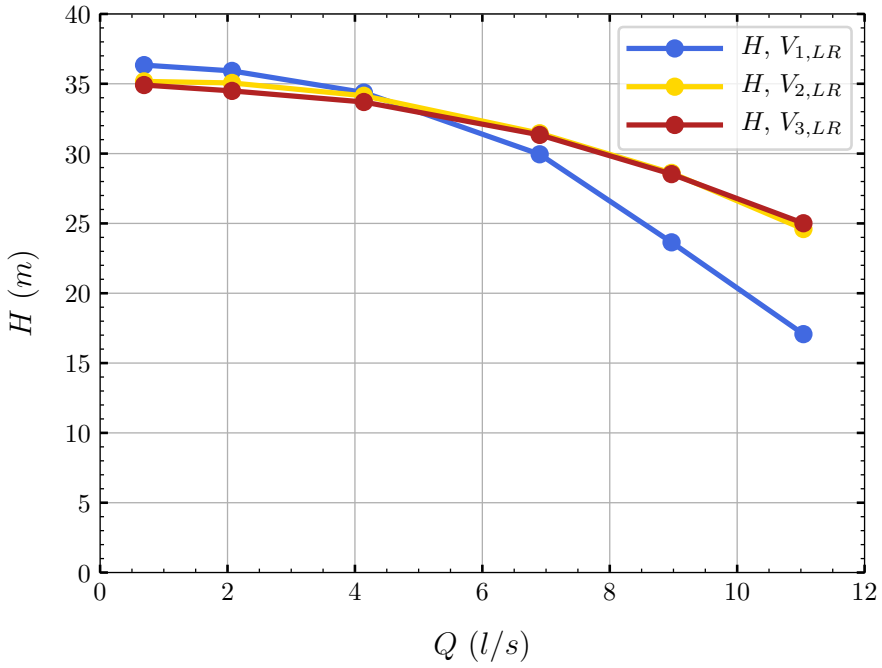

Figure 5.15: Head calculated by CFD for Low-Reynolds number meshes.

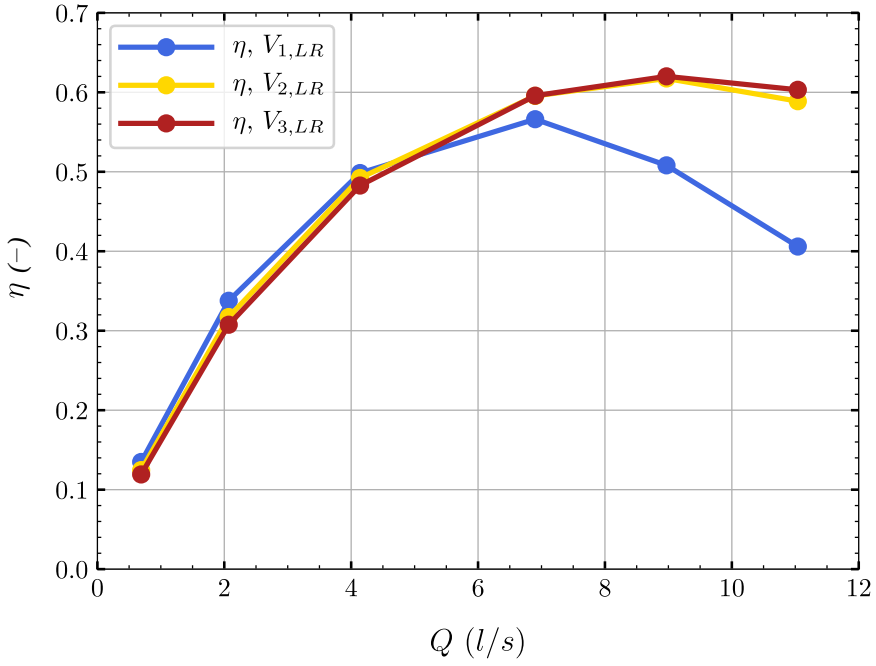

Figure 5.16: Efficiency calculated by CFD for Low-Reynolds number meshes.

At low-flow, the head is seen to flatten when increasing the volute throat area. The flattening of the head curve indicates more pump losses when a bigger volute is used. When using an impeller with a higher number of blades, higher blade outlet angle or higher outlet width, the head curve might be unstable. The study of the flow close to shut-off is thus of interest.

The losses in each of the regions at low-flow, at $Q/Q_d = 0.1$, are plotted in Figure 5.17. It is seen that the losses are higher for pumps with a bigger volute design in all domains, except in the volute, where losses are the lowest.

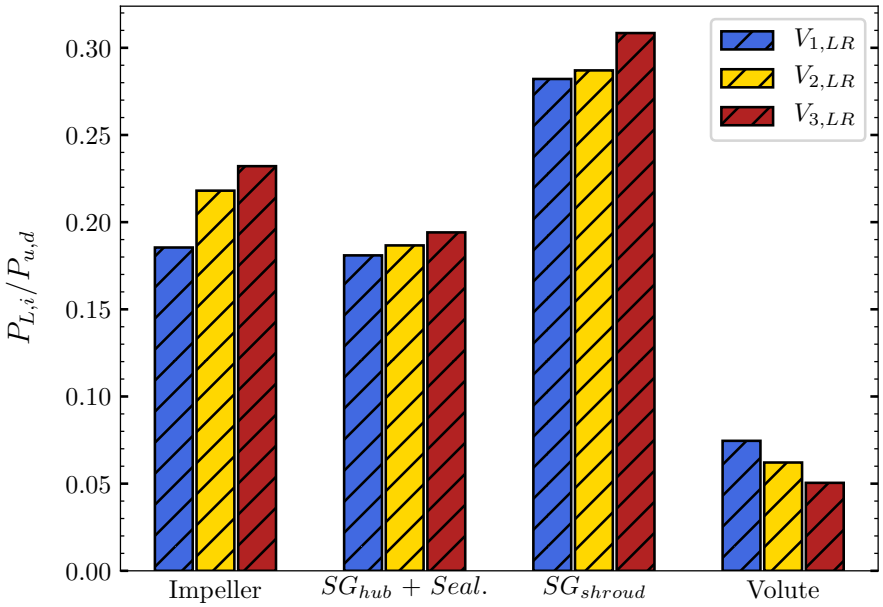

Figure 5.17: Relative losses per domain per case as per equation 5.3 at $Q/Q_d = 0.1$.

To investigate these losses, the flow transfer among several planes is computed and visualized in Figure 5.18. The Figure describes the time-averaged normal velocity v_n at three planes. The velocity is scaled by the averaged meridional inlet velocity at the impeller suction v_{m1}. The three planes are located in the side wall gap (hub side), at the outlet of the impeller and at the sidewall gap (shroud side). The velocity v_n is positive when the fluid flows into the volute, as depicted by an arrow and plus sign in geometry scheme of Figure 5.18, and negative when it flows out. For the sidewall gap (hub side), between 0 and 90 degrees, the exchange is at equilibrium, and v_n is close to zero. Between 90 and 250, there is a net flow from the sidewall gap into the volute. Between 250 and 360 degrees, the flow exits the volute at large speed. The last portion of the volute has a higher pressure, and drives the flow back to the suction. Additionally, with the impeller blade approaching the tongue, the flow is pushed into the gaps, leaving the volute. The averaged velocity v_n is negative, as the fluid flows back to the inlet of the impeller.

For the impeller, the process is cyclic, governed by blade passage. The large peak every 90 degrees shows that the flow exits the impeller on the pressure side. A backflow is clearly visible right after. Finally, there is no net flow exchange from the middle of the impeller to the suction side of the blade.

For the sidewall gap (shroud side), the averaged total flow is zero as it is a closed computational domain. From 0 to 180 degrees, the fluid flows from the gap into the volute. The flow is then close to 0 until about 250 degrees, and the fluid again exits the volute at high speed between 250 and 360 degrees.

The flow patterns are very similar for all volutes, but the exchange is stronger with bigger volute. The value of $|v_n|$ is higher for $V_{3,LR}$. In other words, the curve for $V_{3,LR}$ is always higher in the positive velocity region and always lower in the negative region.

A bigger volute thus leads to a higher flow exchange between domains, and consequently higher losses, leading to a flatter head at low-flow.

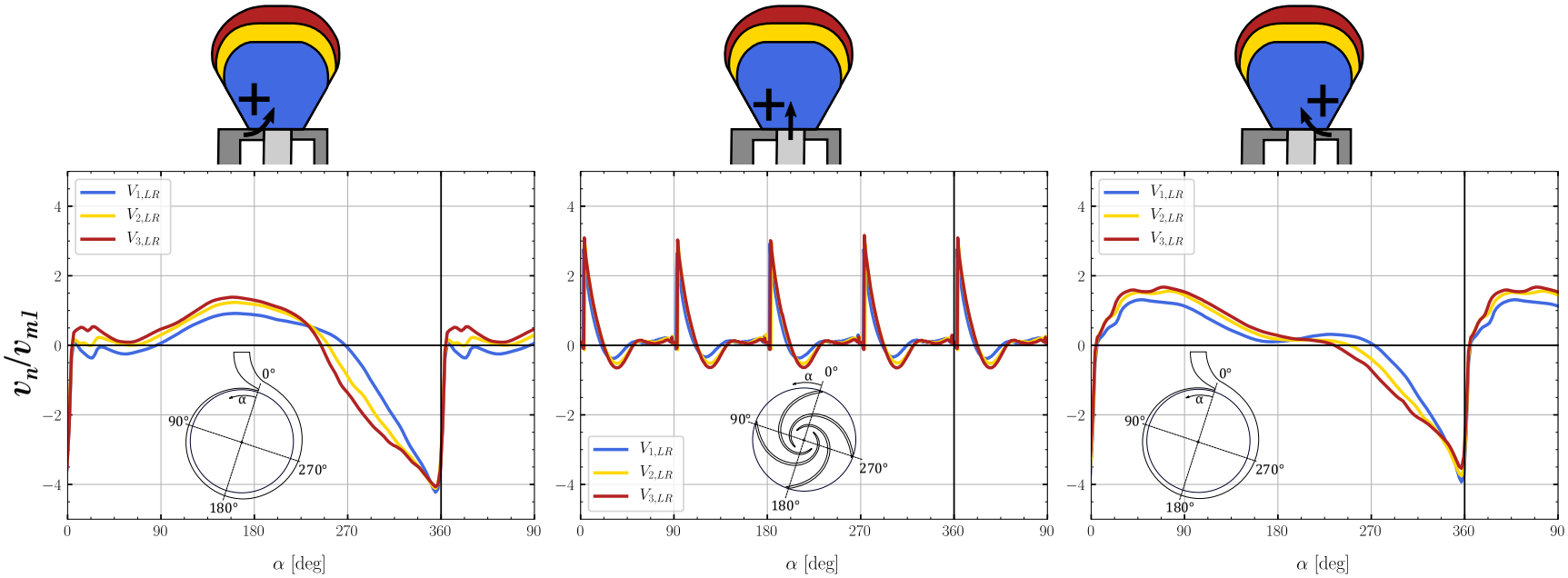

Figure 5.18: Illustrated circulation at different sections of the pump at $Q/Q_d = 0.1$.

5.5. Conclusion about volute throat area

5.5.1. New volute design

Low-flow and high-flow phenomena have been investigated for different volute sizes at low specific speed. Two statements can be made about the analysis:

- At low flow, the small volute V_1 presents better performances due to a limited exchange of momentum between domains, thanks to a smaller cross section. This takes place in the spiral part of the volute.
- At high flow, the large volute V_3 presents better performances due a large throat area that allows the flow not to be choked. This takes place at the throat of the volute.

Because these two mechanisms occur in distinct parts of the volute, it is possible to design a volute benefiting from both. A new design uses the cross-section of the volute V_1 for the major part of the circumference, and rapidly increases the area close to the tongue to obtain the throat area of volute V_3. This new design is non-conventional in the way that it does not respect the design rule of conservation of angular momentum, governing the evolution of the volute cross-section over the circumference as seen in Figure 5.19. Figure 5.20 shows the difference between volute V_1 and the new non-conventional design.

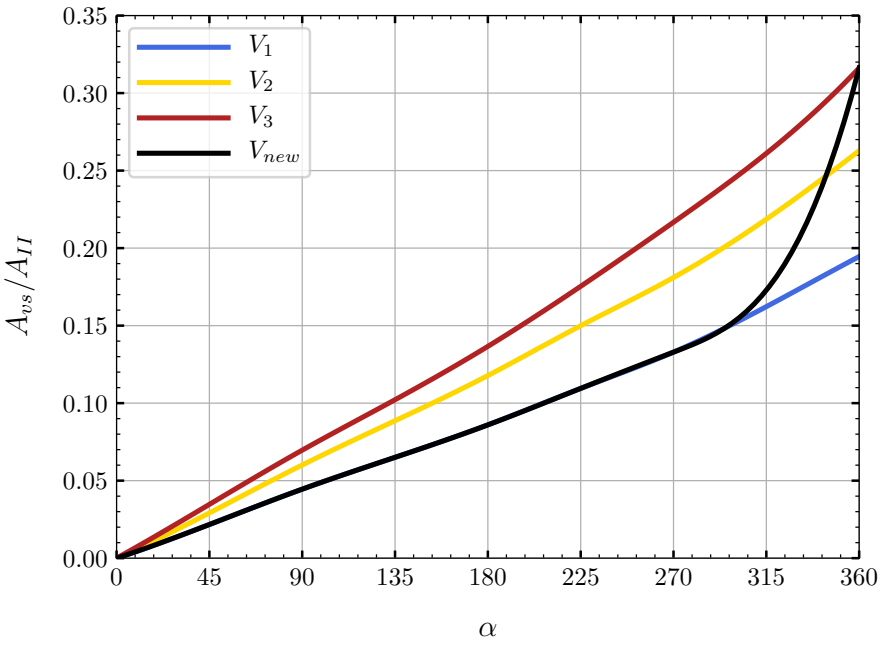

Figure 5.19: Volute cross-section area development along the circumference.

The new volute design V_{new} is evaluated by means of CFD simulation and compared with the designs V_1 and V_3 in figures 5.21 and 5.22.

From the figures, it is clear that the new design V_{new} offers better performances at low and high flow. The head and efficiency at low flow match the performances of volute V_1, while they match the performances of volute V_3 at high flow. The new design is advantageous and confirms that the flow phenomena in the spiral parts and downstream

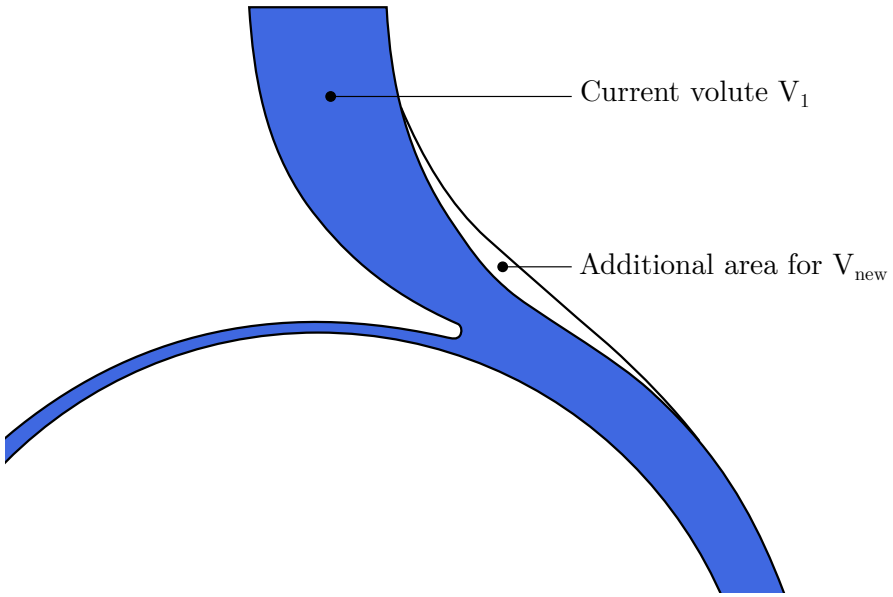

Figure 5.20: New volute section compared with volute V_1.

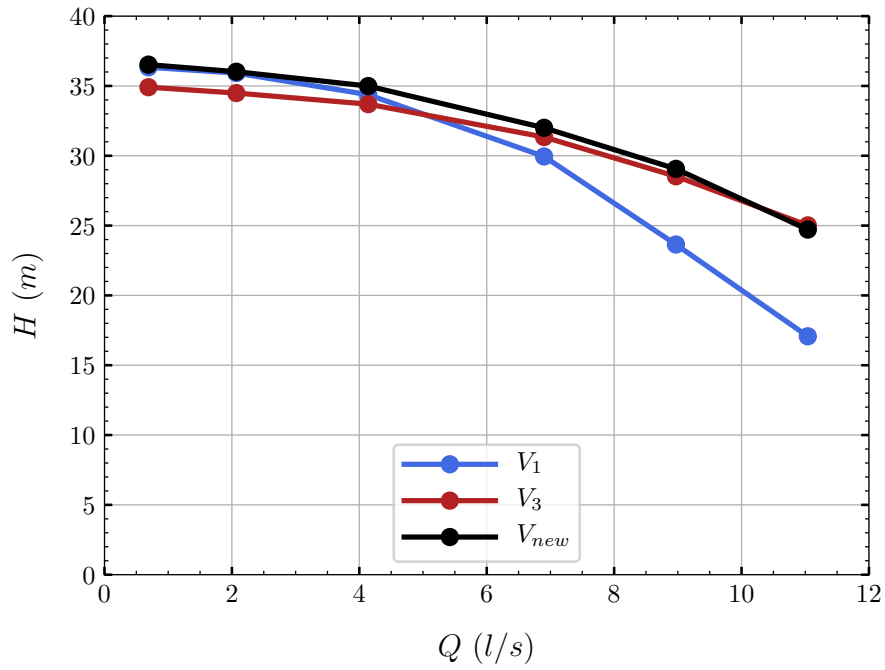

Figure 5.21: Pump head with the new volute design compared with V_1 and V_3.

the tongue are for the most part independent from one another. This volute design has been manufactured and used in the experimental part of Study 2: Effect of the addition of 1 and 2 splitters per impeller passage.

5.5.2. Closure

The flow in a low specific speed pump of $n_s = 32$ has been computed by means of CFD. The influence of the volute throat area is investigated using 3 designs. In the first part, it is seen that using the wall-function approach leads to large differences in

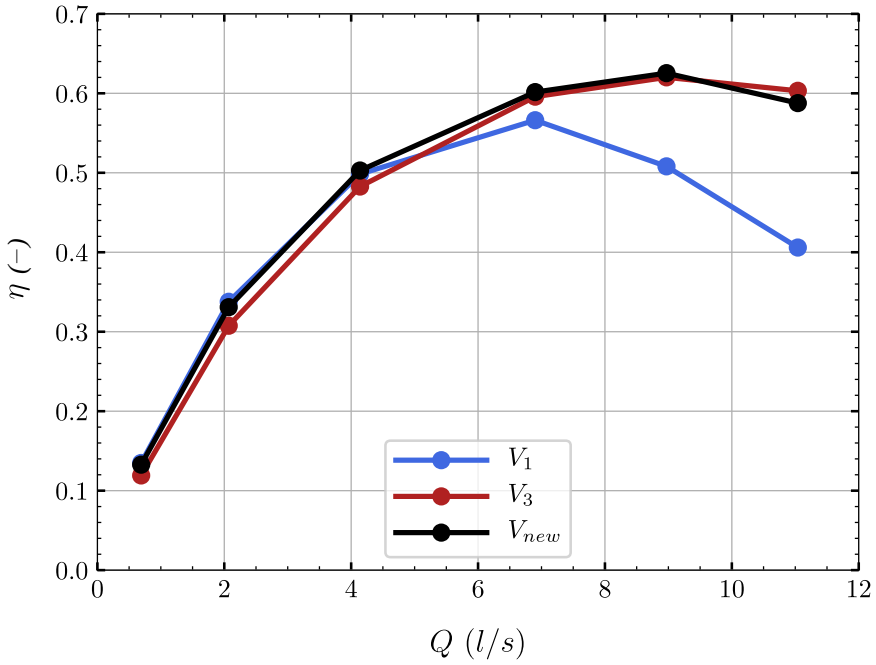

Figure 5.22: Pump efficiency with the new volute design compared with V_1 and V_3.

the predicted pump performances as compared to the low-Reynolds number approach. A forty percent difference is observed at $Q/Q_d = 1.6$ for the case V_1. The difference is due to a wrong prediction of losses downstream the volute tongue, where a zone of large turbulence kinetic energy is present. This mixing zone lowers in intensity as the volute throat area is increased, and so does the difference in the prediction of performances between the two wall-modeling approaches.

In the second part, it is seen that increasing the volute throat area increases the performance of the pump at the best efficiency point and at high-flow. The reason for such an improvement is in the reduction of turbulence kinetic energy downstream the tongue with a throat area enlargement. Besides, the head decreases at low-flow with larger volutes and the risk of instability rises. The flow close to the shut-off point ($Q/Q_d = 0.1$) is investigated. It reveals that a bigger volute leads to higher losses in all domains, except in the volute. The study of the flow exchange between domains (volute, impeller, sidewall gaps) shows that a bigger volute leads to a larger exchange of flow between domains, and so higher mixing losses and friction losses in the case of the sidewall gaps.

Because the regions in which the two unfavorable flow phenomena exist are distinct, a new design is tested avoiding both flaws. The new design is non-conventional, as it does not respect the traditional rule of conservation of angular momentum to describe the volute cross-section. The new design presents high performances both at low and high flow rate. An experiment on a scaled hydraulic model was performed to confirm the observed behaviour.

6. Conclusions and perspectives

6.1. Conclusions

The thesis aims to contribute to the improvement of hydraulic performances of a low-specific speed pump of $n_s = 32$. CFD tools have been used in the presented work to predict and analyze the flow in low-specific speed pumps. Experiments have been done with three impellers to validate part of the obtained numerical results. The main outcome of the thesis are the following:

- **Numerical simulations:** The recent state of art concerning the simulations of low specific speed pumps revealed discrepancies between predicted numerical performances and experiments. Juckelandt [16] suggested that the wall-functions method is unable to predict flow separation downstream the tongue at overload, source of major losses. The use of the low-Reynolds number method would tackle this problem for a greater computational costs. This assessment was verified on the pump geometry used in this dissertation.

- **Impeller:** A careful review of the state of art revealed that the use of splitter blades is a typical solution to tackle problems of low specific speed pumps. Due to the lack of studies present at such a low specific speed, the first part of the results are focused on the use of the splitter blade technology to improve the flow of low specific speed pumps. The conclusion stated that a head raise from 10 to 15% can be expected thanks to splitter blades without impairing the efficiency. The stability of the head curve however is always negatively affected, even with splitters with lower outlet blade angles than the main blades. This statement is also true when a second splitter is added in the impeller passage. A detailed flow analysis in the pump revealed that thanks to splitter blades, the losses (relative to the shaft power) in the pump are smaller in the impeller and the sidewall gaps, but higher in the volute. The flow improvement at the outlet of the impeller leads to a flow with higher absolute velocity at the volute inlet. As a result, friction losses increase in the volute and counterbalances the improvements in other flow domains. The local eddy typically present on the pressure side of blades of low specific speed impeller cannot develop with the presence of splitters. When two additional splitters are used in the flow passage, the large eddy is not present even at 10% of the design flow rate. As a consequence, the pressure and hydraulic forces oscillations at part-load are greatly reduced with the presence of splitters.

- **Volute:** The second part of the results, focused on the volute component, reflects the importance of the throat area on the flow. Tests on three different volutes confirmed that the volute throat area is the main factor in determining the position of the best efficiency point. It was shown that a small volute has benefits at low flow (spiral section) and a bigger volute has benefits at high flow (large volute throat area). A new, unconventional design is proposed, based on these results. The characteristic of this new design is a narrow spiral section and a large volute throat area. After showing high performances at both low and high flow, the design was manufactured and tested experimentally.

- **Head curve stability:** Adding splitter blades and using large volute impair the stability of the head curve at low flow. It was stated that the added flow exchange between the domains (with splitters and large volute) is responsible for pressure dissipation at low flow, eventually leading to instability. The use of the said unconventional volute design limits this low-flow recirculation. The narrow spiral section limits the adverse pressure gradient driving the fluid back to the impeller and to the sidewall gaps.

The results of the thesis have been supported with a presentation at the conference Experimental Fluid Mechanics 2019, at the online conference IAHR 2020 with a publication [51] and in the journal Energies [52]. An experimental campaign has been performed to validate part of the obtained results. Three different impellers were tested and an excellent agreement with the numerical simulations were obtained for each of them. The results are presumably valid for low specific speed pumps with a specific speed below $n_s = 75$.

6.2. A few design recommendations

Based on the and experience accumulated during the work on this thesis, a few design recommendations can be made aimed to the hydraulic designer in need of a low specific speed pump. The main impeller parameters, i.e. outer diameter d_2, outlet width b_2 and outlet blade angle β_{2B} are at the discretion of the hydraulic designer as their influence on the pump characteristics is similar as with more classic specific speed pumps.

For a given design, a strategy to obtain a pump with a greater efficiency and head is to raise the specific speed. The Best Efficiency Point is displaced towards higher flow rates, but the efficiency at the design point is also raised. This was done in two ways in this thesis:

- An increase of the volute throat area.
- The addition of splitter blades.

Both suggestions will have a negative impact on the pump stability. The negative impact can be totally controlled in the volute with the unconventional design proposed: the use of a spiral section fitting the design specific speed coupled with a larger throat area (1.5 to 2 times the design throat area). This strategy seems to not have drawbacks as both the efficiency and head are raised without impairing the pump stability. In the impeller, the addition of splitters will raise the head without impairing the efficiency but inevitably impair the stability of the head. The pressure and hydraulic force pulsations are also reduced. Based on this trade-off, the designer can decide if no splitters, or the use of one splitter or more per passage is most beneficial for its own case.

6.3. Perspectives

Splitter blades offer a clear benefit in the design of low specific speed pumps as they increase the head and have a small to no effect on the efficiency, even sometimes raising it also. In this thesis, at $n_s = 32$, impellers with 4, 8 (4 main blades, 4 long splitters) and

12 blades (4 main blades, 4 long splitters, 4 short splitters) were tested and performance improvements were shown with each new addition of splitters. The number of splitters can be raised until a performance drop in either head, or efficiency is observed. Up to 24 blades (4 main blades and 20 splitters) were proven to be beneficial for both head and efficiency at $n_s = 25$ [24].

The importance of the volute, and the importance of the throat area especially is maximal at low specific speed. We saw that a combination of a tight spiral and a large throat area is beneficial for allowing high performance in a high range of flow rates. Due to the importance of volute friction, a concentric volute with a large cross-section is beneficial from an efficiency and head point of view, although the stability of the head-curve is impacted.

To reduce the disk friction, the use of semi-open impeller may be beneficial at low specific speed, as the disk friction losses would be reduced by a factor of 2. Additional losses and constraints would be added due to the gap between the blades and casing that needs to be small to ensure high efficiency. The axial force would greatly raise and axial force reduction system such as balance holes or back-vanes should be used.

The thesis also made use of rapid prototyping using FDM for impeller manufacturing and testing. Considering the success of the experiment, new designs can be tested rapidly and for a convenient price.

From the numerical simulations point of view, we confirmed that the simulation of the whole pump (especially including the sidewall gaps) is necessary.

Bibliography

[1] GÜLICH, Johann Friedrich. *Centrifugal Pumps*. 3. Berlin: Springer, 2014. ISBN 978-3-642-40113-8.

[2] STEPANOFF, Alexey J. *Centrifugal and Axial Flow Pumps: Theory, Design, and Application*. 2. Krieger Publishing Company, 1993. ISBN 978-0894647239.

[3] JAPIKSE, David. *Centrifugal pump design and performance*. 1. Concepts ETI, 1997. ISBN 978-0933283091.

[4] KARASSIK, Igor J., Joseph P. MESSINA, Paul COOPER and Charles C. HEALD. *Pump Handbook*. 3. Tehran: ASK Innotec, 2011. ISBN 978-0071460446.

[5] KLAS, Roman, František POCHYLÝ and Pavel RUDOLF. Analysis of novel low specific speed pump designs. *IOP Conference Series: Earth and Environmental Science*. 2014, **22**(1), 012010. DOI: 10.1088/1755-1315/22/1/012010.

[6] KLAS, Roman, František POCHYLÝ and Pavel RUDOLF. Influence of recirculation on Y-Q characteristic curve of hydrodynamic pump. *EPJ Web of Conferences*. 2016, **114**, 02054. DOI: 10.1051/epjconf/201611402054.

[7] KLAS, Roman. *Hydraulický návrh hydrodynamického stroje s vloženými lopatkami*. Brno, 2009. PhD Thesis. Brno University of Technology.

[8] JUCKELANDT, Kay and Frank-Hendrik WURM. *Applicability of Wall-Function Approach in Simulations of Turbomachines*. 2015. ISBN 978-0-7918-5664-2.

[9] WEI, Yangyang, Yang YANG, Ling ZHOU, Lei JIANG, Weidong SHI and Gaoyang HUANG. Influence of Impeller Gap Drainage Width on the Performance of Low Specific Speed Centrifugal Pump. *J. Mar. Sci. Eng.* 2021, **9**(2), 106. doi:https://doi.org/10.3390/jmse9020106

[10] ZEMANOVÁ, Lucie and Pavel RUDOLF. Flow Inside the Sidewall Gaps of Hydraulic Machines: A Review. *Energies*. 2020, **13**(24), 6617. doi:https://doi.org/10.3390/en13246617

[11] GÜLICH, Johann Friedrich. Disk friction losses of closed turbomachine impellers. *Forschung im Ingenieurwesen*. 2003, **68**, 87-95. DOI: https://doi.org/10.1007/s10010-003-0111-x.

[12] DAQIQSHIRAZI, Mohammadreza, Rouhollah TORABI, Alireza RIASI and Ahmad NOURBAKHSH. *Impeller Gap Width Effect on losses in a Water Pump; Numerical Study*. Tehran, Iran: Proceedings of the 23rd Annual International Conference on Mechanical Engineering-ISME2015, 2015.

[13] CHO, Leesang, Seawook LEE and Jinsoo CHO. Use of CFD Analyses to Predict Disk Friction Loss of Centrifugal Compressor Impellers. *Jpn. Soc. Aeronaut. Space Sci. Trans.* 2012, **55**(3), 150-156. doi:https://doi.org/10.2322/tjsass.55.150

[14] MARUZEWSKI, Pierre, Vlad HASMATUCHI, Henri-Pascal MOMBELLI, Danny BURGGRAEVE and Peter FINNEGAN. Surface Roughness Impact on Francis Turbine Performances and Prediction of Efficiency Step Up. *International Journal of Fluid Machinery and Systems*. 2009, 2(4), 353-365. doi:https://doi.org/10.5293/IJFMS.2009.2.4.353

[15] DAQIQSHIRAZI, Mohammadreza, Alireza RIASI and Ahmad NOURBAKHSH. *Numerical Study Of Flow In Side Chambers Of A Centrifugal Pump And Its Effect On Disk Friction Loss*. New Delhi, India: Proceedings of the IRF International Conference, 2014.

[16] JUCKELANDT, Kay. *Experimentelle und numerische Untersuchung der Strömungin Pumpen kleiner spezischer Drehzahl unter Berücksichtigung des Rauheitsei-nusses*. Rostock, 2016. PhD thesis. University of Rostock.

[17] NEMDILI, Ali. *Einzelverluste von Kreiselpumpen mit spezifischen Drehzahlen nq 15 ... 35 min-1*. Kaiserslautern, 2000. PhD thesis. Lehrstuhl für Strömungs- und Verdrängermaschinen, Univ.

[18] TAMM, Alberto. *Beitrag zur Bestimmung der Wirkungsgrade einer Kreiselpumpedurch theoretische, numerische und experimentelle Untersuchungen*. Darmstadt, 2003. PhD thesis. TU Darmstadt.

[19] VAN DEN BRAEMBUSSCHE, René. *Flow and Loss Mechanisms in Volutes of Centrifugal Pumps: Educational notes*. RTO-EN-AVT-143, 12, 12-1-12-26., 2006.

[20] WORSTER, R. C. and HYDRAULIC PLANT AND MACHINERY GROUP. *The Flow in Volutes and Its Effect on Centrifugal Pump Performance*. 1963, **177**(1), 843-875. DOI: https://doi.org/10.1243/PIME_PROC_1963_177_061_02.

[21] KUROKAWA, Junichi, Takeshi YAMADA and Hiroshi HIRAGA. Performance of low specific speed pumps. *Journal of Fluid Science and Technology*. 1992, **2**(1), 130-138.

[22] KAGAWA, Shusaku, Junichi KUROKAWA, Jun MATSUI and Young-Do CHOI. Performance of Very Low Specific Speed Centrifugal Pumps with Circular Casing. *Journal of Fluid Science and Technology*. 2007, **2**(1), 130-138. DOI: https://doi.org/10.1299/jfst.2.130.

[23] WO, A. M. and J. P. BONS. Flow Physics Leading to System Instability in a Centrifugal Pump. *Journal of Turbomachinery*. 1994, **116**(4), 612-620. DOI: https://doi.org/10.1115/1.2929451.

[24] CUI, Baoling, Zuchao ZHU and Ying CHEN. The Flow Simulation and Experimental Study of Low-Specific-Speed High-Speed Complex Centrifugal Impellers. *Chinese Journal of Chemical Engineering*. 2006, **14**(4), 435-441. DOI: https://doi.org/10.1016/S1004-9541(06)60096-7.

[25] LI, Wenguang. Analysis of Flow in Extreme Low Specific Speed Centrifugal Pump Impellers with Multi-split-blade. *International Journal of Turbo and Jet Engines*. 2006, **23**, 73-86.

[26] HONGXUN, C., L. WEIWEI, J. WEN and W. PEIRU. Impellers of low specific speed centrifugal pump based on the draughting technology. *IOP Conference Series: Earth and Environmental Science*. 2010, **12**, 012018. DOI: 10.1088/1755-1315/12/1/012018.

[27] ZHOU, X., X. Y. ZHANG, Z. L. LI and L. CHEN. Hydraulic design and performance analysis of low specific speed centrifugal pump. *IOP Conference Series: Earth and Environmental Science*. IOP Publishing, 2012, **15**(3), 032023. DOI: 10.1088/1755-1315/15/3/032023.

[28] ZHAO, A., P. WU, D. Z. WU and L. Q. The optimization of a low specific speed pipeline pump. *IOP Conference Series: Materials Science and Engineering*. IOP Publishing, 2013, **52**(3), 032002. DOI: 10.1088/1757-899x/52/3/032002.

[29] MIYAMOTO, Hiroyuki, Yukitoshi NAKASHIMA and Hideki OHBA. Effects of Splitter Blades on the Flows and Characteristics in Centrifugal Impellers. *JSME international journal. Ser. 2, Fluids engineering, heat transfer, power, combustion, thermophysical properties*. 1992, **35**(2), 238-246. DOI: 10.1299/jsmeb1988.35.2_238.

[30] GÖLCÜ, Mustafa, Yasar PANCAR and Yakup SEKMEN. Energy saving in a deep well pump with splitter blade. *Energy Conversion and Management*. 2006, **47**(5), 638-651. DOI: https://doi.org/10.1016/j.enconman.2005.05.001. ISSN 0196-8904.

[31] KERGOURLAY, G., Mohand YOUNSI, Farid BAKIR and Robert REY. Influence of Splitter Blades on the Flow Field of a Centrifugal Pump: Test-Analysis Comparison. *International Journal of Rotating Machinery*. 2007, , 085024. DOI: 10.1155/2007/85024.

[32] YUAN, Shouqi, Jinfeng ZHANG, Yue TANG, Jianping YUAN and Yuedeng FU. Research on the Design Method of the Centrifugal Pump With Splitter Blades. *Fluids Engineering Division Summer Meeting*. 2009, **1**, 107-120. DOI: 10.1115/FEDSM2009-78101.

[33] ZHANG, Y. L., S. Q. YUAN, J. F. ZHANG, Y. N. FENG and J. X. LU. Numerical investigation of the effects of splitter blades on the cavitation performance of a centrifugal pump. *IOP Conference Series: Earth and Environmental Science*. 2014, **22**(5), 052003. DOI: 10.1088/1755-1315/22/5/052003.

[34] YE, Liting, Shouqi YUAN, Jinfeng ZHANG and Ye YUAN. Effects of Splitter Blades on the Unsteady Flow of a Centrifugal Pump. *ASME 2012 Fluids Engineering Division Summer Meeting collocated with the ASME 2012 Heat Transfer Summer Conference and the ASME 2012 10th International Conference on Nanochannels*. 2012, , 435-441. DOI: 10.1115/FEDSM2012-72155.

[35] ZHANG, Jingeng, Guidong LI, Jieyun MAO, Shouqi YUAN, Yefei QU and Jing JIA. Effects of the outlet position of splitter blade on the flow characteristics in low-specific-speed centrifugal pump. *Advances in Mechanical Engineering*. 2018, **10**(7). DOI: 10.1177/1687814018789525.

[36] BENIGNI, Helmut, Helmut JABERG and Gerhart PENNINGER. *Dimensioning and simulation of a pump with lowest possible specific speed*. Budapest, Hungary, 2003. ISBN 963-420-779-0.

[37] WIMSHURST, Aidan. *Fundamentals Course*. Available Online: fluidmechanics101.com, 2020.

[38] RUMSEY Christopher. *Turbulence Modeling Resource*. https://turbmodels.larc.nasa.gov

[39] MENTER, F.R. Two-equation eddy-viscosity turbulence models for engineering applications. *AIAA Journal*. 1994, **32**(8), 1598-1605. doi:https://doi.org/10.2514/3.12149

[40] WANG, Y. and W. J. WANG. Applicability of eddy viscosity turbulence models in low specific speed centrifugal pump. *IOP Conference Series: Earth and Environmental Science*. 2012, **15**(6), 062013. DOI: 10.1088/1755-1315/15/6/062013.

[41] JUCKELANDT, Kay, Simona BLEECK and F.-H. WURM. *Analysis of Losses in Centrifugal Pumps with Low Specific Speed with Smooth and Rough walls*. Madrid, 2015. ISSN 2410-4833.

[42] EL-BEHERY, Samy M. and Mofreh H. HAMED. A comparative study of turbulence models performance for separating flow in a planar asymmetric diffuser. *Computers Fluids*. 2011, **44**(1), 248-257. DOI: https://doi.org/10.1016/j.compfluid.2011.01.009.

[43] KOK, J.C. Resolving the dependence on freestream values for the k- turbulence model. *AIAA Journal*. 2000, **38**(7). doi:10.2514/3.14547

[44] ANSYS CFX Solver Guide 2019

[45] SHUR, Michael, Philippe SPALART, Michael STRELETS and Andrey TRAVIN. Turbulence Modeling in Rotating and Curved Channels: Assessing the Spalart-Shur Correction. *AIAA Journal*. 2000, **38**(5), 784-792. Dostupné z: doi:https://doi.org/10.2514/2.1058

[46] OLIMSTAD, Grunde, Morten OSVOLL and Pål Henrik Enger FINSTAD. Very Low Specific Speed Centrifugal Pump - Hydraulic Design and Physical Limitations. *J. Fluids Eng.* 2018, **140**(7), 071403. Dostupné z: doi:https://doi.org/10.1115/1.4039250

[47] POCHYLÝ, František and Jiří STEJSKAL. Rotational Flow in Centrifugal Pump Meridian Using Curvilinear Coordinates. *J. Fluids Eng.* 2016, **138**(8), 081101. Dostupné z: doi:https://doi.org/10.1115/1.4032756

[48] STEJSKAL, Jiří. *Analysis of the Velocity and Pressure Fields of the Liquid Using Curvilinear Coordinate*. Brno, 2017. PhD Thesis. Brno University of Technology.

[49] SMIRNOV, V.I. *A Course of Higher Mathematics*. Oxford, UK: Pergamon, 1964. ISBN 978-0-08-010207-8.

[50] SLOUPENSKÝ, Zdeněk and František POCHYLÝ. *Impeller blade design based on the differential geometry*. Svratka, Czech Republic, 2011.

[51] CHABANNES, Lilian, David ŠTEFAN and Pavel RUDOLF. Volute throat area and wall modelling influence on the numerical performances of a very low specific speed pump. *IOP Conf. Ser.: Earth Environ. Sci.* Lausanne, Switzerland, 2021, **774**(1), 012007. doi:10.1088/1755-1315/774/1/012007

[52] CHABANNES, Lilian and David RUDOLF. Effect of Splitter Blades on Performances of a Very Low Specific Speed Pump. *Energies*. 2021, **14**(13), 3785. doi:https://doi.org/10.3390/en14133785

Nomenclature

BEP	Best Efficiency Point
CAD	Computer Aided Design
CFD	Computational Fluid Dynamics
CLF	Compound Lamellar Flow
CNC	Computer Numerical Control
DNS	Direct Numerical Simulation
DOE	Design Of Experiments
FDM	Fused Deposition Modeling
FVM	Finite Volume Method
GGI	General Grid Interface
LES	Large Eddy Simulation
LR	Low Reynolds number
LSS	Low Specific Speed
PIV	Particle Image Velocimetry
RANS	Reynolds-averaged Navier–Stokes equations
RMS	Root Mean Square
RPM	Revolutions Per Minute
SG	Sidewall Gap
SST	Shear Stress Transport
TKE	Turbulence Kinetic Energy
URANS	Unsteady Reynolds-averaged Navier–Stokes equations
WF	Wall Function

---

a	Splitter blade parameter (leading edge)
A_{vs}	Volute throat area
A_{II}	Impeller outlet area parameter
b_2	Impeller outlet width

b_3	Volute inlet width
b_{z3}	Coriolis acceleration
b_{z1}	Acceleration component
b_{z2}	Acceleration component
b_{z3}	Acceleration component
c_1	Absolute flow velocity at impeller inlet
c_{1m}	Meridional flow velocity at impeller inlet
c_{1u}	Circumferential flow velocity at impeller inlet
c_2	Absolute flow velocity at impeller outlet
c_{2m}	Meridional flow velocity at impeller outlet
$c_{2u\infty}$	Theoretical circumferential flow velocity at impeller outlet
c_{2u}	Circumferential flow velocity at impeller outlet
c_u	Circumferential flow velocity
d_1	Impeller inlet diameter
d_2	Impeller outlet diameter
d_{sp}	Splitter blade leading edge diameter
D	Diameter
D_{vol}	Volute equivalent diameter
$d\dot{m}$	Mass flow rate
f	Friction coefficient
F_{ax}	Axial force
F_{rad}	Radial force
g	Gravitational acceleration
H	Pump Head
H_d	Pump Head at design point
H_{Rec}	Head gain through recirculation at partload
h_0	Busemann head coefficient
$\Delta h_{L,vol}$	Volute friction losses

$\Delta h_{L,vol,secondary}$	Volute secondary losses
k	Turbulence kinetic energy
L_{vol}	Volute developed length
M_k	Torque
$M_{k,static}$	Static torque
N	Rotor Speed
n_s	Specific speed
P	Hydraulic Power
p	Pressure
p_T	Total pressure
P_L	Power loss
P_{opt}	Optimal power
P_{RR}	Disk friction power
Q	Pump delivery flow rate
Q_d	Pump delivery flow rate at design point
Q_{Rec}	Recirculated flow rate
Q_{sp}	Recirculated flow rate
R	Radius
r_1	Impeller inlet radius
r_2	Impeller outlet radius
R_{sl}	Streamline radius
Ro	Rossby number
s_2	Impeller outlet area
S_{vol}	Volute wet surface
t	Time
T_{sp}	Torque splitter blade
u_1	Blade inlet tip velocity
u_2	Blade outlet tip velocity

u_T	Friction velocity
u_ϕ	Absolute uncertainty of parameter ϕ
U^+	Non-dimensional velocity
w_1	Relative flow velocity at impeller inlet
w_2	Relative flow velocity at impeller outlet
w	Relative flow velocity
y	Normal wall distance
y^+	Non-dimensional distance from the wall
Z	Blade number

α_{sp}	Splitter blade parameter (outlet blade angle)
β	Blade angle
β_1	Flow angle at impeller inlet
β_{1B}	Impeller inlet blade angle
β_2	Flow angle at impeller outlet
β_{2B}	Impeller outlet blade angle
γ	Slip factor
ϵ	Equivalent sand roughness
ϵ	Rate of dissipation of turbulent kinetic energy
η	Hydraulic efficiency
η_{vol}	Volumetric efficiency
θ	Splitter blade parameter (circumferential position)
ν	Kinematic viscosity
μ	Dynamic viscosity
τ	Shaft torque
τ_{ij}	Reynolds stress tensor
τ_w	Wall shear stress
Ψ_{imp}	Impeller head coefficient

Ψ_{vol}	Volute head coefficient
ρ	Density
ω	Angular velocity
ω	Specific rate of dissipation of the turbulence kinetic energy